NASA/CR—2010-216812

Rotorcraft Transmission Noise Path Model, Including Distributed Fluid Film Bearing Impedance Modeling

Stephen A. Hambric, Amanda D. Hanford, Micah R. Shepherd,
Robert L. Campbell, and Edward C. Smith
Pennsylvania State University, State College, Pennsylvania

September 2010

NASA STI Program . . . in Profile

Since its founding, NASA has been dedicated to the advancement of aeronautics and space science. The NASA Scientific and Technical Information (STI) program plays a key part in helping NASA maintain this important role.

The NASA STI Program operates under the auspices of the Agency Chief Information Officer. It collects, organizes, provides for archiving, and disseminates NASA's STI. The NASA STI program provides access to the NASA Aeronautics and Space Database and its public interface, the NASA Technical Reports Server, thus providing one of the largest collections of aeronautical and space science STI in the world. Results are published in both non-NASA channels and by NASA in the NASA STI Report Series, which includes the following report types:

- TECHNICAL PUBLICATION. Reports of completed research or a major significant phase of research that present the results of NASA programs and include extensive data or theoretical analysis. Includes compilations of significant scientific and technical data and information deemed to be of continuing reference value. NASA counterpart of peer-reviewed formal professional papers but has less stringent limitations on manuscript length and extent of graphic presentations.

- TECHNICAL MEMORANDUM. Scientific and technical findings that are preliminary or of specialized interest, e.g., quick release reports, working papers, and bibliographies that contain minimal annotation. Does not contain extensive analysis.

- CONTRACTOR REPORT. Scientific and technical findings by NASA-sponsored contractors and grantees.

- CONFERENCE PUBLICATION. Collected papers from scientific and technical conferences, symposia, seminars, or other meetings sponsored or cosponsored by NASA.

- SPECIAL PUBLICATION. Scientific, technical, or historical information from NASA programs, projects, and missions, often concerned with subjects having substantial public interest.

- TECHNICAL TRANSLATION. English-language translations of foreign scientific and technical material pertinent to NASA's mission.

Specialized services also include creating custom thesauri, building customized databases, organizing and publishing research results.

For more information about the NASA STI program, see the following:

- Access the NASA STI program home page at *http://www.sti.nasa.gov*

- E-mail your question via the Internet to *help@sti.nasa.gov*

- Fax your question to the NASA STI Help Desk at 443–757–5803

- Telephone the NASA STI Help Desk at 443–757–5802

- Write to:
  NASA Center for AeroSpace Information (CASI)
  7115 Standard Drive
  Hanover, MD 21076–1320

NASA/CR—2010-216812

Rotorcraft Transmission Noise Path Model, Including Distributed Fluid Film Bearing Impedance Modeling

Stephen A. Hambric, Amanda D. Hanford, Micah R. Shepherd,
Robert L. Campbell, and Edward C. Smith
Pennsylvania State University, State College, Pennsylvania

Prepared under Contract NNC08CB07C

National Aeronautics and
Space Administration

Glenn Research Center
Cleveland, Ohio 44135

September 2010

Level of Review: This material has been technically reviewed by NASA expert reviewer(s).

Available from

NASA Center for Aerospace Information
7115 Standard Drive
Hanover, MD 21076–1320

National Technical Information Service
5301 Shawnee Road
Alexandria, VA 22312

Available electronically at http://gltrs.grc.nasa.gov

Rotorcraft Transmission Noise Path Model, Including Distributed Fluid Film Bearing Impedance Modeling

Stephen A. Hambric, Amanda D. Hanford, Micah R. Shepherd,
Robert L. Campbell, and Edward C. Smith
Pennsylvania State University
State College, Pennsylvania 16804

Abstract

A computational approach for simulating the effects of rolling element and journal bearings on the vibration and sound transmission through gearboxes has been demonstrated. The approach, using ARL/Penn State's CHAMP methodology, uses Component Mode Synthesis of housing and shafting modes computed using Finite Element (FE) models to allow for rapid adjustment of bearing impedances in gearbox models. The approach has been demonstrated on NASA GRC's test gearbox with three different bearing configurations: in the first condition, traditional rolling element (ball and roller) bearings were installed, and in the second and third conditions, the traditional bearings were replaced with journal and wave bearings (wave bearings are journal bearings with a multi-lobed wave pattern on the bearing surface). A methodology for computing the stiffnesses and damping in journal and wave bearings has been presented, and demonstrated for the journal and wave bearings used in the NASA GRC test gearbox. The FE model of the gearbox, along with the rolling element bearing coupling impedances, was analyzed to compute dynamic transfer functions between forces applied to the meshing gears and accelerations on the gearbox housing, including several locations near the bearings. A Boundary Element (BE) acoustic model was used to compute the sound radiated by the gearbox. Measurements of the Gear Mesh Frequency (GMF) tones were made by NASA GRC at several operational speeds for the rolling element and journal bearing gearbox configurations. Both the measurements and the CHAMP numerical model indicate that the journal bearings reduce vibration and noise for the second harmonic of the gear meshing tones, but show no clear benefit to using journal bearings to reduce the amplitudes of the fundamental gear meshing tones. Also, the numerical model shows that the gearbox vibrations and radiated sound are similar for journal and wave bearing configurations.

Contents

1 Introduction

Commercial and military rotorcraft are powered by drive systems comprised of complex transmissions, which contain sets of gears and shafts supported by bearings. As the gears rotate at high rates of speed under high torques, they generate vibrations at multiples of Gear Meshing Frequency (GMF). The vibrations pass through the gear shafts, through the bearings, and into the transmission housing, which in turn radiates sound at the GMF frequencies. The housing also transmits vibrations to the cockpit through its support mounts, and the cockpit walls radiate sound into the interior. The resulting noise is usually referred to as 'gear whine', and often exceeds 100 dBA in rotorcraft interiors [1], with strong tones in the critical speech communication frequency range of 1-4 kHz.

To date, rotorcraft transmissions have used rolling element (ball or roller) bearings. Journal bearings, which transmit loads through thin films of lubricant, such as transmission oil, have significantly higher vibration damping, and might attenuate the GMF tones. Journal bearings have not been used in rotorcraft for two key reasons: the fundamental rotational instability mode which leads to shaft 'whirl', and a concern in the rotorcraft community that the bearings would not be able to withstand a loss of lubricant feed, leading to catastrophic failures.

The first and second concerns have been addressed by the so-called 'Wave Bearing', developed by Dimofte [2-3], which is a pressurized journal bearing with a circumferential wave pattern applied to the bearing surface. The wave pattern, with an amplitude of about half of the mean fluid film thickness, prevents the whirl instability from occurring anywhere in the usual operating ranges of a transmission. Therefore, the wave bearings might be usable in rotorcraft transmissions, and could mitigate vibration transmission and radiated sound.

Numerical models of transmissions [4-11] may be used to assess the potential benefits of replacing rolling element bearings (REBs) with wave (and conventional journal) bearings (WBs). Finite Element (FE) models of shafts and housings may be coupled via the impedances of the bearings that connect them. Component Mode Synthesis (CMS) techniques [12-17] may be used to adjust the bearing impedances and efficiently assess the differences between the vibration transmissibility of REB and WB systems. Dynamic loads, which model the gear tooth transmission errors, placed at the locations of meshing gear teeth may be used to drive the assembled model, and vibrations on the housing may be monitored.

The sound radiated by the transmission housings can be modeled using Boundary Element (BE) techniques, where a boundary element mesh surrounds the FE model of the gearbox housing. Oswald, Seybert, and Wu [18] confirmed that BE models can accurately compute gearbox radiated sound, provided the gearbox housing surface vibrations are known.

In this report, we summarize the development of a steady-state, time-harmonic modeling procedure for simulating the transmission of vibration through the shafting and bearings of the NASA Glenn Research Center (GRC) test gearbox, including the cross-coupling effects of the shafts and bearings and the damping within fluid film bearings. The test gearbox contains a single-stage spur gear system, providing a simple means of assessing the performance of journal and wave bearings. Measured vibrations and

sound pressures acquired at a limited number of rotational speeds and operating torques are available to compare to the numerical simulations. The measurements and simulations will reveal the potential benefits (or degradations) of replacing traditional rolling element bearings with journal bearings in gearboxes. In particular, the following items are described:

- FE and BE modeling of the NASA GRC gearbox,
- analytic modeling of REB, journal, and wave bearing impedances;
- CMS approach for simulating the coupling impedances of REBs and WBs;
- verification of the FE modeling by comparison to structural-acoustic measurements made on the NASA GRC gearbox, and
- comparisons of simulations and measurements of the differences between vibration transmissibility and radiated sound between gearboxes with REBs and WBs (with and without waveforms).

2 Overview of NASA GRC Gearbox and Gearbox Noise Mechanisms

2.1 NASA GRC Gearbox

Photographs of the NASA GRC gearbox are shown in Figure 1, and a schematic of the gearbox with key dimensions is shown in Figure 2 and described further in Table 1. Two identical spur gears (shown in Figure 3 with properties listed in Table 2) are mounted to the shafts, which are supported at both ends by bearings within the housing. Ball bearings support the shafts at their loaded ends, and roller bearings are used at the free ends. The input and output shafts are connected to larger external shafts via flexible couplings. The external shafts are not modeled in this project, with the internal shaft models terminated with the estimated impedances of the flexible couplings. The gearbox is a simple rectangular steel box, with a flat plate bolted to its top on a stiff mounting flange. An O-ring is sandwiched between the top plate and flange within a groove machined into the top plate. The top mounting flange and all of the walls are 0.25” thick. The gearbox is mounted to another box-like support structure, which is attached to the base of the test rig. More details on the test rig may be found in [1, 19].

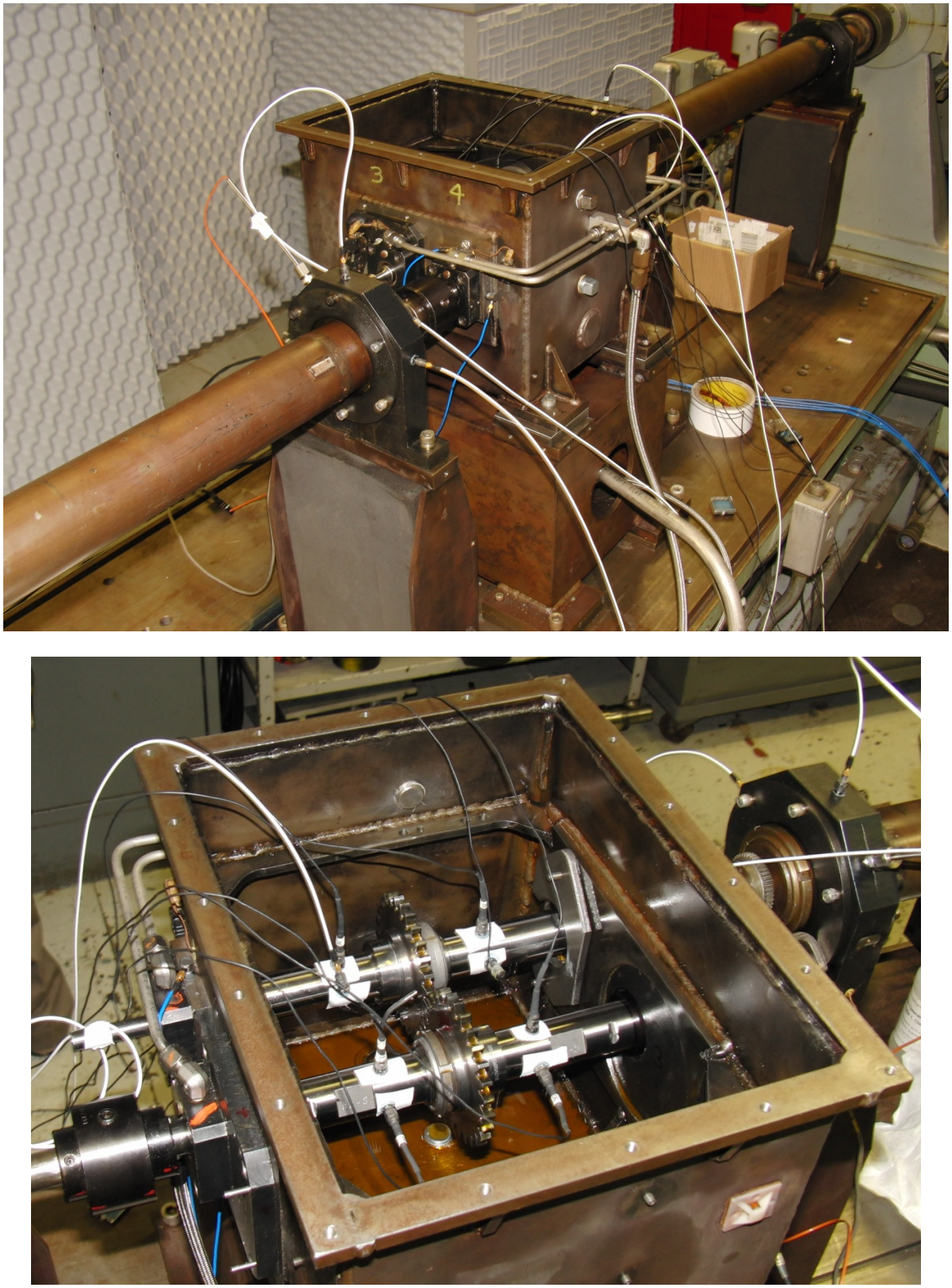

Figure 1. NASA GRC test gearbox with lid removed and instrumentation attached.

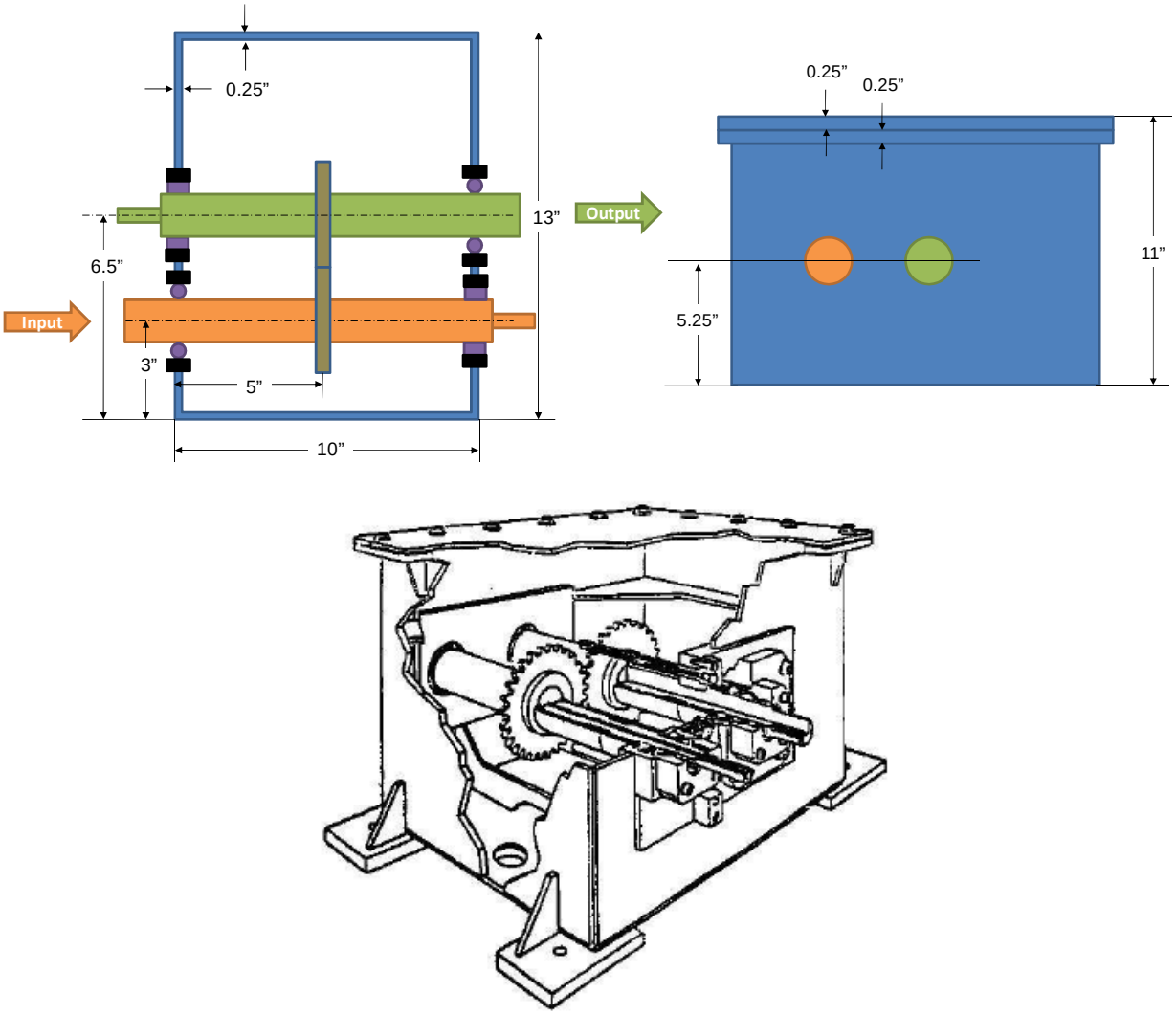

Figure 2. Schematic of NASA GRC test gearbox. Left - top view with lid cut away; Right - side view.

Height (in)	11
Width (in)	10
Length (in)	13
Wall thickness (in)	0.25
Lid thickness (in)	0.25
Material	Steel

Table 1. NASA GRC test gearbox dimensions and materials.

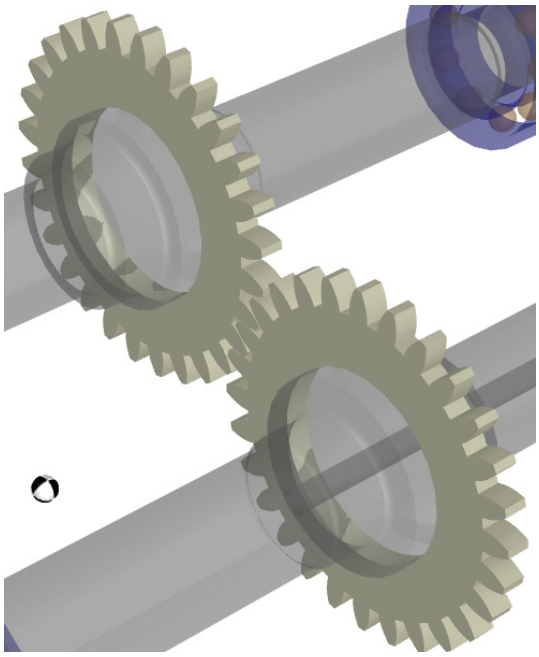

Figure 3. Twin spur gears in NASA GRC gearbox.

Parameter	Value
Number of teeth	28
Outer diameter (in)	3.75”, with 0.006” edge break/tip chamfer
Root diameter (in)	3.139”
Facewidth (in)	0.25”
Diametral pitch (1/in)	8
Pressure angle	20 degrees
Standard center distance between gears (in)	3.5”
Tooth thickness (in)	0.191, with 0.007” backlash
Cutter edge radius (in)	0.05”
Linear tip relief on both flanks (in)	0.0007” starting at 24 degrees

Table 2. NASA GRC gearbox spur gear parameters.

2.2 Gear Transmission Error (GTE)

Gear whine is not limited to rotorcraft transmissions, and also occurs in automobiles [6, 20], construction equipment [4], industrial machinery, and many other applications. As mating gears rotate, loads are transmitted through the gear teeth and into the shafting. As the teeth pass over each other, geometric imperfections, material deformations, and geometric misalignments lead to deviations in the load transmission, causing Gear Transmission Error (GTE) [21, 22]. GTE manifests itself as unsteady displacements that occur at a series of harmonics of the Gear Meshing Frequency (GMF). The

fluctuating displacements cause unsteady forces which are transmitted into the shafting, through the bearings, and into the transmission housing.

Misalignment between the shafts and gearbox, or between the shafts themselves, along with shaft imbalance and/or electrical oscillations, lead to deformations and dynamic loads which occur at multiples of shaft rotation speed. The deformations also modulate the spacing between the meshing gears, and therefore modulate the amplitudes of the GMF tones, causing side bands to appear at frequencies corresponding to GMF +- shaft rate multiples. Geometrical deviations between gear tooth spacing, and gear tooth geometry, also lead to amplitude modulation and side band tones [23, 24]. Figure 4 shows a typical gearbox noise spectrum with shaft harmonics, GMF harmonics, and side band tones.

GTE may be simulated by computing the time histories of the gear tooth locations, and deformations under load. Classical analyses consider only the gear microgeometry (the shape of the teeth), the overall tooth deflection, and the localized Hertzian deformation of the tooth surfaces under load. Since the tooth deflection and deformation depend on the system load (or torque), the GTE also depends on the loading. GTE, however, also depends on any misalignments between the gears, which may be caused by deformation of the shafting and bearings under loaded conditions, and deformations of the gearbox. As pointed out in [20], modern gearboxes and shafting are generally constructed of lightweight flexible materials, leading to GTE contributions from misalignments which are comparable to those caused by gear tooth microgeometry differences. GTE amplitudes, while strongly dependent on operating torque, do not depend on operational speed. The GTE frequencies, however, are directly proportional to operating speed.

As the gear teeth slide into and away from each other, frictional forces are also generated from the so-called ‘stick-slip’ interaction. These frictional loads are not commonly considered in gearbox noise analyses, but may be significant, particularly under high loading and at certain GMF harmonics [10, 11]. The frictional forces drive the gearbox system in the Off-Line of Action (OLOA), or in the direction perpendicular to the common gear tooth loads, which occur in the Line of Action (LOA).

Various GTE modeling procedures have been proposed over the years, including those incorporated into the commercial software packages Romax [25] and Calyx [26]. Ohio State University has also documented its LDP software [27], which is referenced by several gearbox noise studies. In this report, however, we compare only the relative vibration and noise differences between gearboxes equipped with REB and journal and wave bearings, and do not attempt to compute GTE. We therefore compute vibration and noise with respect to unit displacement transmission error, following the guidance in [4].

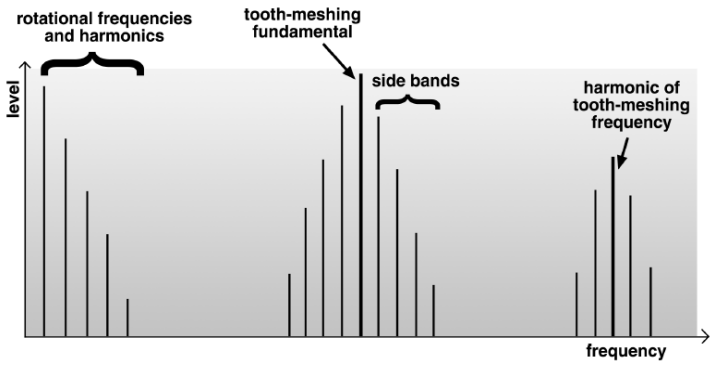

Figure 4. Typical gearbox vibration spectrum.

2.3 Shaft and Bearing Response and Transmissibility

The static gear loads push one of the shafts downward and the other upward, pre-loading the support bearings. The dynamic gear loads drive the shafting, causing it to vibrate in beam-like motion at low frequencies. The shafts may be viewed as beams resting on supports near their ends, and connected together near their center by the stiffness of the meshing gear teeth in the LOA direction. The gear meshing stiffness may be computed using simple cantilever beam theory along with the tooth dimensions and materials. Commercial software tools like Romax also consider the tooth contact ratios in their assessments of meshing stiffness. However, it appears that most of the gear noise community ignores the frictional stiffnesses in the OLOA direction between meshing teeth.

The shafts typically vibrate at their fundamental beam-like resonance frequencies, as shown by Zhou [28]. The shafts amplify the gear loads for modes with high amplitudes (antinodes) near the gears, and attenuate loads for modes with very small amplitudes (nodes) near the gears. The resonance frequencies and mode shapes depend not only on the shaft dimensions and materials, but on the bearing locations and impedances, and housing impedances. Early studies of gearbox noise often ignored these effects, and used lumped parameter models of the shafts and gears [29]. When bearing impedances were considered, rotational terms were ignored, filtering any transmission of unsteady moments from the shafts to the housing. Omitting moment transmissibility from gearbox noise modeling can cause significant errors, particularly when bearings are offset from the neutral axes of the gearbox walls. Since Zhou [28] showed in a series of measurements that offset bearings lead to higher noise, it is clearly important to include moment terms in any gearbox noise modeling.

Unfortunately, early models of rolling element bearing stiffnesses consider only translational terms [30]. Lim and Singh [31], however, derived approaches for modeling the full stiffness matrix, including translational and rotational terms, as well as cross-coupling terms, for ball and roller bearings. This approach was later refined by Liew and Lim [32]. The approach considers the non-linear deformation of the balls or rollers under various loading conditions. The deformation is governed by Hertzian contact theory, which depends on the rolling element geometry and material properties. As static load increases, more of the ball surface deforms locally, and contacts the neighboring bearing structure. Further complicating matters, the number of balls or rollers in contact with the bearing varies with

angular position. Since nearly all gearbox noise modeling is conducted in the frequency domain, it is common to simply average the overall bearing impedances over a range of angular positions. Also, the bearing stiffnesses must be computed for each load condition, or torque, due to the non-linearity of the load-deflection behavior. As load increases, bearing stiffness increases.

2.4 Gearbox Vibration and Noise

The gear meshing tones, after being either amplified or attenuated by the shafting vibration and transmission through the various bearings, enter the gearbox housing in the form of dynamic forces and moments at each bearing location. The walls of the housing then vibrate and radiate sound. The wall vibration depends on the gearbox geometry and material properties, which determine the structural mode shapes of the housing. The wall modes also depend strongly on the shafting, which can stiffen the overall structure considerably, and lead to strongly coupled shafting-housing modes of vibration. For thick walls with high elastic moduli and mass densities, the vibrations can be quite small. For housings built with lightweight, flexible materials, however, the modal vibrations can be quite large. The higher vibrations lead to higher sound radiation, as shown by Igarashi and Nishizaki [33], who measured the sound radiated by Aluminum and Cast Iron gearboxes. The iron gearboxes were constructed with varying wall thicknesses. Not surprisingly, the more massive and stiff the gearbox, the lower the noise.

For non-metallic materials, however, the radiation characteristics of the walls differ from those of metal. The sound power radiation efficiency – the ratio of sound power to wall vibration, surface area, and acoustic impedance – depends on a wall panel's critical frequency, which is the frequency at which the speeds of structural bending waves match those in the surrounding air. Above the critical frequency, the radiation efficiency is one, and the sound power radiated by a vibrating gearbox is easily calculated by averaging the square of the normal surface velocities over the surface area and combining that average with the surface area and acoustic impedance. Below, the critical frequency, however, the radiation efficiency decreases with decreasing frequency. For simple panels, the frequency dependence is usually that of the most efficiently radiating modes, and is often assumed to vary with the square of frequency, or with $(f/f_c)^2$, where f_c is the critical frequency. Igarashi and Asano [34], however, measured the radiation efficiencies of gearboxes, and showed radiation efficiency frequency dependencies which were less strong than the square of frequency, varying between $(f/f_c)^{1.2}$ – $(f/f_c)^{1.9}$.

2.5 Vibration and Noise Measurements

As Figure 4 shows, gearbox vibration and noise is highly tonal in nature. The underlying structural-acoustic transfer functions between the gear tooth forcing functions and the eventual noise measurement locations are therefore only visible at the tonal frequencies. To visualize the continuous transfer functions, a sweep through a range of rotational speeds is required, sometimes called a 'run-up'. The amplitude and frequency of each tone is traced through increasing rotational speed to generate the transfer functions. In many experiments, the rotational speed is increased slowly over time with data acquired continuously. Order tracking algorithms, available in some commercial vibro-acoustic data acquisition systems, are used to capture the peak amplitudes at specific GMFs [35].

If continuous speed sweeps are not feasible, data is acquired at several speeds in individual tests, and a coarse accounting of the structural-acoustic transfer functions may be pieced together. This is the

procedure used at NASA GRC for their gearbox tests. Care must be taken when extracting the tone peaks, however, as simple spectral analysis may not yield accurate results, particularly when the tonal amplitudes vary slowly over time, which often occurs in industrial and rotorcraft gearboxes. Appendix A demonstrates how the tone amplitudes are measured, along with examples of the amplitude variabilities.

While the tonal amplitudes can vary over time during a single measurement, they are also known to vary from test to test. Oswald [19], and Sellgren and Akerblom [4] demonstrated that disassembling and reassembling a gearbox leads to tonal amplitude variability of nominally +-3 dB. Sellgren and Akerblom suspected that differences in bearing axial preloading is responsible for the variability they observed in their measurements. However, the bearings in the NASA GRC test gearbox used in Oswald's measurements were not axially preloaded, so the cause(s) of the variability are not yet understood, but are likely to be associated with differences in gear alignment, leading to differences in the GTE. Based on these experiences, any differences in gearbox noise caused by changing the bearings must exceed 3 dB to be considered meaningful.

2.6 Ramifications of Replacing REBs with Journal or Wave Bearings

Replacing the ball and roller bearings currently in the NASA GRC gearbox with journal or wave bearings will change:

- the bearing stiffnesses, and increase significantly the bearing damping, affecting the transmission of vibration through the bearings and into the housing;
- the coupled housing/shafting mode shapes and resonance frequencies, altering the structural-acoustic transfer functions between the gear forcing functions and the vibration and radiated sound monitoring points; and
- the shafting boundary conditions, which will change the shaft end deflections under torque loading, and subsequently the misalignment between the gear teeth and resulting GTE.

However, since the gears are situated at the center of the gearbox, and all the journal/wave bearings will be identical, it is unlikely that changes in the shaft boundary conditions will lead to significant changes in GTE. Therefore, the primary differences in noise transmissibility will be due to the altered transmissibility through the bearings, and to the changes in the structural-acoustic behavior of the gearbox.

3 Modeling and Analysis

Computer Aided Drafting (CAD) files of the gearbox were provided by NASA GRC for both rolling element (REB) and wave bearing (WB) configurations. CAD images of the gearbox with REBs and with the housing cover removed are shown in Figure 5. FE models were constructed of the gearbox housing, including the lower support frame, and the shafting and gear blanks. The bearing impedances are modeled analytically, and applied as interface conditions between the shafting and gearbox, cross-coupling the shafting and gearbox modes of vibration. A dynamic force is applied to the gears at the

tooth meshing location in the line of action (LOA) to simulate GMF loads, along with the gear meshing stiffness, effectively applying an enforced displacement to the gears. Vibrations throughout the gearbox are computed, and input to a BE model of the air surrounding the gearbox to compute radiated sound.

Two sets of simulations are compared to measurements made at NASA GRC: one with the lid removed, and the other with the lid attached. The simulations with the lid removed are compared to static vibration measurements, where the gear teeth are struck with instrumented force impact hammers and wall vibrations are measured with accelerometers. The simulations with the lid attached are compared to a limited set of operating gearbox measurements over a coarse distribution of operating speeds. The vibrations and radiated sound are computed for a range of operating speeds (between 2000 and 6000 rpm) and GMFs (1-2x GMF), and a single torque (700 in-lb, which corresponds to the theoretical minimum of GTE for this gearset). The simulated levels are normalized to a unit GTE so that actual operating levels may be computed given a known GTE amplitude. The differences between the simulated levels with traditional REB and the new journal and wave bearings are compared to the differences observed in the NASA GRC measurements.

3.1 Finite Element Modeling of Gearbox Housing

The housing, base structure, and shafts were modeled with quadratic tetrahedral finite elements, as shown in Figure 6. The model includes about 190,000 nodes and 93,000 solid elements. The feet of the base structure were attached rigidly to ground. The top plate is rigidly connected to the housing at bolt locations, and attached vertically to the housing along the o-ring (in-plane motion is not constrained along the o-ring). The drive and output shafts are modeled up to the point where they couple with the external shafts.

The gear blanks are modeled with finite elements, but the teeth are not. Instead of modeling the teeth, the two gear blanks are coupled by the averaged stiffness of the meshing gear teeth. Gear tooth stiffnesses may be derived from simple beam theory and tooth geometry and material properties, or from the commercial software Romax. Based on Romax calculations, a gear mesh stiffness of 108 kN/mm (averaged over a range of gear tooth positions) is applied in the LOA direction (20 degrees from vertical) between the FE gear blank models. The stiffness is divided between two springs – one on each edge of the gear blanks. The gear mesh stiffness couples the shaft modes of vibration, generating coupled two-beam mode sets in both the vertical and horizontal directions. No stiffnesses in the off-line-of-action (OLOA) or axial directions are applied to the teeth, although they surely exist, due to frictional resistance between the loaded tooth surfaces.

Since the shafts and gearbox housing are modeled with solid elements, some constraint equations must be used to model the connectivity via the bearing impedances. Figure 7 shows a schematic of the coupling procedure. Since the shaft and housing bearing holes remain nearly circular at the analysis frequencies of interest, they may be coupled by generating nodes on the shaft centerline, and constraining the motion of those nodes to the averaged motion of the shaft and bearing. In the example, node 5 (at the shaft center) and the four shaft nodes (separated by 90 degree increments) are constrained to move together. Similarly, node 10 (also at the shaft center) and four housing nodes are also constrained to move together. The rotations of the shaft and housing are also constrained to

match those of the center nodes 5 and 10 using moment arms between the shaft center and the shaft and housing diameters. In the example, moment arms are shown in the x direction. Next, the translational and rotational stiffnesses and damping values (along with coupling terms between them) are simply applied between the central nodes 5 and 10. For higher frequency analyses, where the housing may deform in ovaling, or other patterns, the distributed impedances of the bearings must be applied between adjacent nodes around the circumference.

The drive and output shaft ends are connected to flexible couplers: R+W EKH elastomer jaw couplings, Series 150. The couplers were initially fitted with type B elastomer inserts, which have a torsional stiffness of 29,300 N-m/rad. Later, NASA GRC switched to softer elastomers (type C), with a torsional stiffness of 3,590 N-m/rad. The manufacturer does not provide the coupling stiffnesses in the transverse and axial directions, so they were estimated based on the coupler geometry, shown in Figure 8 (moment stiffnesses were not estimated).

To compute the transverse stiffnesses, the elastic moduli of the inserts were estimated. Based on the number of inserts (8) and their approximate geometry (the moment arm for each segment is about 17 mm to the segment centroid), the compressional stiffness of one segment is the total torsional stiffness divided by the square of the moment arm, or K_{torque}/2.3E-3 N/m. If we assume that half (four) of the segments are in compression under transverse loading, the translation stiffness is approximately 4*K_{torque}/2.3E-3 N/m. The axial stiffness depends on the shear moduli of the inserts, which may be assumed to be 1/3 of the compressional moduli (for nearly incompressible rubbers). Since all segments will resist axial motion in shear, the axial stiffness is approximately (8/3)*Ktorque/2.3E-3. The final stiffnesses are listed in Table 3. Although the stiffnesses of the flexible couplers are likely complex (including material damping), the vendor has not provided an estimated loss factor. The damping is therefore ignored.

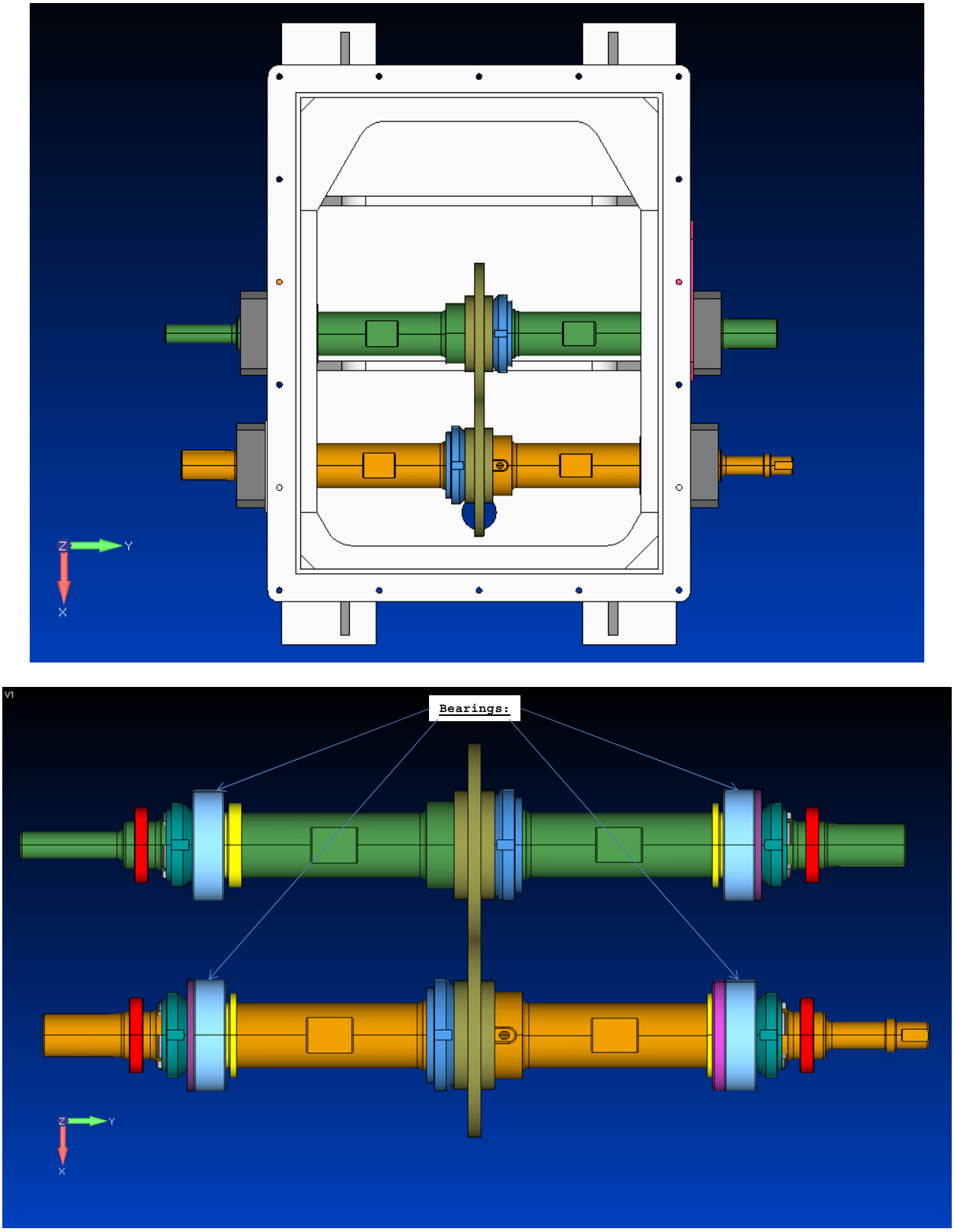

Figure 5. CAD database images of gearbox and shafting (top) and shafting with rolling element bearings (bottom).

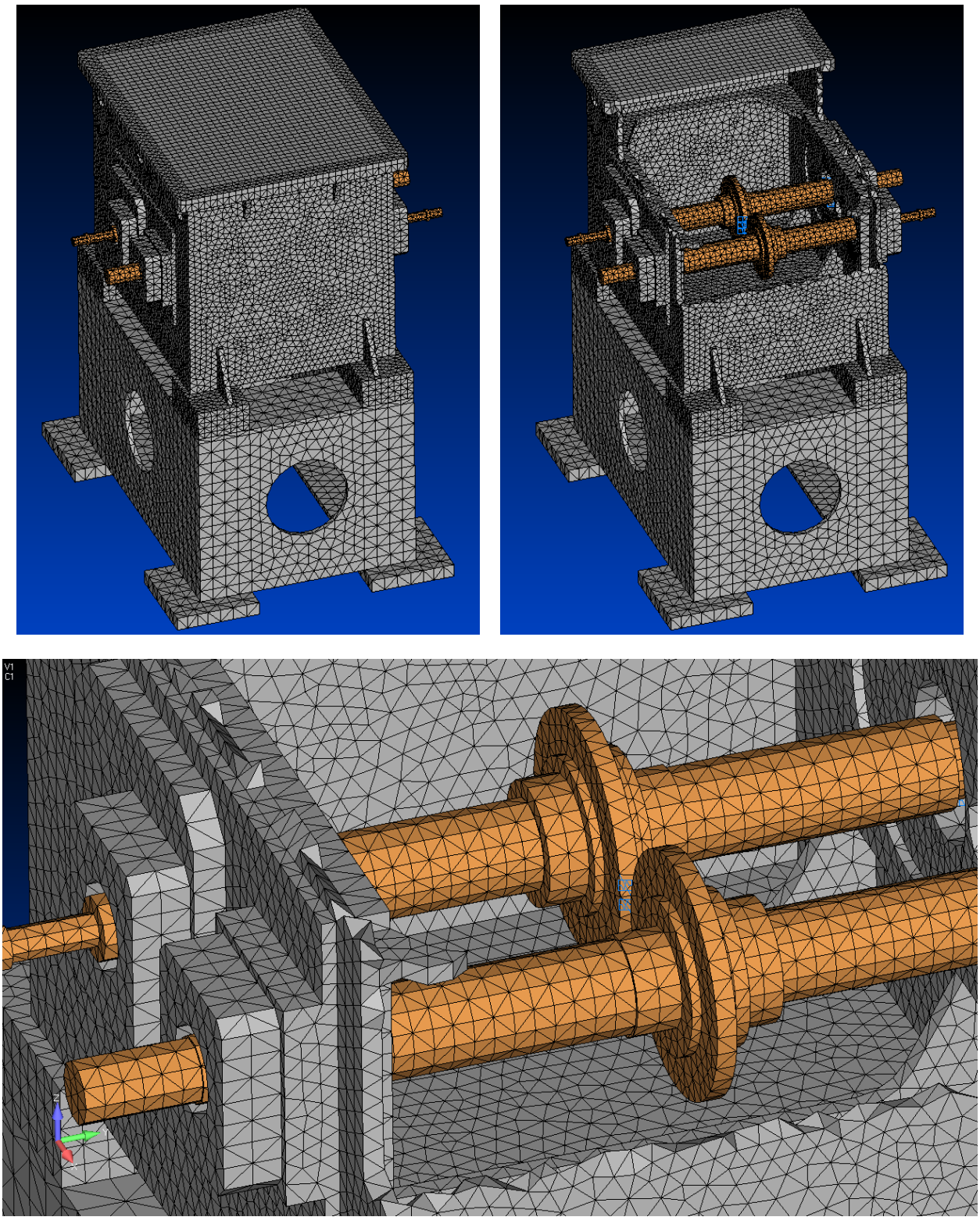

Figure 6. Finite element model of NASA GRC gearbox. Right - part of top cover and front and side walls removed to reveal inner shafting and gear blanks. Bottom – zoom of shafting and gear blanks.

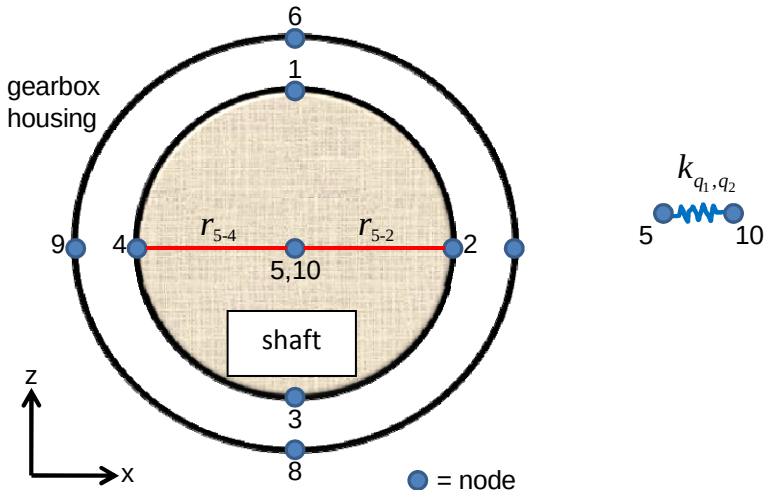

Figure 7. Approach for coupling shafting and housing models.

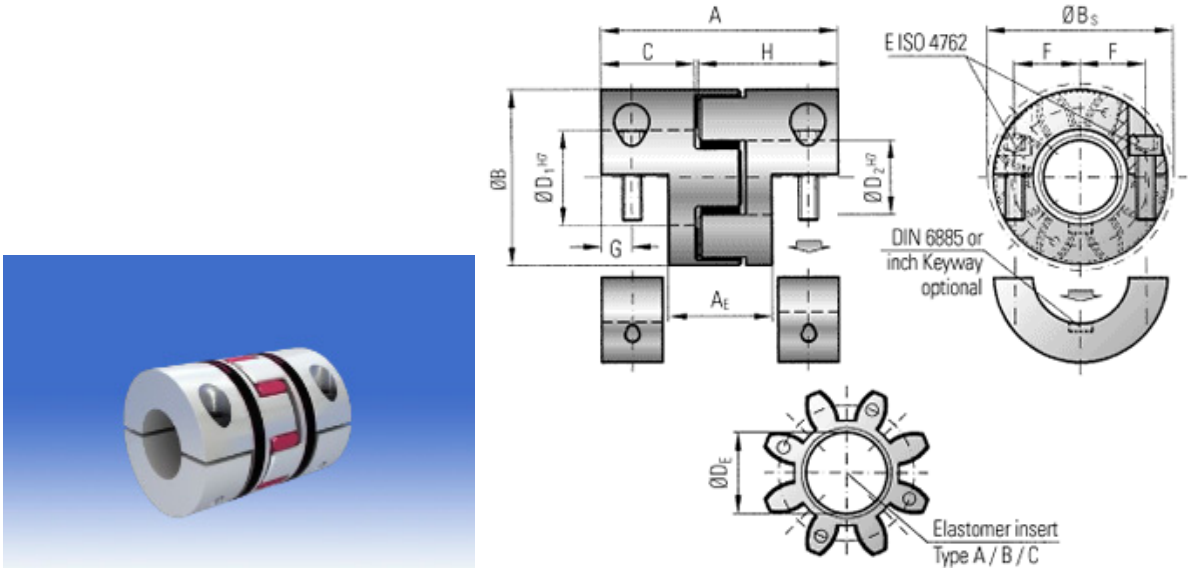

Figure 8. Flexible couplings applied to drive and output shafts.

Insert type	Torsional stiffness (N-m/rad)	Transverse stiffness (N/m)	Axial stiffness (N/m)
B	29,300	51E6	34E6
C	3,590	1.5E6	6.2E6

Table 3. Elastomeric coupling stiffnesses.

3.2 Component Mode Synthesis

The impedances of the REBs or WBs may be applied directly within the FE model between the shafts and housing, and separate FE models of gearboxes with REBs and WBs may be analyzed and compared. However, this approach is computationally inefficient, and does not allow rapid assessment of the effects of changing bearings. Also, since the impedances of all bearings vary with load condition (torque), and the impedances of journal (and wave) bearings vary with rotational speed and lubricant temperature, a prohibitive number of FE analyses would be required to generate gearbox noise spectra. Clearly, a more computationally efficient modeling approach is required.

Component mode synthesis (CMS) [12-15] allows for a simple, efficient means of coupling the shafts and housing via their component modes. In CMS, the amplitudes of the component modes required to satisfy continuity of displacements at the connections between the shafts and housing are solved for. Typically, component modes with free boundary conditions are used in CMS, although modes with other boundary conditions may also be applied. However, the CMS approach can have difficulty converging to accurate solutions due to modal truncation errors when an insufficient number of modes is used in the analysis [16]. For many problems the number of modes required to obtain accurate solutions can be prohibitive. Fortunately, a simple approach which uses residual vectors to approximate the static effects of high frequency modes on the CMS solution is available in the NASTRAN commercial finite element software [36]. The residual vectors are computed by applying static loads at all interface locations, and at all points where forces will be applied. The resulting displacement fields are modified by subtracting the contributions from the modes which are included in the CMS solution, leaving behind the static terms from all high-frequency modes which are excluded. These residual vector 'modes' are then added to the group of actual modes, and included in the CMS analysis, dramatically improving solution convergence and accuracy.

ARL/Penn State's CHAMP approach (Computational Hydroacoustic Modeling Programs) [37, 38], shown in Figure 9, is based on CMS. Component modes of the gearbox (without shafts) and the shafting (without the gearbox) may be computed by a commercial FE code, such as NASTRAN, and stored. Next, CHAMP computes the forced response of the coupled system based on the component modes, and any combination of impedances which couple the component modes together.

To confirm that the CHAMP approach will work on a gearbox, a simple model with properties similar to those of the NASA GRC gearbox was constructed, as shown in Figure 10. The box dimensions and wall thicknesses are consistent with those of the NASA GRC gearbox, and a single shaft, modeled with beam elements, is inserted in the center of the box, and coupled to the box via a roller and ball bearing. The shaft is driven at its center, and the response of the shaft and housing top plate are computed both with CMS, and directly within the FE software (a direct, exact solution which does not rely on a modal series summation). Sample modes of the uncoupled box and shafting are shown in Figure 11. Note that the shafting is actually circular, but represented with a square cross section in the FE viewing software.

Figure 12 compares computed top plate vibrations in response to a shaft drive. The 'actual stiffness' curve is the exact, direct solution, and the 'zero stiffness' curves are based on CMS solutions with and without residual vectors. When residual vectors are excluded from the solution, the CMS and exact

results match only at a few selected resonance frequencies, and differ significantly at all other frequencies. Including the residual vectors leads to dramatic improvement in the CMS results. However, the CMS and exact results still do not match perfectly. To improve convergence, we therefore modify the CMS procedure to use component modes which are based on including nominal bearing stiffnesses in the FE model.

The nominal bearing stiffnesses, which are set based on the computed rolling element and journal bearing stiffnesses over the ranges of operational speeds and torque conditions considered, lead to a set of component modes which are very similar to those which occur under the various operating conditions. To correct the bearing stiffnesses to the actual values, the differences between the actual and nominal bearing stiffnesses are added or subtracted to the nominal values during the CMS process. This procedure, while efficiently allowing for rapid assessment of bearing changes, also allows for non-symmetric bearing stiffnesses to be accounted for easily, by using symmetric nominal stiffnesses to compute the component modes, and correcting to the actual non-symmetric bearing stiffnesses during the CMS analysis. Figure 13 compares the exact top plate vibration solution with a solution using nominal bearing stiffnesses (chosen here to be the average of the ball and roller bearing stiffnesses), and a solution using CMS and adjustments to the bearing stiffnesses. The exact and CMS solution based on modes computed using nominal bearing stiffnesses are nearly identical.

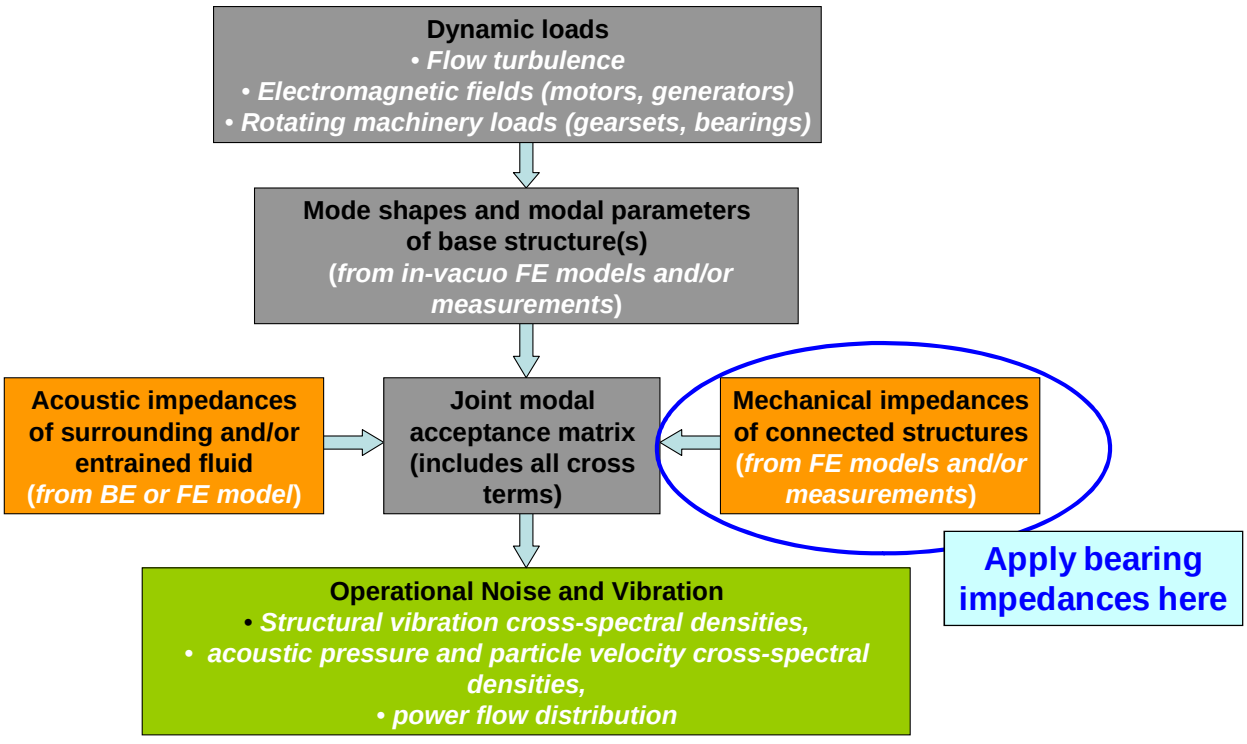

Figure 9. CHAMP noise and vibration simulation capability.

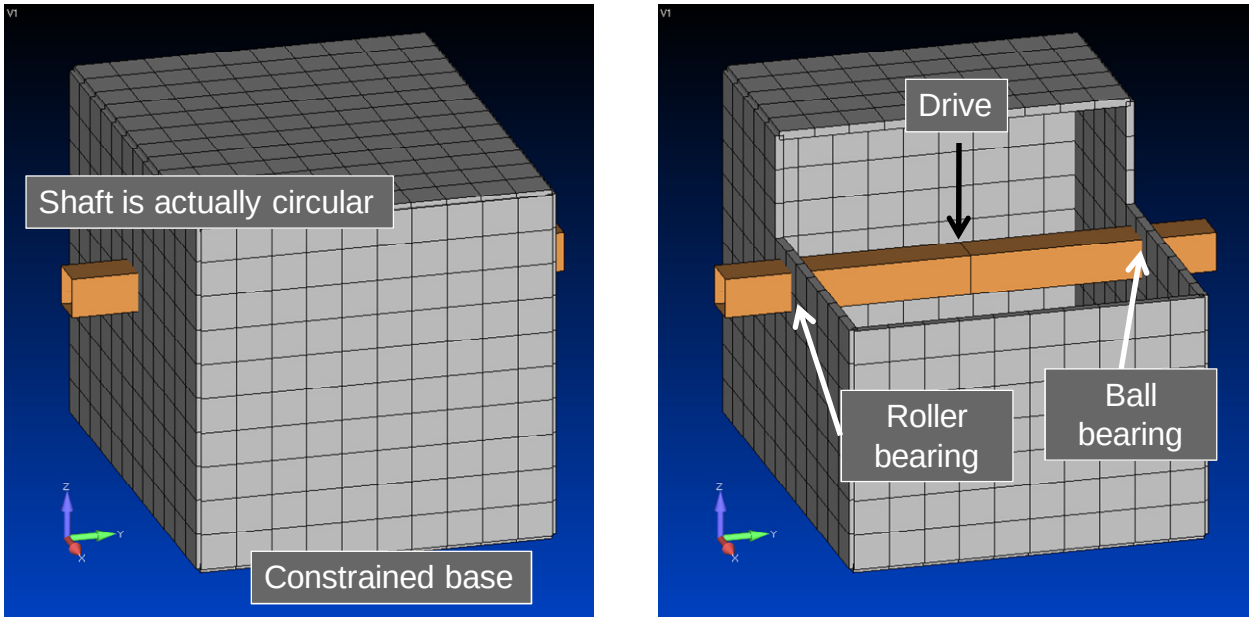

Figure 10. Finite element model of simplified gearbox with single shaft.

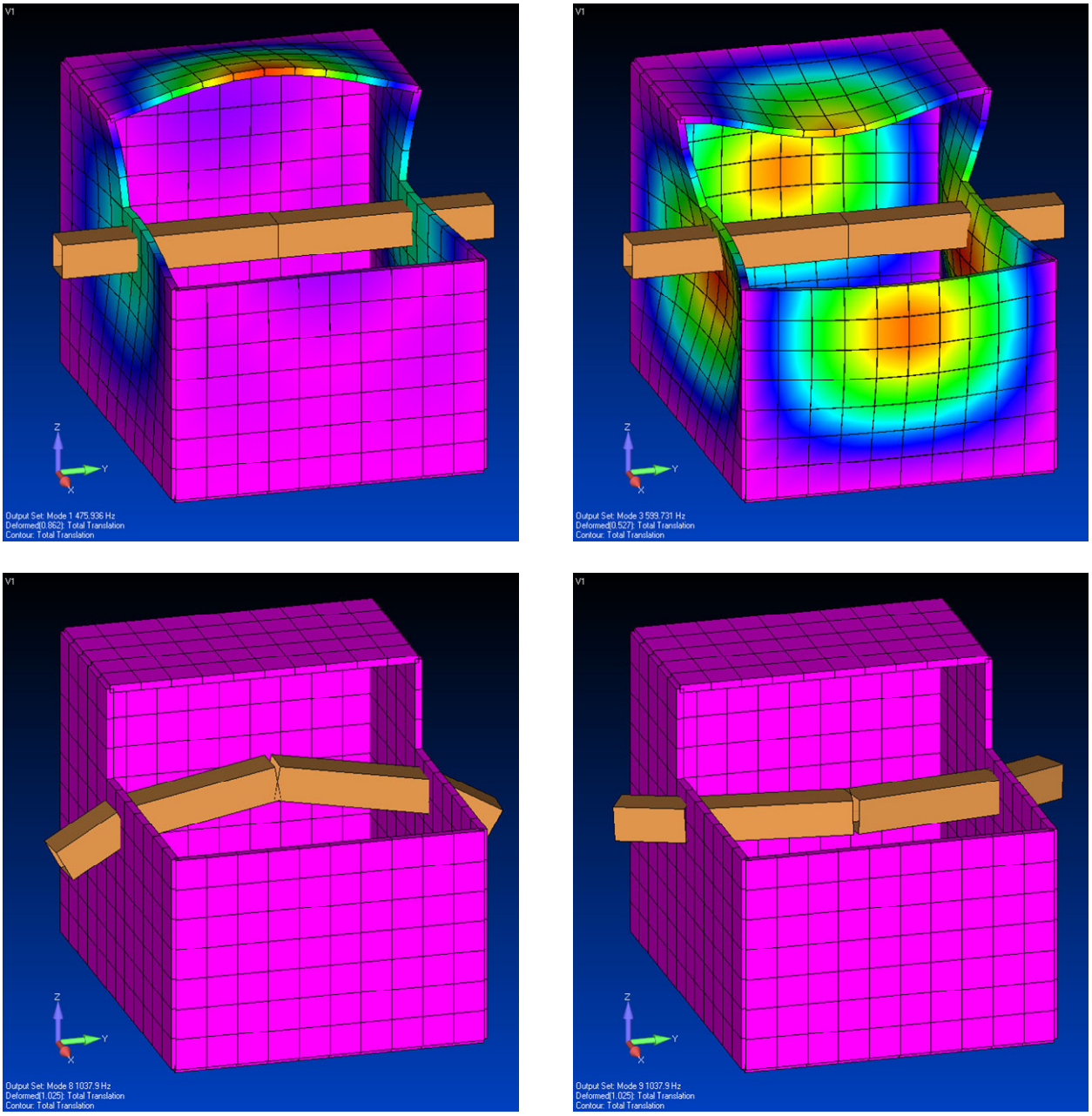

Figure 11. Sample mode shapes of housing (top) and shafting (bottom) of simplified gearbox model.

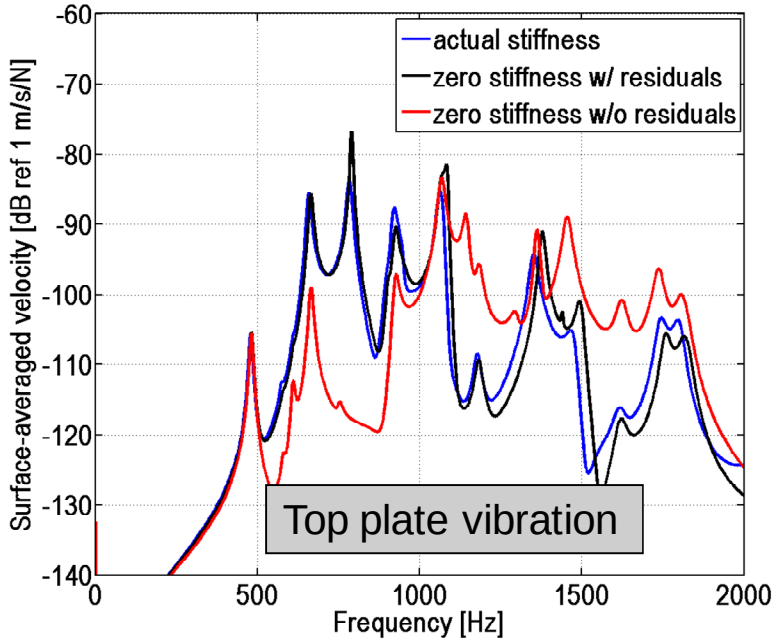

Figure 12. Top plate vibration of simplified gearbox. 'Actual stiffness' curve is the exact solution, and 'zero stiffness' curves are based on CMS solutions with and without residual vectors.

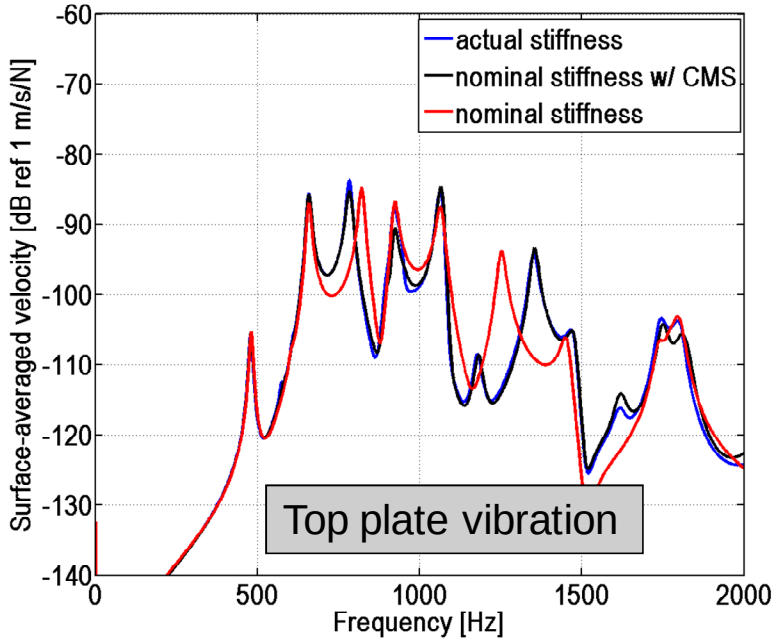

Figure 13. Top plate vibration of simplified gearbox. 'Actual stiffness' curve is the exact solution, and 'nominal stiffness' curves are shown with and without CMS.

3.3 Analytic Modeling of Rolling Element and Journal (Wave) Bearings

Both REBs and WBs are modeled analytically based on the geometric and physical bearing properties, along with the bearing operating conditions. Bearing impedances are nonlinear with applied load, and therefore must be recomputed and reapplied to the analysis at each torque condition. The impedances of journal bearings also vary with operating speed.

3.3.1 Rolling Element Bearings

Figure 14 shows a schematic of a ball bearing, along with a matrix relating bearing deformation with internal bearing forces. Roller bearings are similar to ball bearings, with cylindrical rather than spherical rolling elements. The bearings used in the NASA GRC test gearbox are shown in Figure 15. Bearing stiffness are finite in all directions except the rotational direction. The stiffness matrix includes several cross terms, where a load in the *x* direction is resisted by a stiffness in the *y* direction, for example.

As a rolling element, like a ball or roller, is loaded, a portion of its surface undergoes Hertzian deformation. As the load increases, more of the surface area deforms. Since the balls and rollers are not flat, the amount of surface under deformation does not increase linearly with loading. Also, as loading increases more balls and rollers are deformed, further complicating the relationships between load and deformation (and stiffness).

Complex [31, 32] and simplified [30] formulations of REB stiffnesses are available. The simplified formulas are useful for approximating the 'self' terms of the stiffness matrix in the radial and axial directions, but cannot be used to compute cross terms. For ball bearings, the radial and axial stiffnesses (in lbf/inch) are:

$$K_{radial} \cong 3.25E4 \cdot \sqrt[3]{DFZ^2 \cos^5 \alpha}, \quad K_{axial} \cong 9.49E4 \cdot \sqrt[3]{DFZ^2 \sin^5 \alpha},$$

where D is the ball diameter in inches, F is the applied load in lbf, Z is the number of balls, and α is the contact angle (a purely radial load implies a contact angle of 0, and no axial stiffness). The radial and axial stiffnesses of radial roller bearings are:

$$K_{radial} \cong 3.00E5 F^{0.1} Z^{0.9} l^{0.8} \cos^{1.9} \alpha, \quad K_{axial} \cong 1.28E6 F^{0.1} Z^{0.9} l^{0.8} \sin^{1.9} \alpha,$$

where l is the length of the roller elements in inches.

The Lim/Singh/Liew [31, 32] approach was implemented by ARL/Penn State and used to compute more accurate stiffnesses, including moment stiffnesses and cross-terms. Prior to applying the simple or complex formulas, the load resultants acting on a bearing must be known. Figure 16 shows the force and moment resultants at the bearings in the gearbox at 700 in-lb of torque as computed by Romax [25]. The rolling element bearings in the NASA GRC gearbox (see Figure 15) are different on each end of each shaft. Ball bearings (SKF Explorer 6205) are used for the shaft ends connected to external shafting, and roller bearings (FAG N205E) are used at the shaft free ends. The bearing types are indicated in Figure 16, along with the bearing numbers (the numbers are used later to label accelerometers mounted by NASA GRC on the outsides of the gearbox adjacent to the bearings). Figure 17 compares total radial stiffness/deflection and deflection/load curves for each rolling element bearing at several torques. All transverse and moment stiffnesses were computed using the Lim/Singh/Liew methodology for the 700 in-lb torque condition, and are shown in Table 4.

$$\begin{Bmatrix} F_x \\ F_y \\ F_z \\ M_x \\ M_y \\ M_z \end{Bmatrix} = \begin{bmatrix} k_{xx} & k_{yx} & k_{zx} & k_{\theta_x x} & k_{\theta_y x} & 0 \\ k_{xy} & k_{yy} & k_{zy} & k_{\theta_x y} & k_{\theta_y y} & 0 \\ k_{xz} & k_{yz} & k_{zz} & k_{\theta_x z} & k_{\theta_y z} & 0 \\ k_{x\theta_x} & k_{y\theta_x} & k_{z\theta_x} & k_{\theta_x\theta_x} & k_{\theta_y\theta_x} & 0 \\ k_{x\theta_y} & k_{y\theta_x} & k_{z\theta_x} & k_{\theta_x\theta_y} & k_{\theta_y\theta_y} & 0 \\ 0 & 0 & 0 & 0 & 0 & 0 \end{bmatrix} \cdot \begin{Bmatrix} \delta_x \\ \delta_y \\ \delta_z \\ \beta_x \\ \beta_y \\ \beta_z \end{Bmatrix}$$

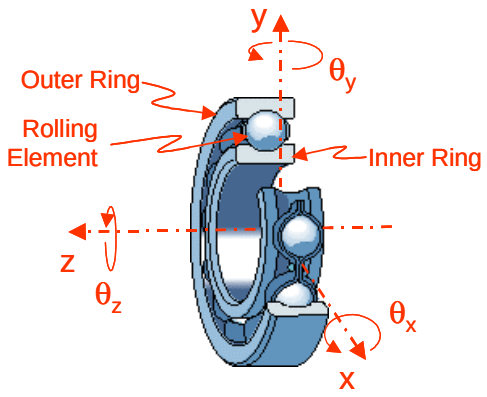

Figure 14. Ball bearing schematic and force-displacement relationships.

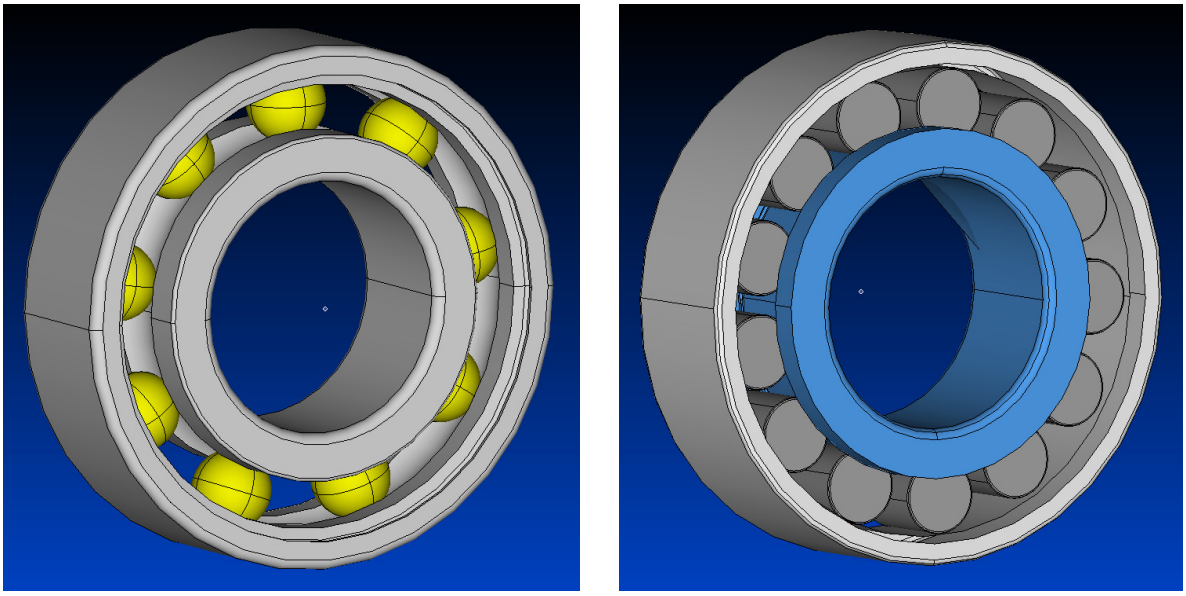

Figure 15. SKF Explorer 6205 Ball Bearing (left) and FAG N205E roller bearing (right).

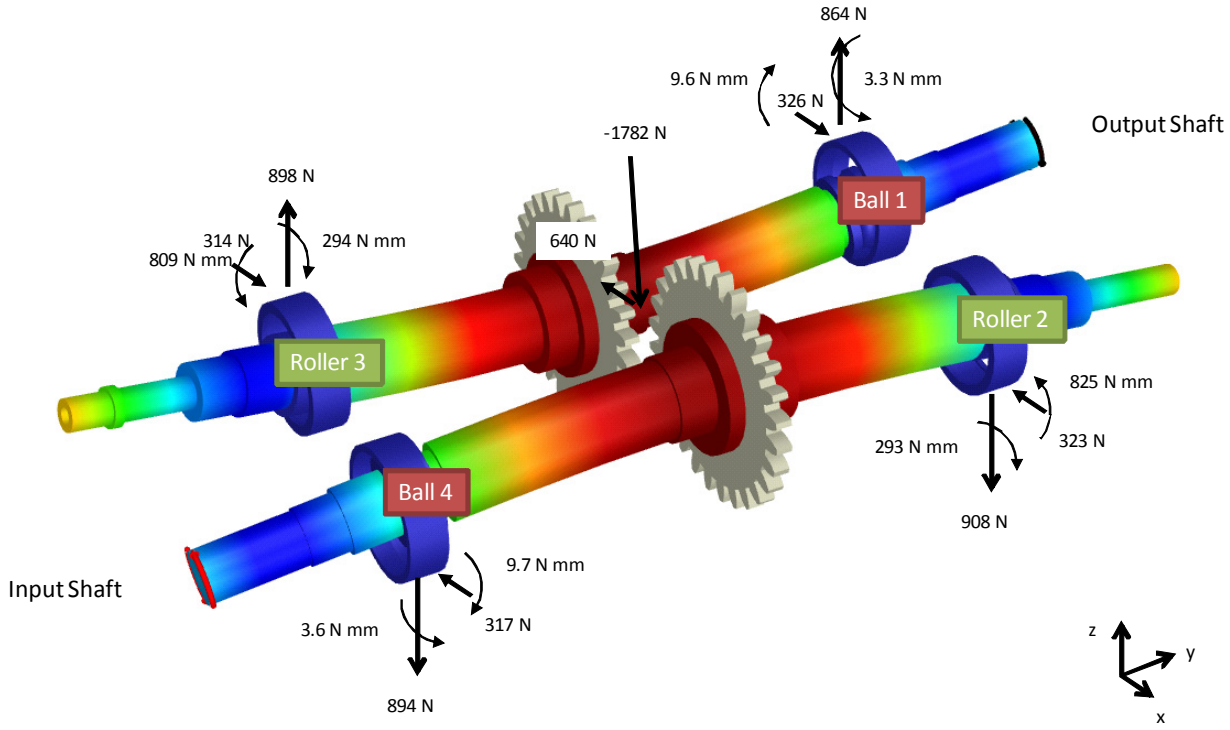

Figure 16. Force and moment resultants at 700 in-lb of torque for shafts and bearings, as computed by Romax software.

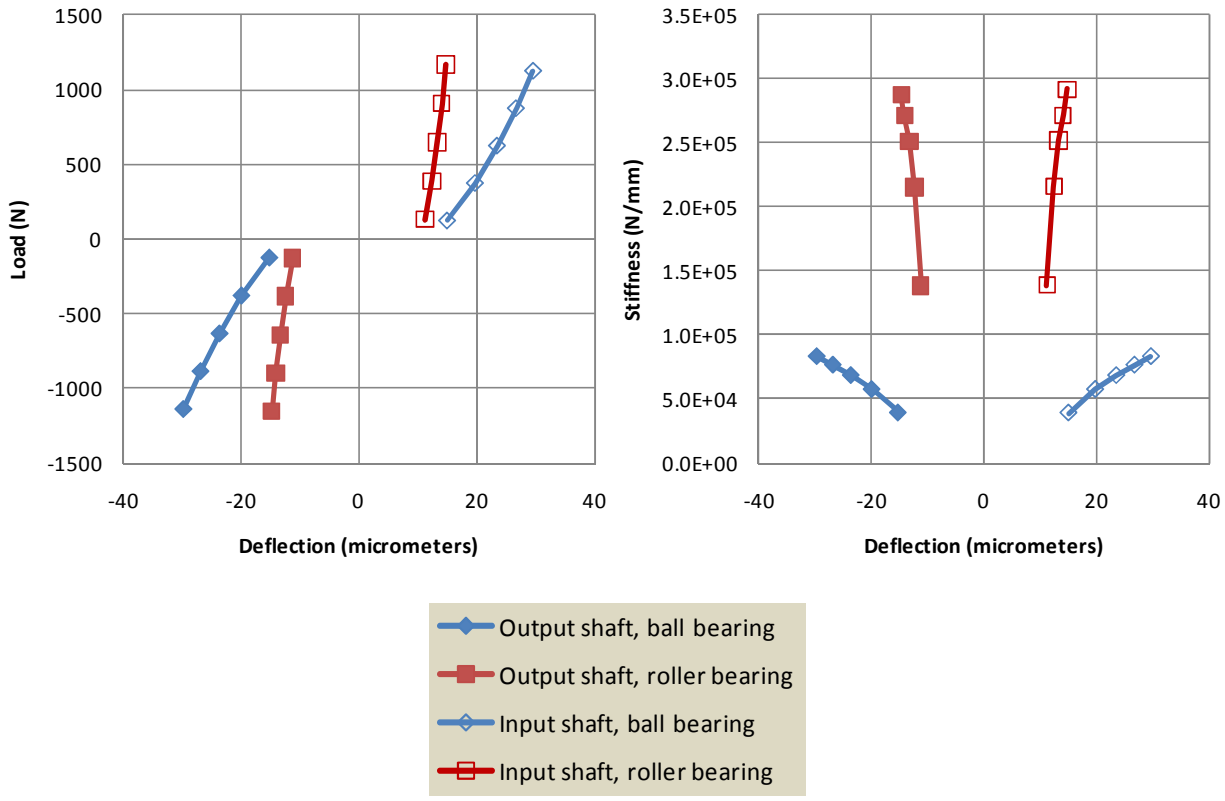

Figure 17. Radial load-deflection and stiffness-deflection curves for NASA GRC gearbox ball and roller bearings.

ARL - Full Matrix (Ball 1), N, mm, rad						
	x	y	z	rx	ry	rz
x	66600					
y	6735	49400				
z	4	-10	933			
rx	1600	-3595	5220	118000		
ry	248	-1525	-13800	-51250	226000	
rz	0	0	0	0	0	0

ARL - Full Matrix (Roller 2), N, mm, rad						
	x	y	z	rx	ry	rz
x	249000					
y	87300	50000				
z	67	24	0			
rx	8775	5050	2	306000		
ry	-25450	-8865	-7	-534000	1520000	
rz	0	0	0	0	0	0

ARL - Full Matrix (Roller 3), N, mm, rad						
	x	y	z	rx	ry	rz
x	279000					
y	70600	57800				
z	65	24	0			
rx	-66750	-84400	-29	368000		
ry	150000	66750	40	-460000	1610000	
rz	0	0	0	0	0	0

ARL - Full Matrix (Ball 4), N, mm, rad						
	x	y	z	rx	ry	rz
x	66700					
y	7530	50100				
z	-2	3	958			
rx	-1135	3670	-5050	116000		
ry	-275	1215	14300	-45300	238000	
rz	0	0	0	0	0	0

Table 4. Ball and roller bearing stiffnesses (in bearing coordinate system: x downward, y horizontal, z along shaft axis) for NASA GRC test gearbox at 700 in-lb torque, computed with ARL/Penn State implementation of the Lim/Singh/Liew methodology.

3.3.2 Journal and Wave Bearings

The rolling element bearings in the NASA GRC gearbox were replaced with journal/wave bearings, as shown in the CAD image in Figure 18. Journal bearings support loads through a fluid film between the shaft and bearing surfaces. As the shaft rotates, a shear layer is formed in the fluid film which supports the load. Wave bearings are fluid film journal bearings with multi-lobed wave patterns around the circumference of the bearing surface [2, 3]. Under this project, ARL/Penn State developed a wave bearing software suite [39], which is a Matlab application that computes bearing properties for user specified wave bearing conditions as well as plain journal bearings. The dynamic coefficients are output in a way for easy implementation in a finite element model used in rotor dynamics analyses.

A three-lobed wave journal bearing geometry is shown in Figure 19. Generally speaking, under normal operating conditions, the N -wave bearing will develop N converging fluid regions around the circumference to support the applied load. The software first determines where the active film regions are and then performs the necessary computation within each of those fluid regions to compute the equilibrium journal location. Once the journal location has been determined, the bearing dynamic coefficients can be computed at that location.

The terms used to define a wave bearing are:

e: Eccentricity,
ε: Eccentricity ratio =*e/C,*
D: Bearing diameter (nominal),
h: Film thickness,
W: Applied load,
ϕ: Attitude angle,
Ω: Shaft speed, and
C: Radial clearance.

The wave bearing impedances are computed based on an extension to the method described by Campbell [40] for regular journal bearings. In Campbell's approach, the pressure field in the fluid film between the shaft and bearing surface is computed by solving the Reynolds Equation using finite difference methods. The external load that can be supported by the bearing is calculated by integrating the pressure over the film surface. The dynamic stiffness and damping coefficients are then related to the reaction forces by a Taylor series expansion. The circumferentially varying stiffness and damping is then integrated to compute the overall impedances in the vertical and horizontal directions. For wave bearings, the circumferentially varying film thickness is augmented with a three lobed wave profile (any number of lobes may be considered, but the NASA GRC wave bearings have three lobes). For details on the procedure, see [39].

The NASA GRC journal and wave bearing parameters are shown in Table 5 and Table 6. The bearing lubricant (MobilJet2, MilSpec 23699) is pumped into the fluid film gap at about 70 degrees C between the bearing and shaft through three small ports spaced equidistantly around the circumference. The effects of the inlet pressure on the fluid film is minimal, and need not be considered in the modeling of the bearing coefficients (see Appendix A of [39]). For this example, impedances were computed at four rotational speeds and at 700 in-lb of torque. A wave amplitude of 40% of the undeformed gap thickness was modeled.

The pressures in the fluid film are close to the ambient pressure except in the regions where the film is squeezed (the convergent region). There is only one convergent region in a simple journal bearing, but there are three convergent regions for the three-lobed wave bearings. Figure 20 compares the pressure distributions in the fluid films of journal and wave bearings at 3000 rpm. The multiple high pressure regions are evident in the wave bearing distribution, and the wave bearing pressures are higher than those in the simple journal bearing.

Figure 21 and Figure 22 compare the circumferentially varying radial stiffness and damping terms for the journal and wave bearings (again at 3000 rpm and 700 in-lb). The peak stiffnesses are higher in the wave bearing, and the peak damping levels are comparable for both bearings. The figures also show that the cross-terms (k_{xy} and k_{yx}, b_{xy} and b_{yx}) are different, leading to non-symmetric stiffness matrices. The non-symmetric matrices are handled easily in the CHAMP CMS analyses, but would be difficult to work with in a traditional FE analysis, since non-symmetric matrices lead to much longer computational times.

Moment stiffnesses and damping of the journal and wave bearings are also computed using a numerical perturbation technique. The bearing forces and moments are computed for a prescribed journal location and then the journal location is perturbed in both translational and rotational directions and the forces and moments recomputed. The secant method is then used to estimate the slope of the load-deflection curve (i.e., the stiffness). The moment damping terms are not so easily computed, however, and are estimated based on the ratios of the translational damping and stiffness terms. Damping for the cross terms (translational to moment), are ignored, but should be investigated in the future. For more details, see Appendix B of [39].

The stiffnesses and damping are integrated around the bearing circumference to compute total vertical and horizontal impedances for both direct and cross terms. Table 7 and Table 8 list the full stiffness matrices for the journal and wave bearings for the 700 in-lb torque condition. Note that the matrices are nonsymmetric. Figure 23 compares the total radial stiffnesses and moment stiffnesses (magnitude of the x and y components) for wave and plain journal bearings as a function of rotational speed. Note that the impedances for all four journal bearings are identical, since the shafts and gears are symmetric with respect to the gearbox. Also shown on the plots are the radial and rotational stiffnesses for the ball and roller bearings on the input side of the gearbox. In the translational direction, the roller bearings are stiffer than the plain journal (and ball) bearings, but are less stiff than the wave bearings. The wave bearings, however, are stiffer than the journal bearings. Finally, while the plain journal bearing radial stiffnesses are fairly constant with rotational speed, the wave bearings stiffen significantly with increasing rotational speed. In the rotational direction, the journal and wave bearings are stiffer than the roller bearings above 2500 rpm, with the journal bearings having the highest rotational stiffnesses. The journal and wave bearing rotational stiffnesses also increase significantly with increasing rotational speed.

Table 9 and Table 10 list the full damping matrices for the journal and wave bearings. Whereas the stiffness matrices are non-symmetric, the damping matrices are symmetric. Note that cross terms between the translational and rotational damping are not currently computed. Figure 24 compares total damping in the radial directions for the journal and wave bearings at 700 in-lb torque and varying

rotational speeds. As a point of comparison, ball and roller bearing damping typically varies between 0.1 and 0.5 N/mm/s [41], values more than three orders of magnitude less than the damping in the wave and journal bearings. The wave bearings have lower damping than the journal bearings. Also, damping decreases slightly with increasing rotational speed for both journal and wave bearings.

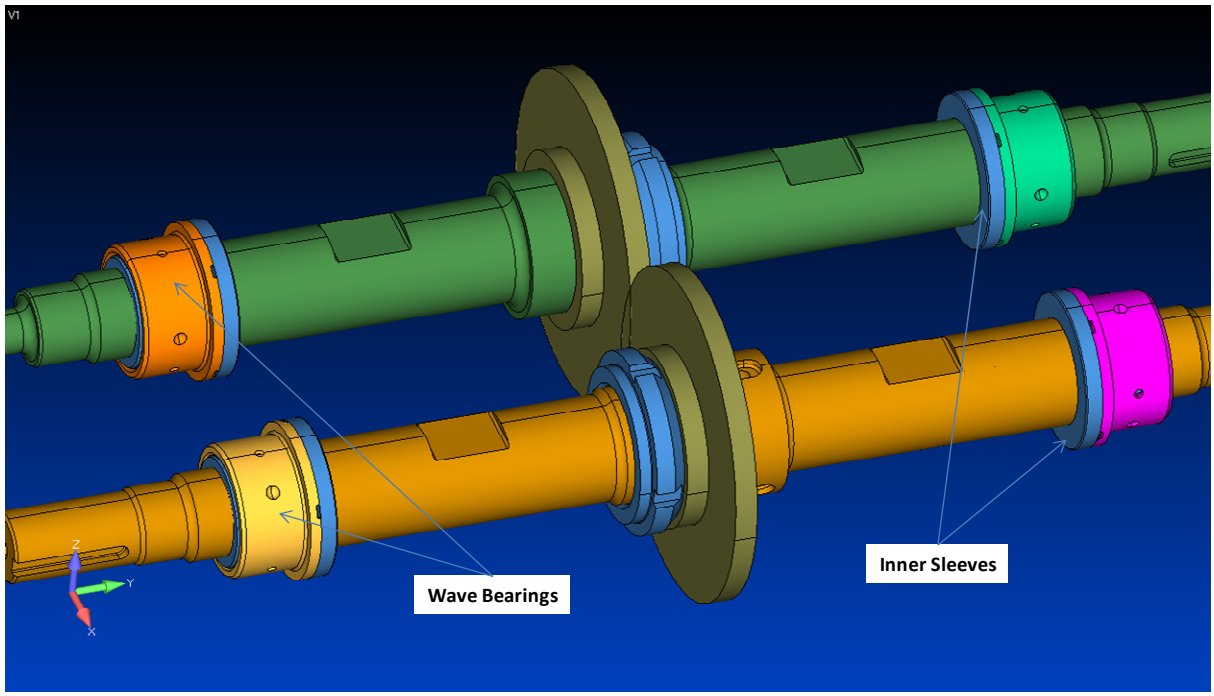

Figure 18. CAD image of the NASA GRC gearbox shafting shown with wave bearings.

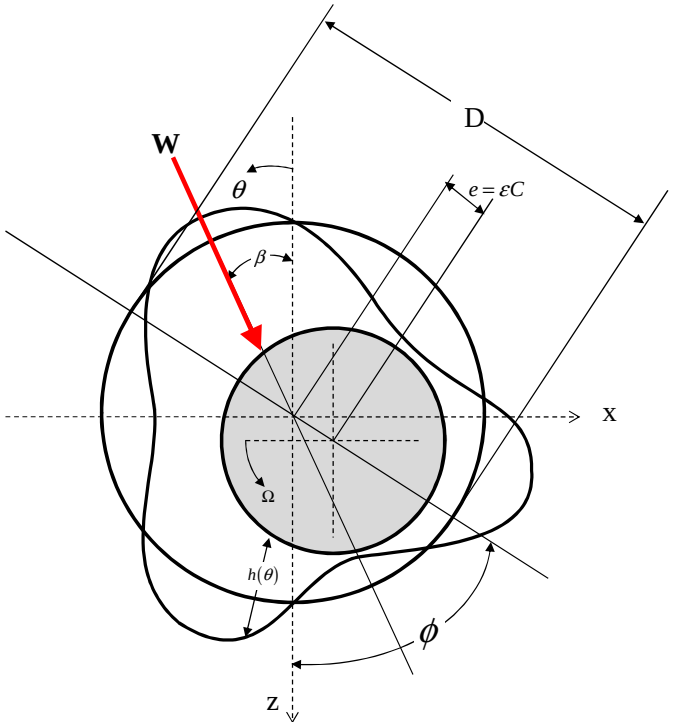

Figure 19. Wave bearing geometry (wave profile greatly exaggerated).

Fluid viscosity	μ = 0.0294 Pa s
Fluid density	ρ = 980 kg/m^3
Journal diameter	D = 0.03195 m
Radial clearance	C = 15 μm
Bearing length	L = 0.019882 m
Rotation speed	Ω = 50 Hz
Number of waves	N_w = 0
Wave amplitude ratio	ε_w = 0
Wave profile offset angle	β = 0˚

Table 5. Journal bearing parameters.

Fluid viscosity	μ = 0.0294 Pa s
Fluid density	ρ = 980 kg/m^3
Bearing diameter	D = 0.03195 m
Radial clearance	C = 15 μm
Bearing length	L = 0.019882 m
Rotating speed	Ω = 50 Hz
Number of waves	N_w = 3
Wave amplitude ratio	ε_w = 0.4
Wave profile offset angle	β = 20˚

Table 6. Wave bearing parameters.

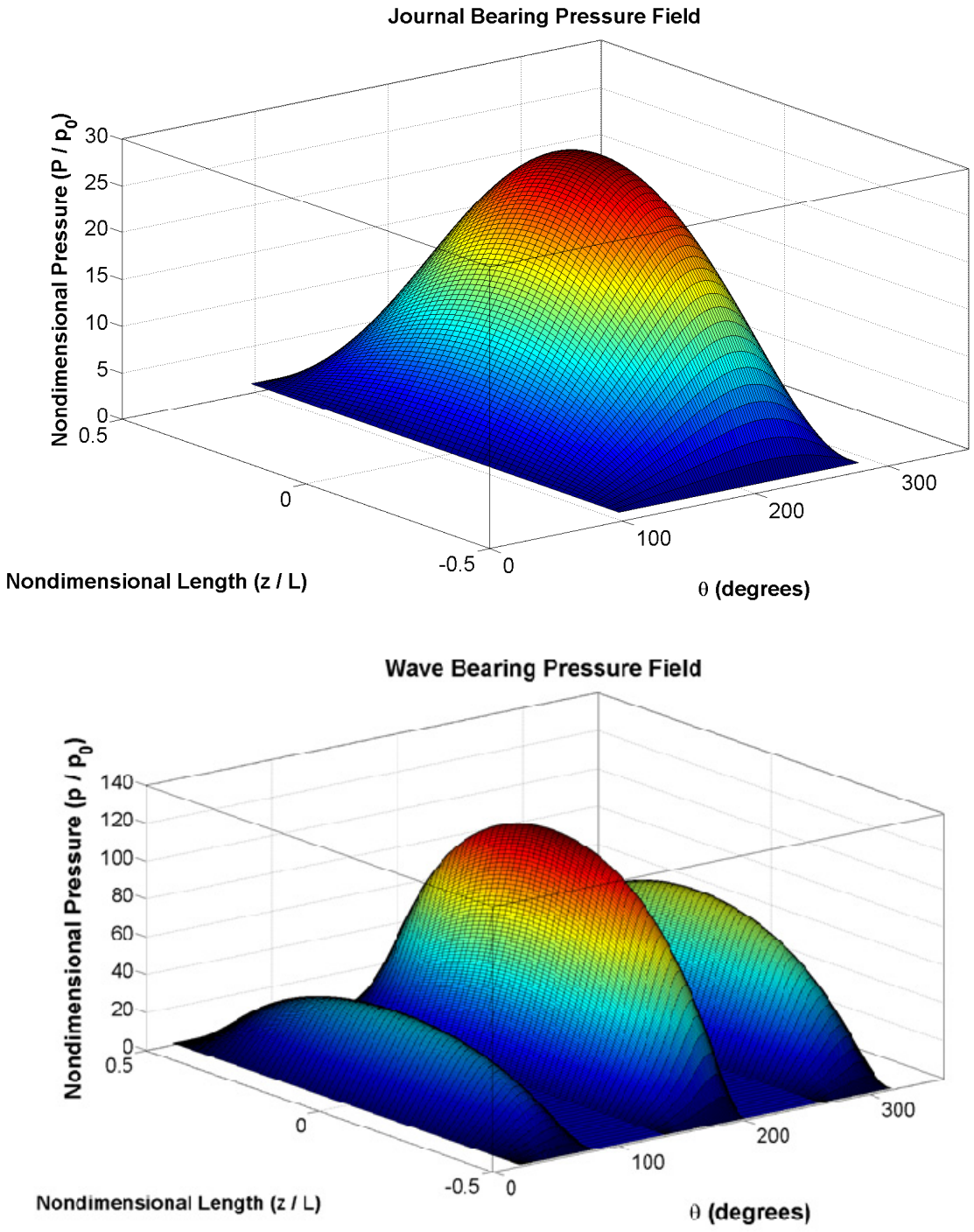

Figure 20. Normalized pressure (pressure normalized by atmospheric pressure) distributions for traditional journal bearing (top) and wave bearing (bottom) at 700 in-lb torque and 3000 rpm.

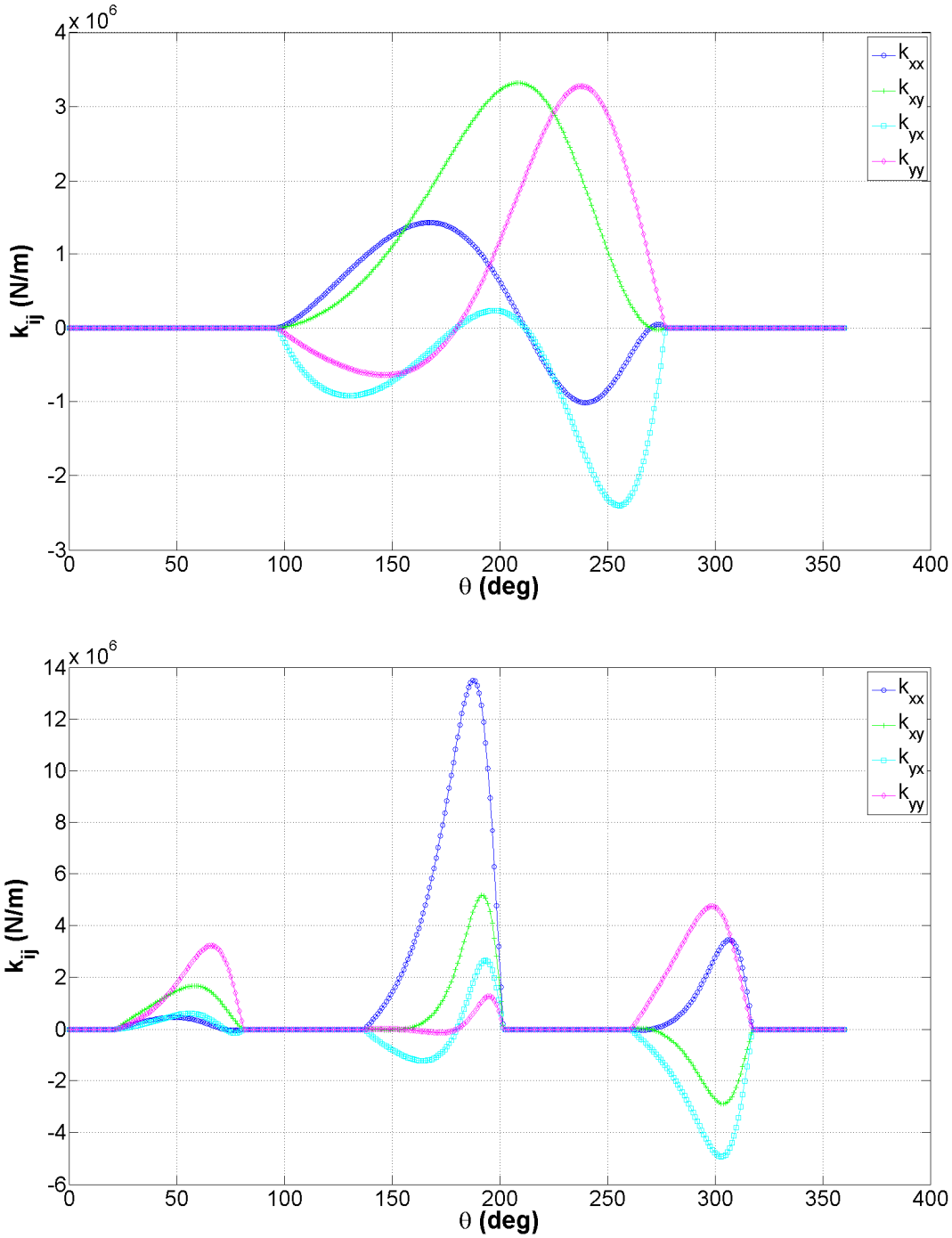

Figure 21. Journal (top) and wave (bottom) bearing stiffness coefficients around the bearing circumference at 700 in-lb torque and 3000 rpm.

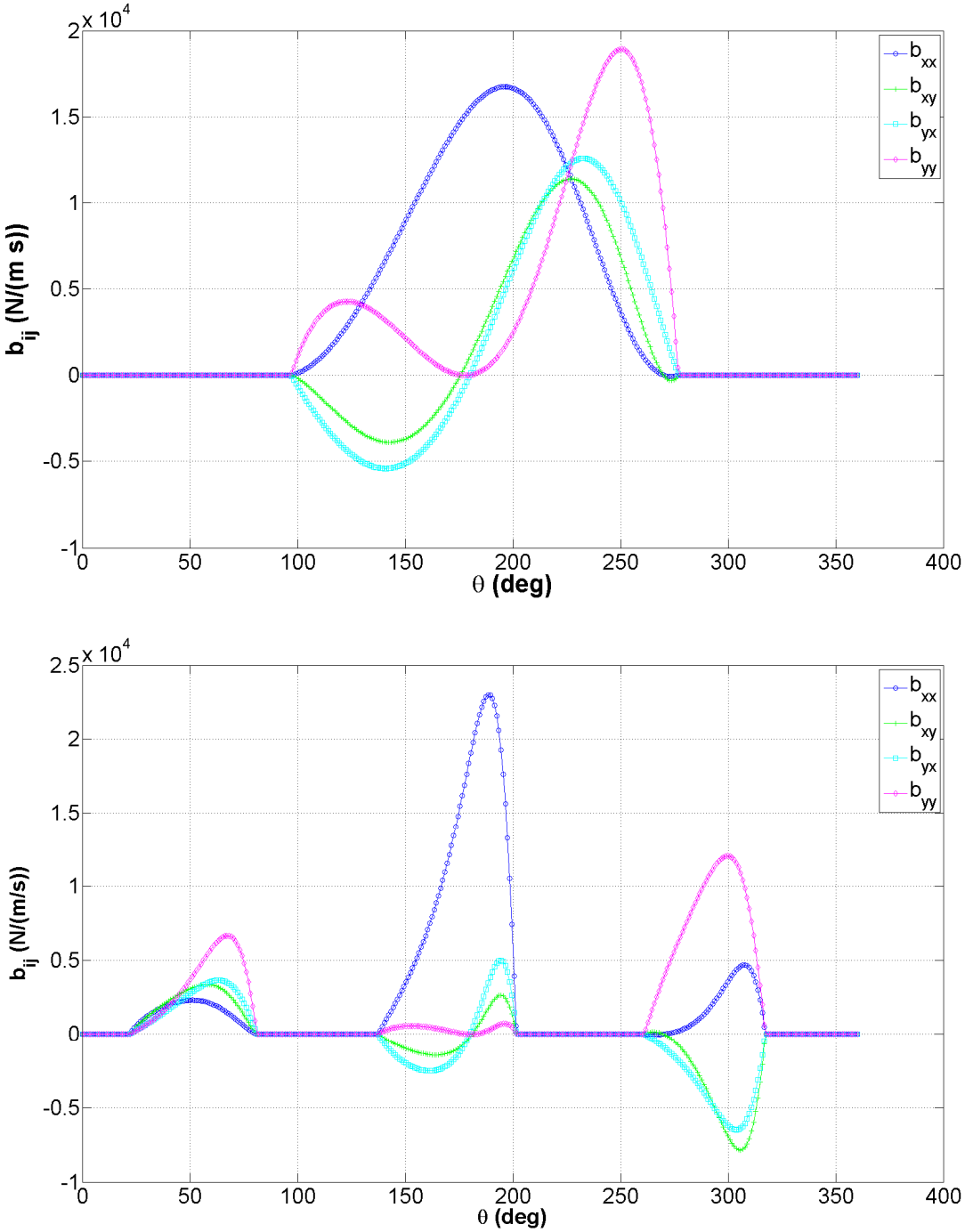

Figure 22. Journal (top) and wave (bottom) bearing damping coefficients around the bearing circumference at 700 in-lb torque and 3000 rpm.

2000 rpm - Full Matrix, N, mm, rad						
	x	y	z	rx	ry	rz
x	8.48E+04	2.27E+05	0	1.20E+05	4.55E-04	0
y	-7.73E+04	1.53E+05	0	6.56E+04	6.64E-04	0
z	0	0	0	0	0	0
rx	3.07E+04	-2.58E+04	0	-1.61E+04	2.05E-06	0
ry	-1.07E+04	-3.82E+04	0	-2.64E+04	2.14E-06	0
rz	0	0	0	0	0	0

3000 rpm - Full Matrix, N, mm, rad						
	x	y	z	rx	ry	rz
x	7.05E+04	2.79E+05	0	1.20E+05	4.55E+04	0
y	-1.32E+05	1.56E+05	0	6.56E+04	6.64E+04	0
z	0	0	0	0	0	0
rx	3.07E+04	-2.58E+04	0	1.66E+05	2.04E+06	0
ry	-1.07E+04	-3.82E+04	0	1.74E+05	2.24E+06	0
rz	0	0	0	0	0	0

4000 rpm - Full Matrix, N, mm, rad						
	x	y	z	rx	ry	rz
x	5.96E+04	3.40E+05	0	1.20E+05	4.55E-04	0
y	-1.83E+05	1.62E+05	0	6.56E+04	6.64E-04	0
z	0	0	0	0	0	0
rx	3.07E+04	-2.58E+04	0	2.80E+05	2.11E-06	0
ry	-1.07E+04	-3.82E+04	0	3.21E+05	2.52E-06	0
rz	0	0	0	0	0	0

5000 rpm - Full Matrix, N, mm, rad						
	x	y	z	rx	ry	rz
x	4.95E+04	4.06E+05	0	1.20E+05	4.55E+04	0
y	-2.33E+05	1.70E+05	0	6.56E+04	6.64E+04	0
z	0	0	0	0	0	0
rx	3.07E+04	-2.58E+04	0	3.58E+05	2.22E+06	0
ry	-1.07E+04	-3.82E+04	0	4.47E+05	2.88E+06	0
rz	0	0	0	0	0	0

Table 7. Journal bearing stiffness matrices (in bearing coordinate system: x downward, y horizontal, z along shaft axis) for 700 in-lb torque condition and four operational speeds.

2000 rpm - Full Matrix, N, mm, rad						
	x	y	z	rx	ry	rz
x	3.96E+05	6.87E+04	0	1.20E+05	4.55E-04	0
y	-8.79E+04	1.75E+05	0	6.56E+04	6.64E-04	0
z	0	0	0	0	0	0
rx	3.07E+04	-2.58E+04	0	9.40E+05	3.07E-06	0
ry	-1.07E+04	-3.82E+04	0	-7.17E+06	1.02E-06	0
rz	0	0	0	0	0	0

3000 rpm - Full Matrix, N, mm, rad						
	x	y	z	rx	ry	rz
x	4.71E+05	8.97E+04	0	1.20E+05	4.55E+04	0
y	-1.26E+05	2.56E+05	0	6.56E+04	6.64E+04	0
z	0	0	0	0	0	0
rx	3.07E+04	-2.58E+04	0	1.44E+06	4.45E+06	0
ry	-1.07E+04	-3.82E+04	0	-8.31E+06	1.11E+06	0
rz	0	0	0	0	0	0

4000 rpm - Full Matrix, N, mm, rad						
	x	y	z	rx	ry	rz
x	5.59E+05	1.17E+05	0	1.20E+05	4.55E-04	0
y	-1.61E+05	3.47E+05	0	6.56E+04	6.64E-04	0
z	0	0	0	0	0	0
rx	3.07E+04	-2.58E+04	0	1.88E+06	5.96E-06	0
ry	-1.07E+04	-3.82E+04	0	-9.79E+06	1.38E-06	0
rz	0	0	0	0	0	0

5000 rpm - Full Matrix, N, mm, rad						
	x	y	z	rx	ry	rz
x	6.53E+05	1.46E+05	0	1.20E+05	4.55E+04	0
y	-1.96E+05	4.41E+05	0	6.56E+04	6.64E+04	0
z	0	0	0	0	0	0
rx	3.07E+04	-2.58E+04	0	2.30E+06	7.56E+06	0
ry	-1.07E+04	-3.82E+04	0	-1.13E+07	1.66E+06	0
rz	0	0	0	0	0	0

Table 8. Wave bearing stiffness matrices (in bearing coordinate system: x downward, y horizontal, z along shaft axis) for 700 in-lb torque condition and four operational speeds.

2000 rpm - Full Matrix, N, mm, rad						
	x	y	z	rx	ry	rz
x	1.70E+03	6.13E+02				
y	6.13E+02	1.26E+03				
z						
rx				-3.22E+02	2.87E+03	
ry				2.87E+03	1.76E+04	
rz						

3000 rpm - Full Matrix, N, mm, rad						
	x	y	z	rx	ry	rz
x	1.51e3	4.55e2				
y	4.55e2	1.13e3				
z						
rx				3.56e3	1.36e3	
ry				1.36e3	1.62e4	
rz						

4000 rpm - Full Matrix, N, mm, rad						
	x	y	z	rx	ry	rz
x	1.45e3	3.82e2				
y	3.82e2	1.07e3				
z						
rx				6.80e3	8.50e2	
ry				8.50e2	1.66e4	
rz						

5000 rpm - Full Matrix, N, mm, rad						
	x	y	z	rx	ry	rz
x	1.42e3	3.40e2				
y	3.40e2	1.03e3				
z						
rx				1.03e4	6.04e2	
ry				6.04e2	1.75e4	
rz						

Table 9. Journal bearing damping matrices (in bearing coordinate system: x downward, y horizontal, z along shaft axis) for 700 in-lb torque condition and four operational speeds.

2000 rpm - Full Matrix, N, mm, rad						
	x	y	z	rx	ry	rz
x	1.04e3	-8.93e1				
y	-8.93e1	6.56e2				
z						
rx				2.45e3	-5.64e3	
ry				-5.64e3	3.81e3	
rz						

3000 rpm - Full Matrix, N, mm, rad						
	x	y	z	rx	ry	rz
x	8.94e2	7.20e1				
y	7.20e1	6.39e2				
z						
rx				2.74e3	-4.16e3	
ry				-4.16e3	2.76e3	
rz						

4000 rpm - Full Matrix, N, mm, rad						
	x	y	z	rx	ry	rz
x	8.33e2	-5.88e1				
y	-5.88e1	6.40e2				
z						
rx				2.80e3	-3.28e3	
ry				-3.28e3	2.54e3	
rz						

5000 rpm - Full Matrix, N, mm, rad						
	x	y	z	rx	ry	rz
x	7.99e2	-4.93e1				
y	-4.93e1	6.44e2				
z						
rx				2.82e3	-2.70e3	
ry				-2.70e3	2.42e3	
rz						

Table 10. Wave bearing damping matrices (in bearing coordinate system: x downward, y horizontal, z along shaft axis) for 700 in-lb torque condition and four operational speeds.

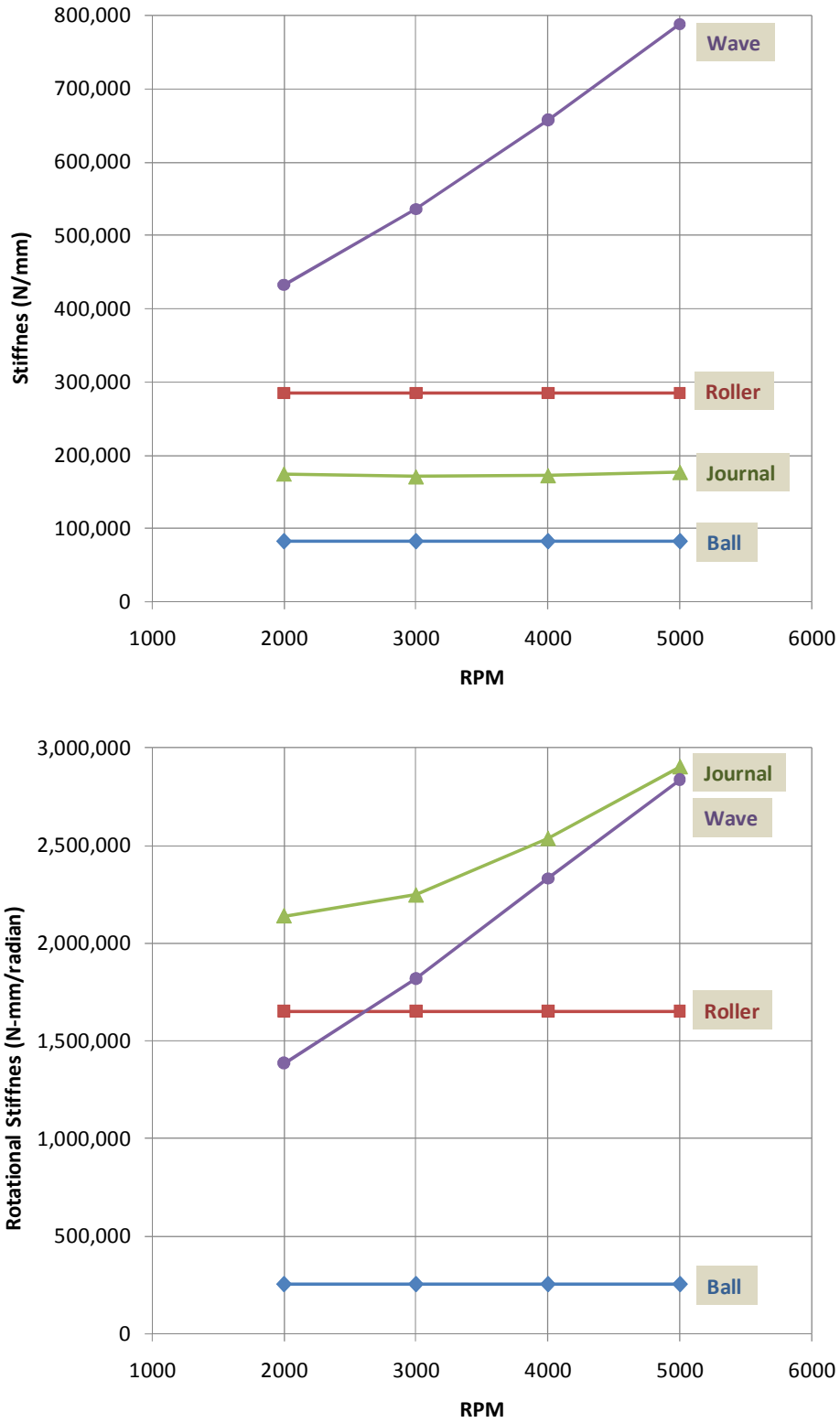

Figure 23. Comparison between journal and wave bearing radial stiffnesses (top) and rotational stiffness magnitudes (bottom) to those of ball and roller bearings at input side of gearbox at 700 in-lb torque.

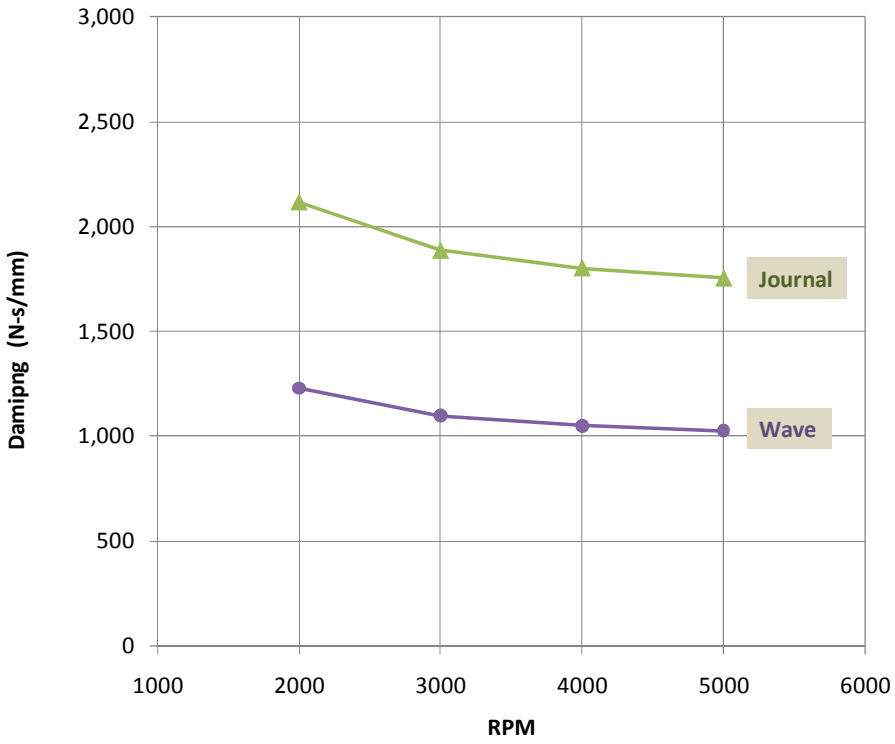

Figure 24. Journal and wave bearing radial damping at 700 in-lb torque and variable rpm.

3.4 Verification of Gearbox Model with Rolling Element Bearings

Penn State conducted structural-dynamic measurements of the NASA GRC gearbox for two configurations: the first test with stiff shaft couplings between the gearbox and external shafts, and the second with soft shaft couplings and rubber pads between the feet of the gearbox and the lower support structure. Both sets of measurements were conducted with a non-operational gearbox with ball and roller bearings installed, and with static torque applied to the input shaft to simulate operating conditions near 300 in-lb and 700 in-lb. The FE model, however, was exercised assuming rigid connectivity between the gearbox and lower support structure, and soft couplings between the gearbox and external shafts, since future NASA operating gearbox measurements were made with that configuration.

Figure 25 shows images of the testing configurations. One set of measurements was conducted with the top plate attached to the housing, and another set with the plate removed, allowing access to the gears and internal shafting. Mode shapes of the internal shafting and gearbox were measured, along with several sets of transfer functions between drive and response locations. Using reciprocity, all reference accelerometers become 'drives', while all points driven with an instrumented dynamic force hammer become response locations. Several surface-averaged responses over arrays of drive points with respect to virtual drives at the reference accelerometers are computed. The test data is used to guide and verify the gearbox and shafting FE modeling.

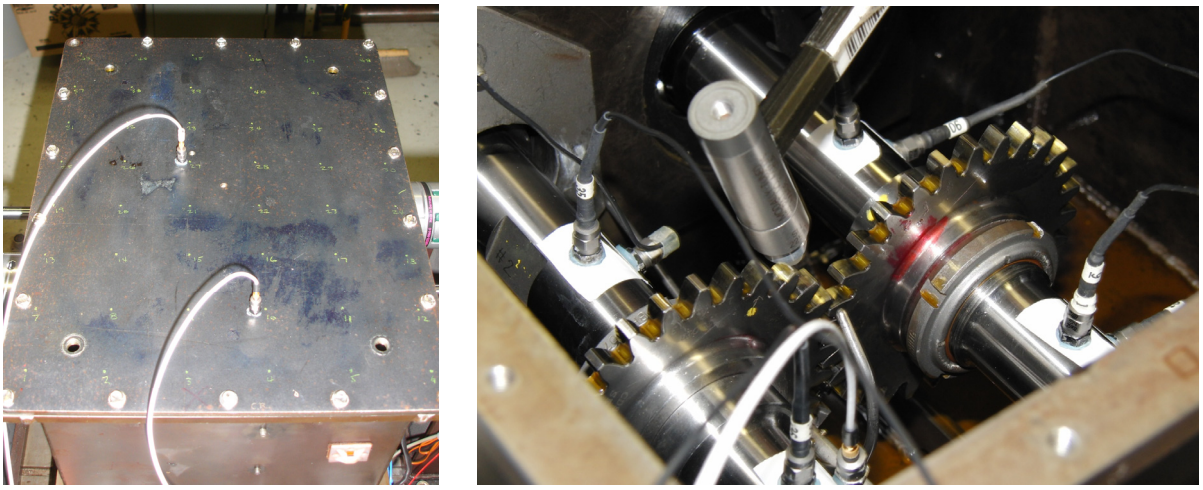

Figure 25. Accelerometers mounted to gearbox cover (left) and to gear shafts (right), along with force hammer impacting gear teeth.

3.4.1 Fundamental shafting and housing modes

Gearbox vibrations are based on the modes of the internal shafting and the modes of the housing. Since the shafting and housing are strongly coupled by the bearings, many mode shapes and resonance frequencies differ significantly from those of the uncoupled systems (the shafts and housing by themselves, without the coupling effects of the bearings). The modes computed using the FE model are compared here to various sets of measurements made on the NASA GRC test gearbox for the rolling element bearing configuration. Data for two configurations are compared – with and without the housing lid attached.

3.4.1.1 Shafting Modes

Examples of coupled shaft/gearbox modes are shown in Figure 26. Some shafting modes couple strongly with the gearbox, such as the mode on the left, while others do not. The degree of coupling depends on the amount of transverse and rotational motion of the shafts at the bearing locations. To verify the modeling of the shafting, along with its coupling to the housing, simulated and measured shafting vibration response and modes are compared with the housing lid removed. Figure 27 compares averaged drive point accelerances measured and simulated over the input and output shafts. The accelerances were measured and computed over several points along the shafting on either side of the gears, in the vertical and horizontal directions (see Figure 1 and Figure 25 for an example of accelerometer locations on the shafting). The critical groups of shaft bending modes are clearly visible in the plots. The frequencies, amplitudes, and character of the plots agree well, with the exception of the third mode cluster peak, which is apparent in the simulated results (near 3500 Hz), but not in the measurements. The measurement coherence was poor above about 3 kHz, so that the modes above that frequency could not be measured. Also, the frequencies of the second cluster of shaft bending modes between 2 and 3 kHz are underestimated by the FE model, most likely due to errors in the assumed impedances of the flexible couplings attached to the ends of the input and output shafts.

The shapes of the first three shaft bending mode types are shown in Figure 28. A few of the shafting mode shapes were successfully extracted from the measured accelerances, and compare well with the simulated mode shapes. To compare the mode shapes, the plotting convention shown in Figure 29 was adopted, where the mode shapes of the input and output shafts are shown in the vertical and horizontal directions. Figure 30 compares a measured and simulated mode shape near 800 Hz. For this mode, the shafts vibrate primarily in the vertical direction, with node lines (points of near zero vibration) near the bearings. Table 11 compares the resonance frequencies of measured and simulated mode shapes for the first two mode orders, denoted n=2 (the fundamental mode, with two node lines – both near the bearings) and n=3 (the next order mode group, with three node lines). The simulated and measured frequencies are similar, with the FE model slightly underestimating the frequencies of the n=3 modes.

It is clear from Figure 27 that there are several bending modes in each grouping near 800 and 2500 Hz, with some primarily vibrating in the vertical direction, and others vibrating horizontally. To investigate the cause of this modal 'spreading', the FE model is exercised for several conditions (this time with the lid attached), with the shafts:

a. completely uncoupled;

b. connected by the gear meshing stiffness in the LOA direction;

c. connected by gear meshing stiffness, and bearing stiffnesses, but assuming a rigid housing; and

d. connected by gear meshing stiffness and bearing stiffness, but with a flexible housing.

Figure 31, Figure 32, and Figure 33 show examples of how selected n=2, n=3, and n=4 shafting bending modes are affected by the addition of gear meshing stiffness, bearing stiffness, and housing flexibility. Each mode type has at least four different variations, with dominant motions in the input or output shaft, and in the vertical or horizontal directions. The free shaft modes are pure, with a single shaft vibrating in the vertical or horizontal direction. Coupling the shafts with the gear meshing stiffness causes both shafts to vibrate, and 'rotates' the mode shapes about the shaft axes, leading to strong vibration in both the vertical and horizontal directions, but has little effect on the resonance frequencies. Adding the bearing stiffnesses increases the resonance frequencies significantly, and further modifies the shaft vibration patterns. Including housing flexibility further changes the vibration patterns and resonance frequencies. Figure 34 summarizes the changes in resonance frequencies, along with the spread in resonance frequencies, for each mode group. The strongest effect on the resonance frequencies, not surprisingly, is caused by the addition of bearing stiffnesses. Including housing flexibility increases the 3rd and 4th order mode resonance frequencies slightly, and has little effect on the frequencies of the 2nd order modes.

Torsional modes also exist in the shafting, where the gear teeth act as springs and the shafts rotate about their axes. These modes can amplify gear transmission error at specific rotational speeds, but may not necessarily generate strong gearbox housing vibration or radiated sound, since the majority of the shaft motion is rotational, and not translational. Figure 35 shows the fundamental shaft/gear torsional mode shape computed with the FE model which resonates at about 4 kHz. The effects of this mode are included in subsequent forced response calculations.

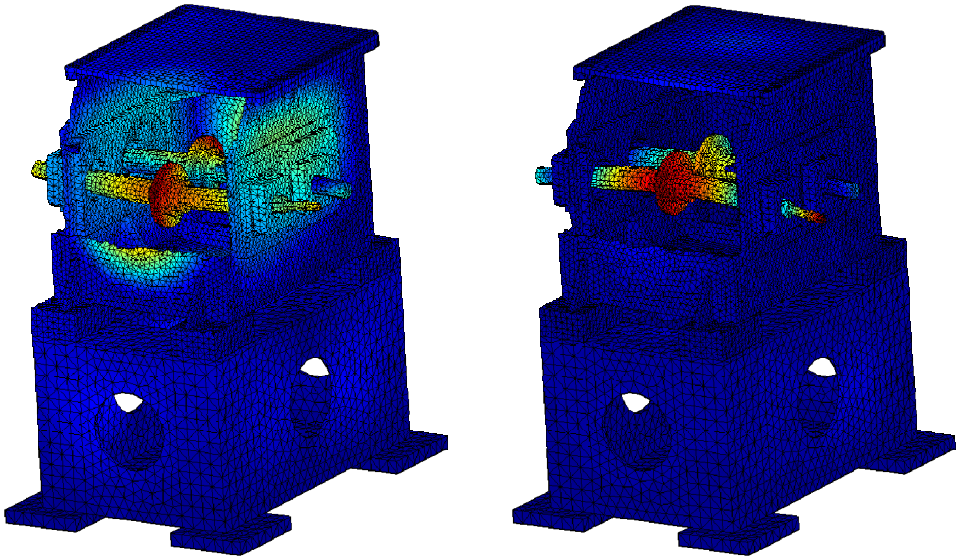

Figure 26. Sample shafting modes. Left - shafting mode strongly coupled with gearbox; right - shafting mode weakly coupled with gearbox.

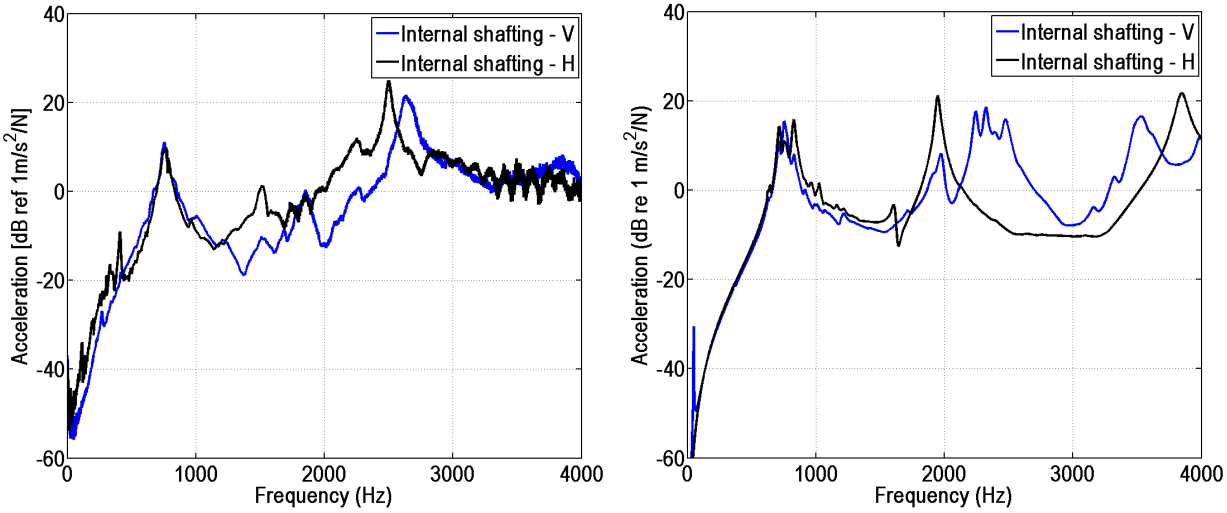

Figure 27. Averaged drive point accelerances over input and output shafts in vertical and horizontal directions, with lid removed from gearbox. Left – measured; Right – simulated

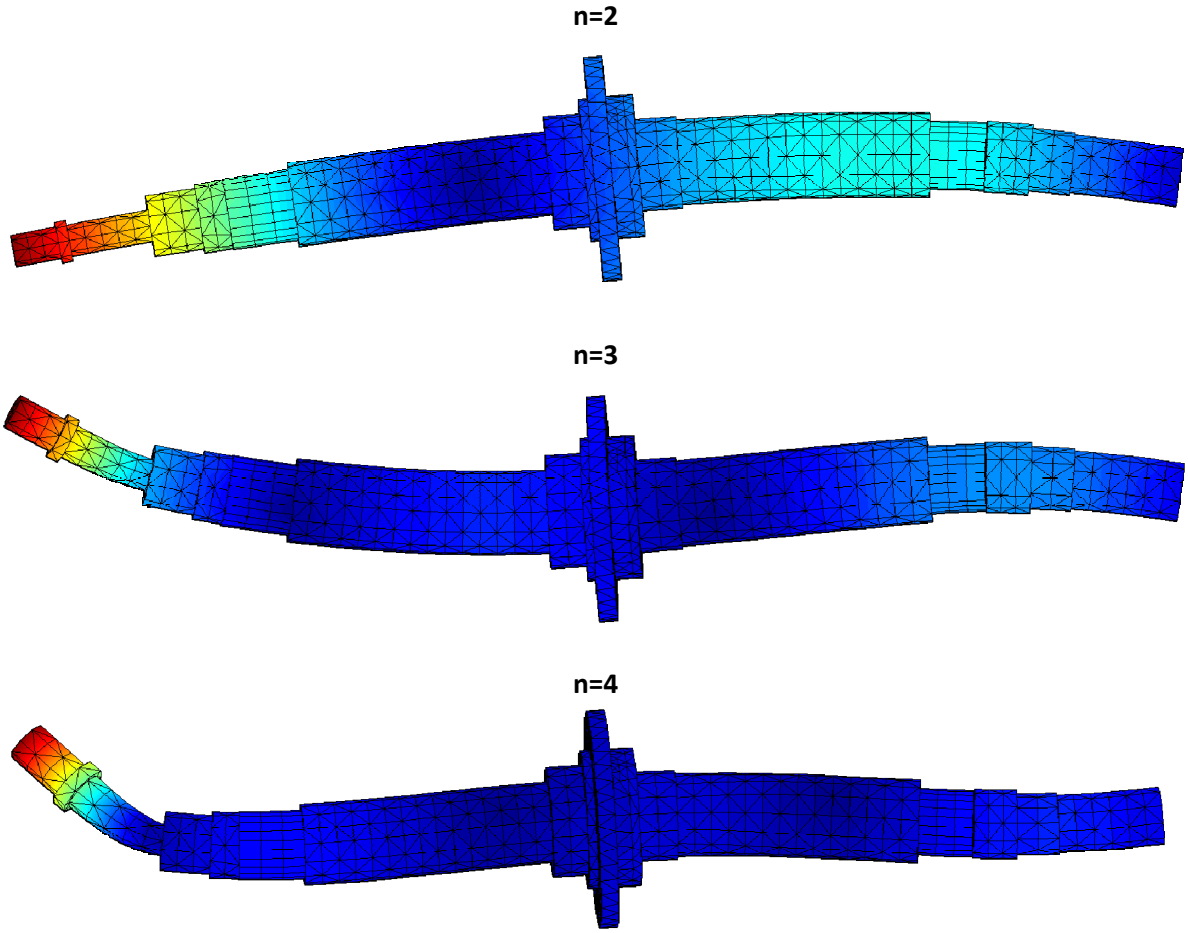

Figure 28. Mode shapes of first three shaft mode types (without bearing or gear mesh stiffnesses).

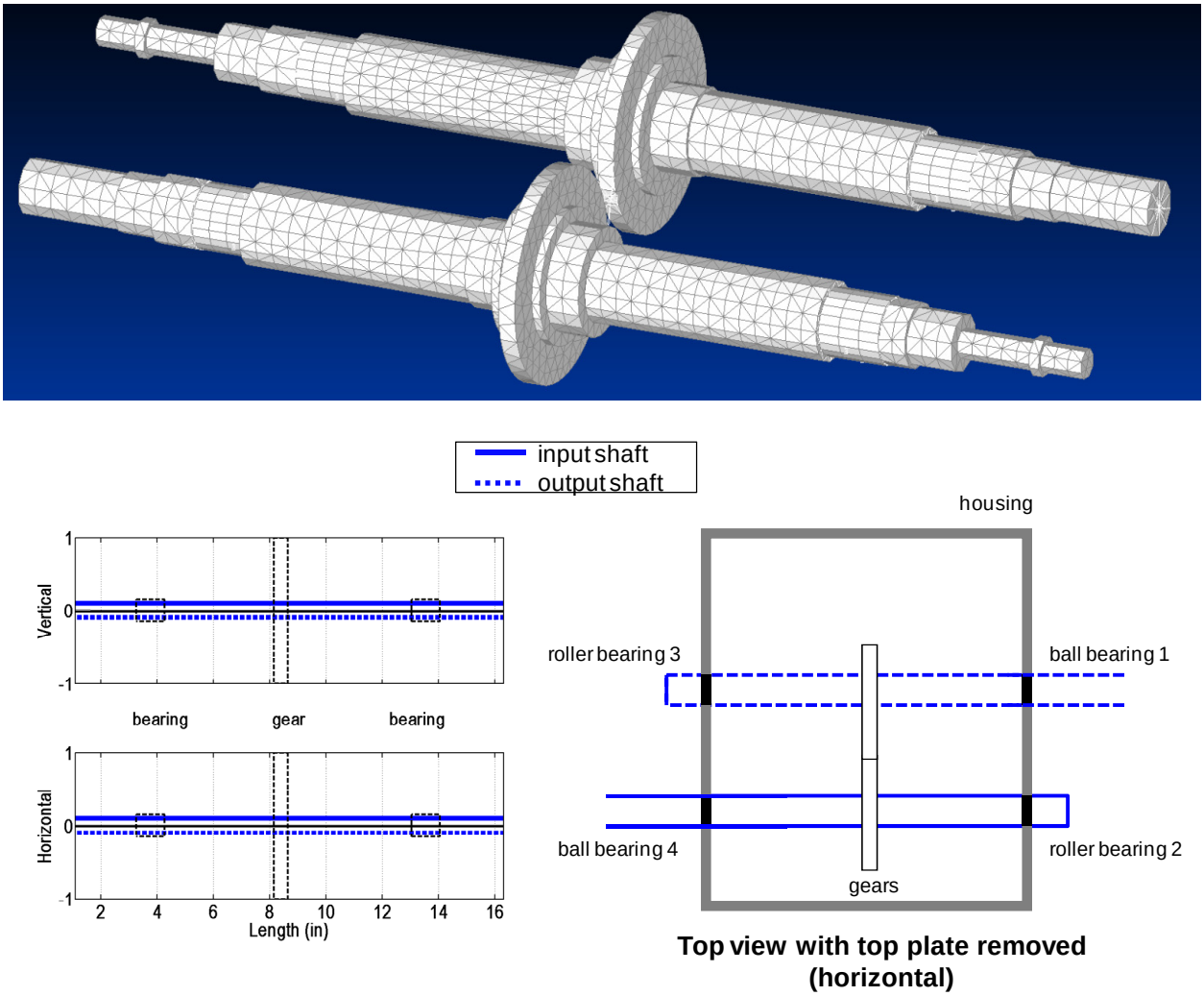

Figure 29. Shafting FE model (top); top view of gearbox with lid removed (lower right); and layout for plotting shaft modes in vertical and horizontal directions (lower left).

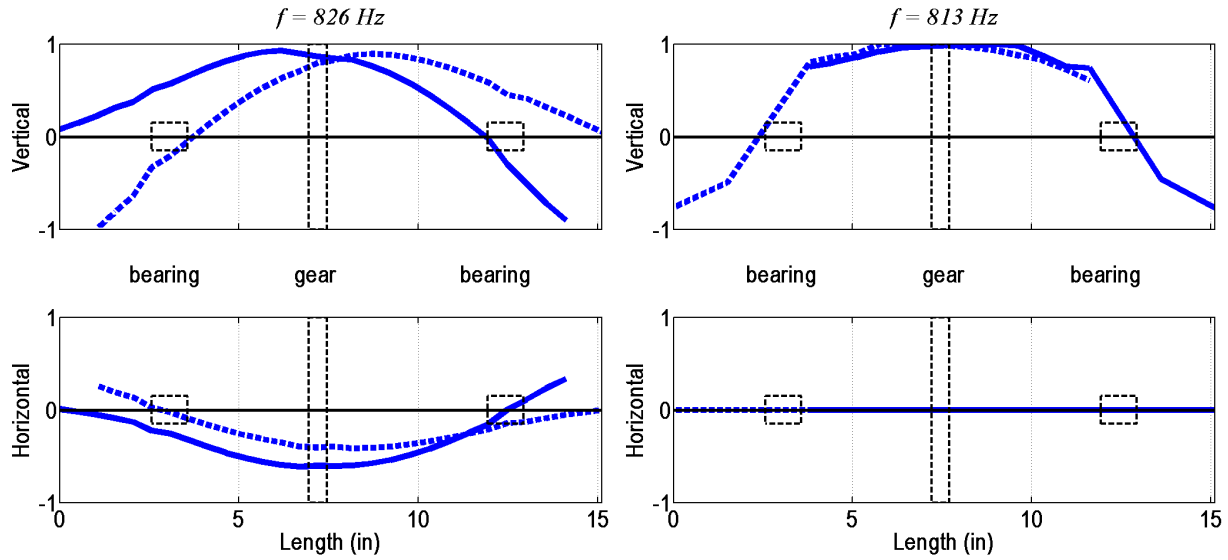

Figure 30. Simulated (left) and measured (right) n=2 shaft mode shapes for gearbox with lid removed.

Mode type	Simulated Frequencies (Hz) lid removed	Measured Frequencies, Hz lid removed	Measured loss factors
n=2	707 – 826	750, 813	0.032, 0.046
n=3	1946-2323	2498	0.015

Table 11. Measured and simulated shaft bending modes for gearbox with lid removed.

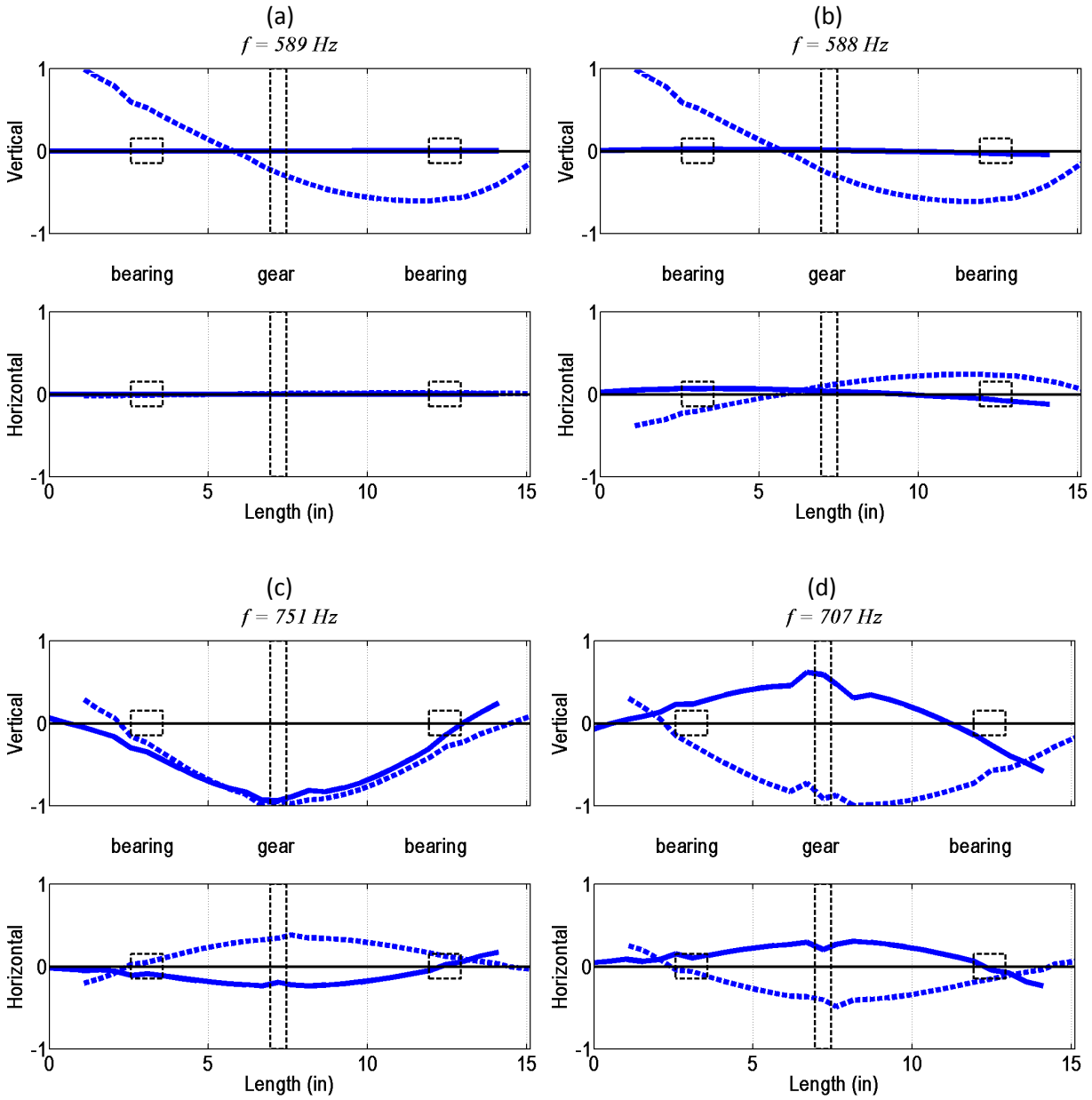

Figure 31. Effects of adding gear meshing, bearing, and housing stiffness to fundamental (n=2) shaft mode for fully assembled gearbox. (a) Uncoupled shafts, output shaft mode in vertical direction. (b) Shafts coupled with gear meshing stiffness. (c) Same as (b), but also connected to flexible rolling element bearings. (d) Same as (c), but also includes housing flexibility.

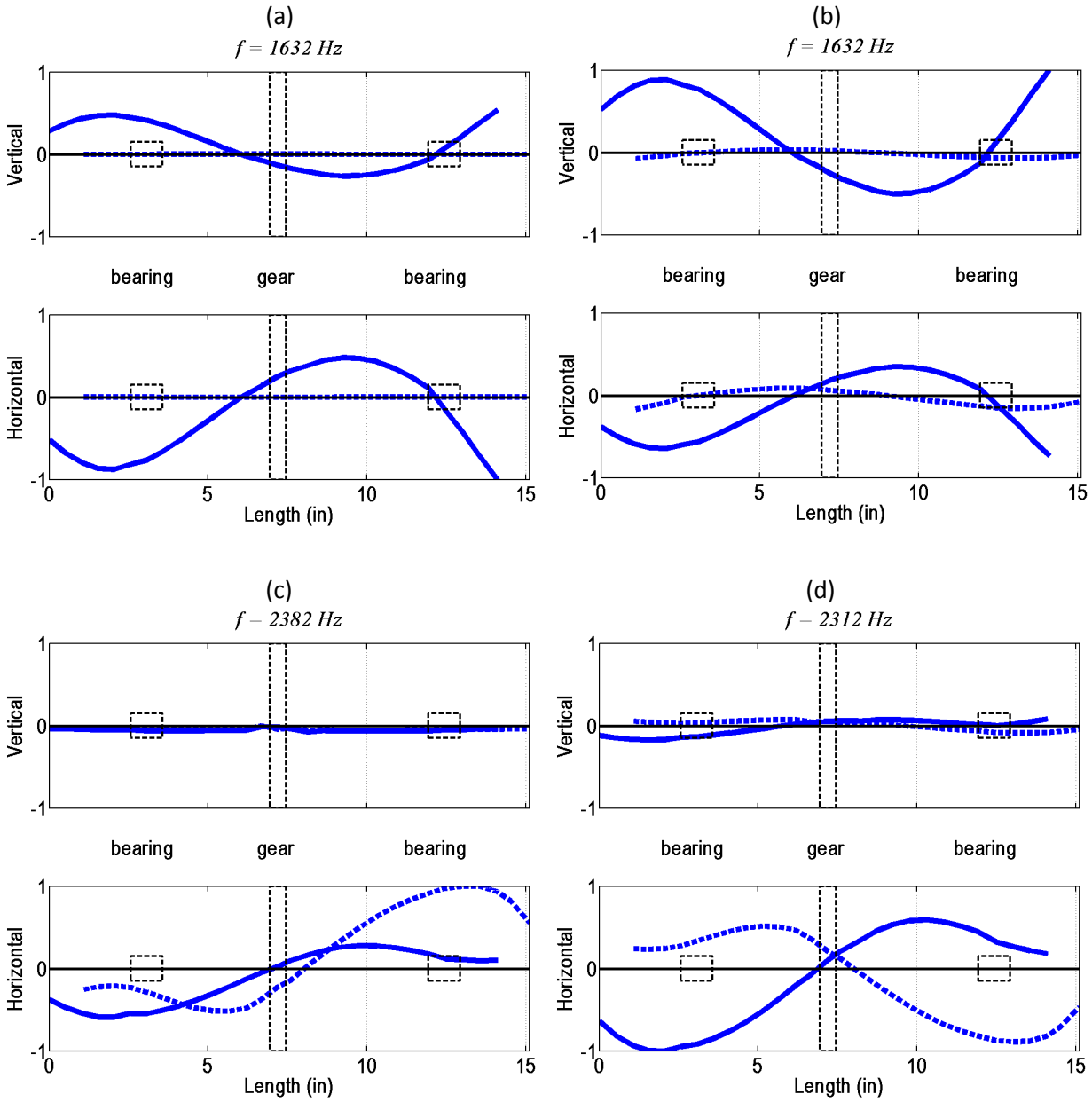

Figure 32. Effects of adding gear meshing, bearing, and housing stiffness to higher order (n=3) shaft mode for fully assembled gearbox. (a) Uncoupled shafts, input shaft mode primarily in horizontal direction. (b) Shafts coupled with gear meshing stiffness. (c) Same as (b), but also connected to flexible rolling element bearings. (d) Same as (c), but also includes housing flexibility.

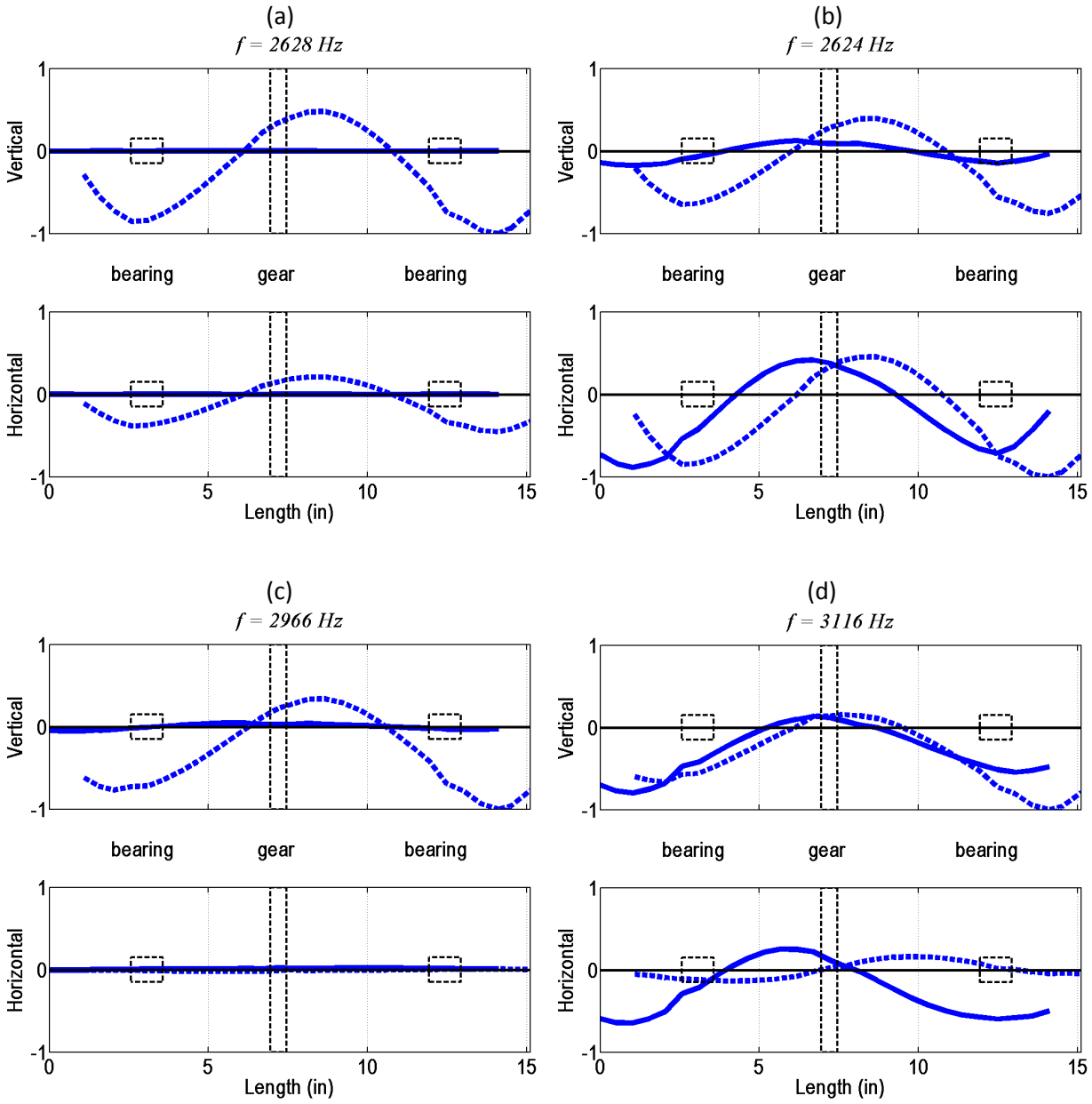

Figure 33. Effects of adding gear meshing, bearing, and housing stiffness to higher order (n=4) shaft mode for fully assembled gearbox. (a) Uncoupled shafts, output shaft mode primarily in vertical direction. (b) Shafts coupled with gear meshing stiffness. (c) Same as (b), but also connected to flexible rolling element bearings. (d) Same as (c), but also includes housing flexibility.

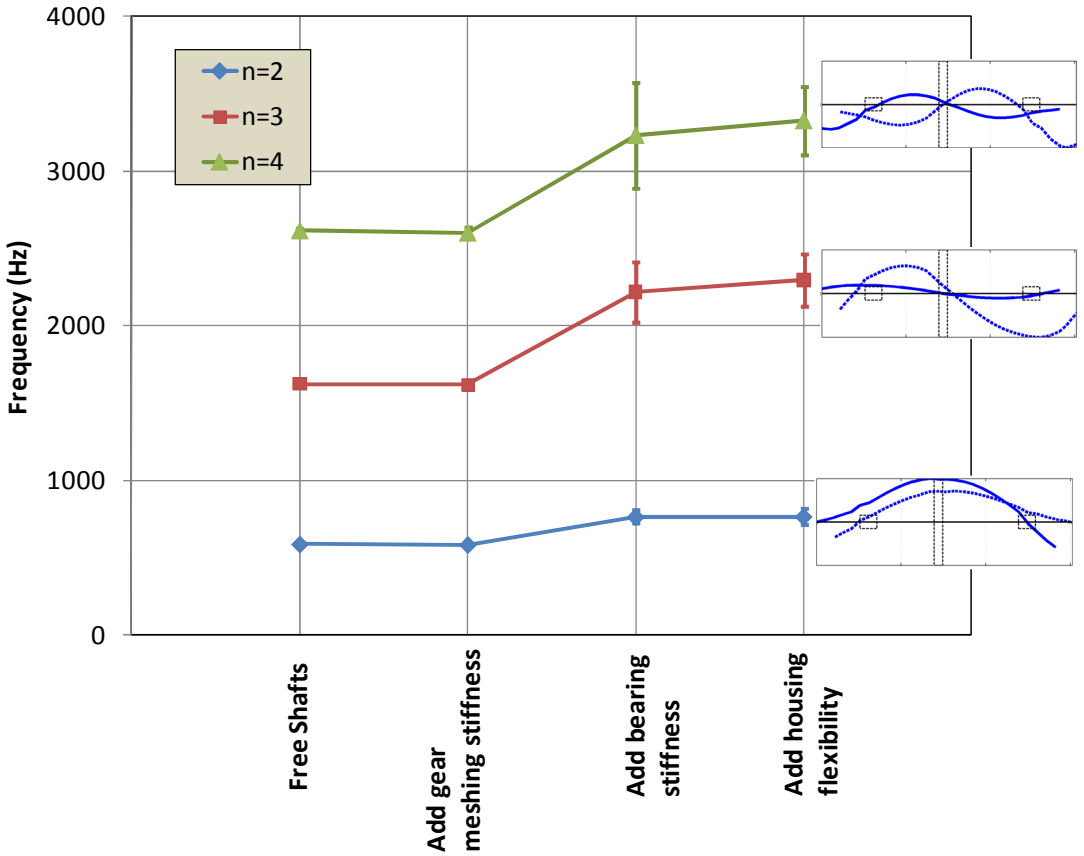

Figure 34. Effects on shaft mode frequencies by sequentially adding gear meshing stiffness, bearing stiffness, and housing flexibility.

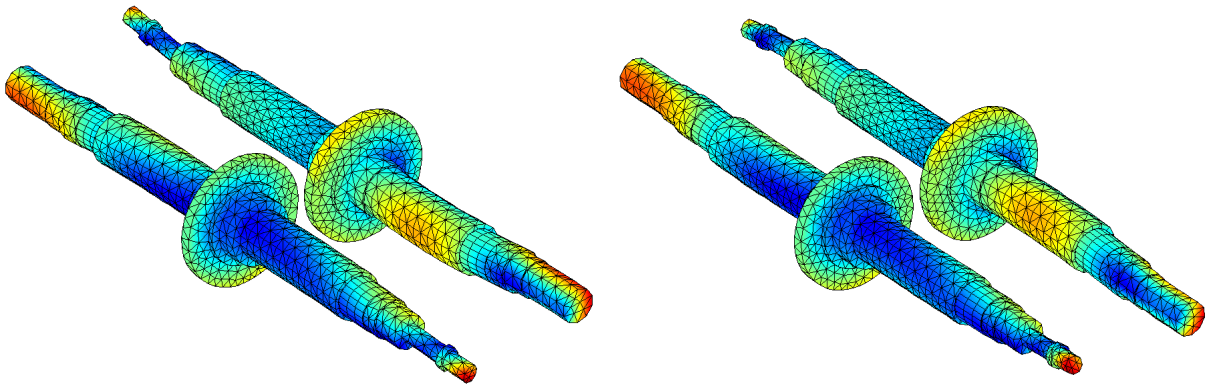

Figure 35. Torsional shafting/gear mode at about 4 kHz in FE model. Images reflect the two peak deflection points, separated by 180 degree phase angle, in an oscillation cycle.

3.4.1.2 Housing Modes

The top panel vibrations were measured with accelerometers and force hammers. Mode shapes, resonance frequencies, and loss factors were extracted from the vibration measurements using ARL/Penn State's modal analysis software. The first six mode shapes of the top panel are shown in Figure 36, along with measured and simulated resonance frequencies, and measured loss factors. The measured and simulated frequencies match within 5% (except for the (4,1) mode frequency, which is underestimated by 7%). The loss factors are generally high – about 0.05 – mostly due to the effects of the O-ring between the top panel and the housing.

An example of a comparison between simulated and measured drive point mobilities is shown in Figure 37. Also shown in the plots is the mobility of an infinite panel with the thickness and material properties of the top plate. The infinite panel mobility, which should be the mean of the finite panel mobility, acts as a check on the data. The mobilities agree very well, establishing confidence in the housing modeling approach.

To obtain a good match of peak modal amplitudes, the measured loss factors were applied to the FE model. The loss factors extracted from the gearbox modal analysis, which includes the sides of the housing and the shafting external to the housing, are shown in Figure 38. The loss factors range from 0.005 to 0.080. The loss factors of the top plate are highest, with the loss factors of the shafting modes also high – ranging from about 0.040 to 0.015. The overall top housing modes have loss factors of about 0.02. Where possible, the measured loss factors of individual modes were assigned to those of the gearbox FE model. For all modes which are unclassifiable (modes where most or all components are in motion), the average loss factor, which is approximately 0.02 for frequencies up to 4 kHz, was applied as a reasonable approximation.

Some of the global housing modes were also extracted from additional gearbox vibration measurements. These modes are more difficult to quantify than the shafting and top panel modes, since several panels are in motion, and strongly coupled to the shafting. Nevertheless, a few well defined modes could be identified and positively matched to those computed with the FE model. Figure 39 compares simulated and measured resonance frequencies for three modes, and also includes measured loss factors for the modes. The frequencies do not match as well as those of the top panel, but the agreement is sufficient to establish confidence in the housing model as a reasonable simulator of gearbox vibro-acoustic behavior.

Mode shape	Simulated frequency	Measured frequency	Loss factor
(1,1)	465 Hz	489 Hz	.061
(2,1)	864 Hz	876 Hz	.061
(1,2)	1215 Hz	1223 Hz	.044
(3,1)	1532 Hz	1555 Hz	.048
(3,2)	2279 Hz	2232 Hz	.053
(4,1)	2400 Hz	2546 Hz	.012

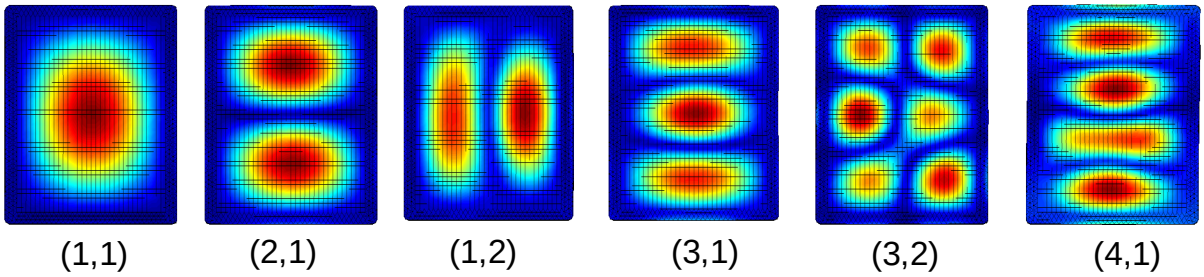

Figure 36. Measured and simulated top panel modes, attached to housing.

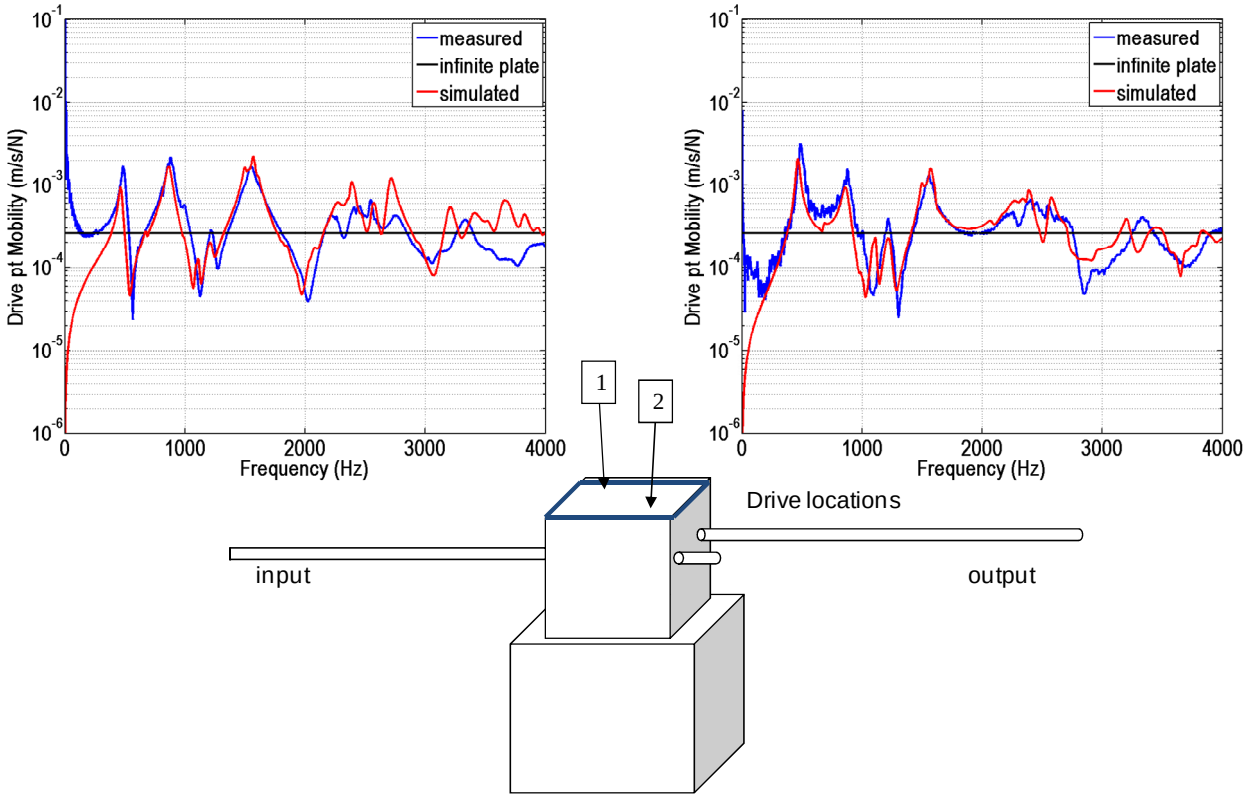

Figure 37. Simulated and measured drive point mobility of top panel, with first three mode shapes.

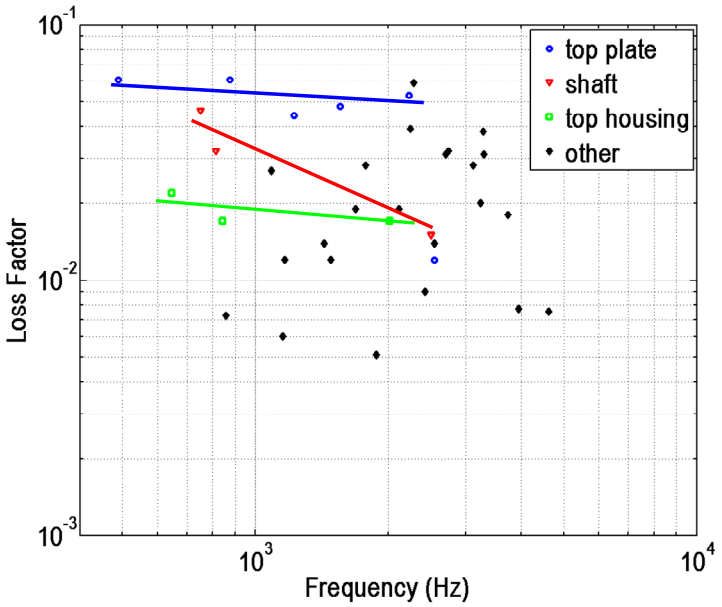

Figure 38. Measured gearbox mode loss factors, along with averaged curve fits.

Mode shape	Simulated frequency	Measured frequency	Loss Factor
A	677 Hz	647 Hz	.022
B	990 Hz	841 Hz	.017
C	1972 Hz	2013 Hz	.017

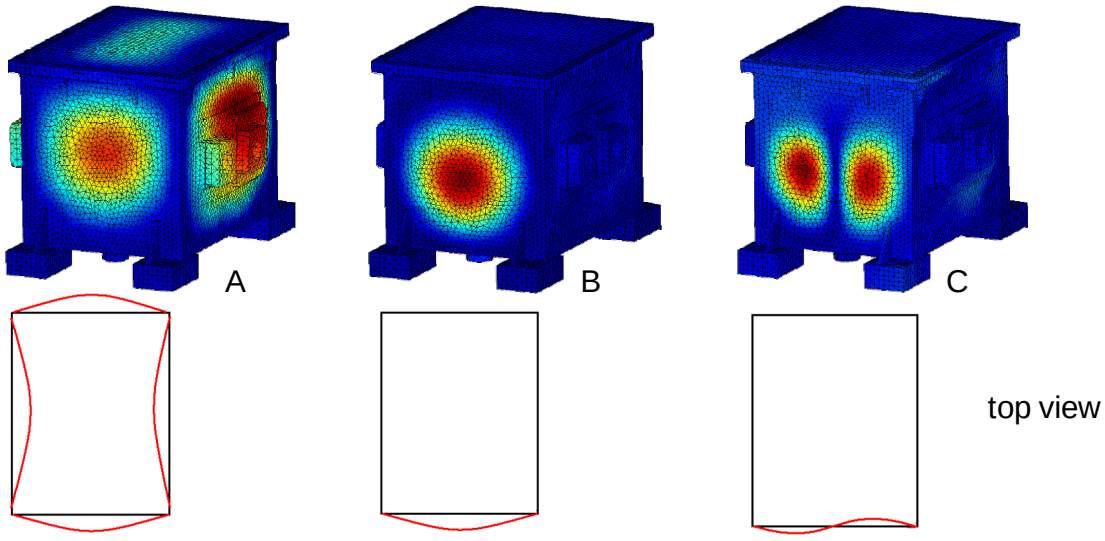

Figure 39. Measured and simulated top housing modes, top panel attached.

3.4.2 Transfer mobilities between gears and bearing locations

Figure 40 shows an example of where vertically and horizontally oriented accelerometers were mounted on the outer surface of the gearbox adjacent to the bearings. The flexible coupling attached to one of the shafts is also visible in the image. Measurements of the transfer accelerances between forces applied to the gear teeth in the LOA and vertical and horizontal vibrations adjacent to the bearings are compared to simulations in Figure 41 for the top panel removed. Note that the measurements were made with soft mounts on the gearbox feet in the physical hardware (the FE model assumes rigid connections, which is consistent with the operational configuration later tested by NASA GRC), which primarily affects low frequency response.

In spite of the differences between the simulated and measured configurations, the transfer functions agree fairly well. Dominant response peaks appear at about 800, 2500, and 3300 Hz, frequencies which correspond to modes of the internal shafting. The comparisons establish that the FE model is an acceptable representative test case to assess the differences between rolling element and journal bearing noise performance.

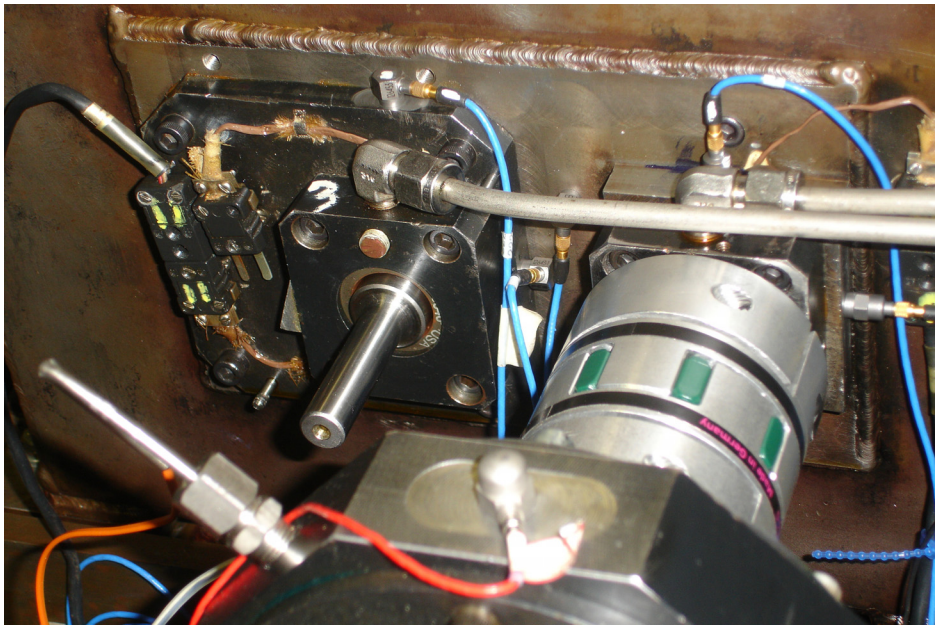

Figure 40. Vertical and horizontal accelerometers mounted on end plates outside gearbox.

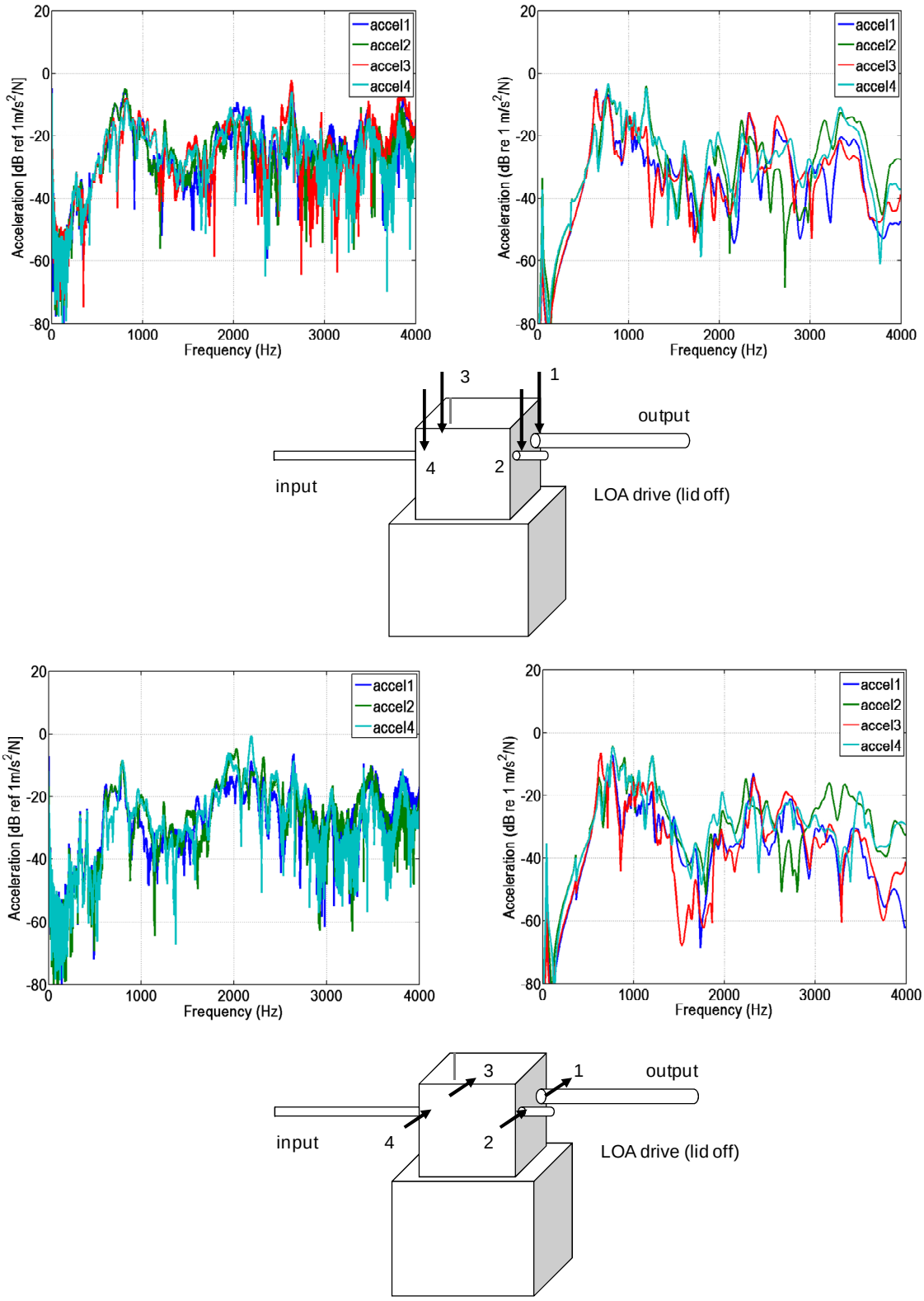

Figure 41. Simulated and measured transfer accelerances between gear tooth loads (in line of action) and bearing accelerometers with top panel removed. Top – vertical (without accelerometer 3, which produced noisy results) and Bottom – horizontal.

3.5 Sound Radiation Modeling

The walls of the gearbox were meshed with boundary elements so that the sound radiated by the wall vibrations could be modeled. Models were constructed for both Coustyx, a fast multipole boundary element modeling software package from ANSOL [42], and ARL/Penn State's POWER software [43]. Both BE analysis approaches should provide similar results. However, since the ANSOL data files are quite large for this application, the POWER software was applied to save storage space and increase turnaround time.

The BE models may be used to compute radiated sound power, as well as radiation efficiency:

$$\sigma_{rad} = \frac{P_{rad}}{\rho_o c_o A \left\langle |v|^2 \right\rangle},$$

where c_o is the speed of sound in air, ρ_o is the density of air, A is the total external surface area of the gearbox, and $\left\langle |v|^2 \right\rangle$ is the surface average of the rms normal wall velocity.

The gearbox housing radiates sound very well near and above its critical frequency, which may be calculated as:

$$f_c = \frac{1}{2\pi} c_o^2 \sqrt{\frac{\rho h}{D}},$$

where D is the flexural rigidity, ρ is the structural mass density, and h is the panel thickness. For the NASA GRC gearbox walls, f_c is about 1900 Hz. Therefore, for frequencies above about 2 kHz, the radiation efficiency of the gearbox walls is nearly unity, and the sound radiation may be computed easily without using BE simulations as:

$$P_{rad_{high}} = \rho_o c_o A \left\langle |v|^2 \right\rangle,$$

where P_{rad} is the radiated sound power (here, computed as the high frequency limit). The mean radiated pressure corresponding to the radiated power at any frequency (above or below coincidence) may be computed using a monopole (or point) source assumption, where:

$$|p|^2 = \frac{P_{rad} \rho_o c_o}{2\pi a^2},$$

where p is the peak pressure on a sphere of radius a, where a is typically taken as 1 yard or 1 meter. To compute sound directivity, or pressure at a specific point, however the BE software is still required.

The sound power radiated by the gearbox with rolling element bearings caused by a unit load applied at the gears in the line of action is shown in Figure 42, along with the high frequency limit of radiated power. Above 1800 Hz (near the estimated critical frequency), the sound power and high frequency limits are nearly identical, implying a radiation efficiency of unity. The radiation efficiency is shown in

Figure 43, and is indeed close to unity for frequencies near and above 1800 Hz, and decreases nearly monotonically with frequency below 1800 Hz. The low-frequency behavior is simulated with curve fits with respect to the ratio of frequency to critical frequency (f/f_c). The traditional quadratic curve fit, which works well for single flat panels, underestimates the actual radiation efficiency. A linear curve fit does not match exactly, but is within 2-3 dB of the calculated values below coincidence. The computed radiation efficiency is similar in character to those measured by Igarashi and Asano [34], who also showed a slow rolloff in radiation efficiency below the critical frequency. Since the BE-computed radiation efficiency may be simply modeled with a curve fit, where

$$\sigma_{rad} = \begin{matrix} f / f_c, & f < f_c \\ 1, & f > f_c \end{matrix},$$

and since changing bearing impedances should not lead to significant changes in the gearbox radiation efficiency, we employ the simplified linear curve fit to calculate radiated sound from the gearbox with journal and wave bearings installed.

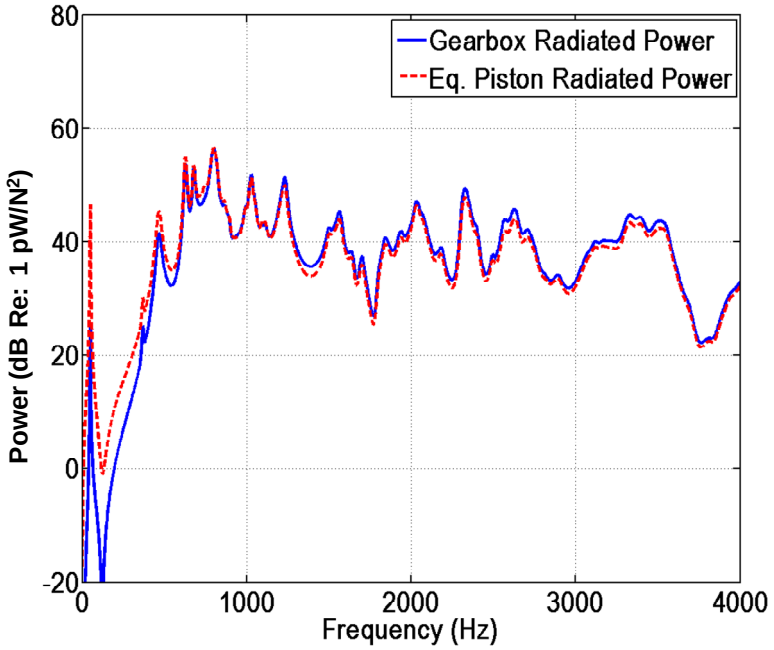

Figure 42. Radiated sound power, and high frequency limit (piston) radiated sound power for gearbox with rolling element bearings, and drive in the LOA of the meshing gears.

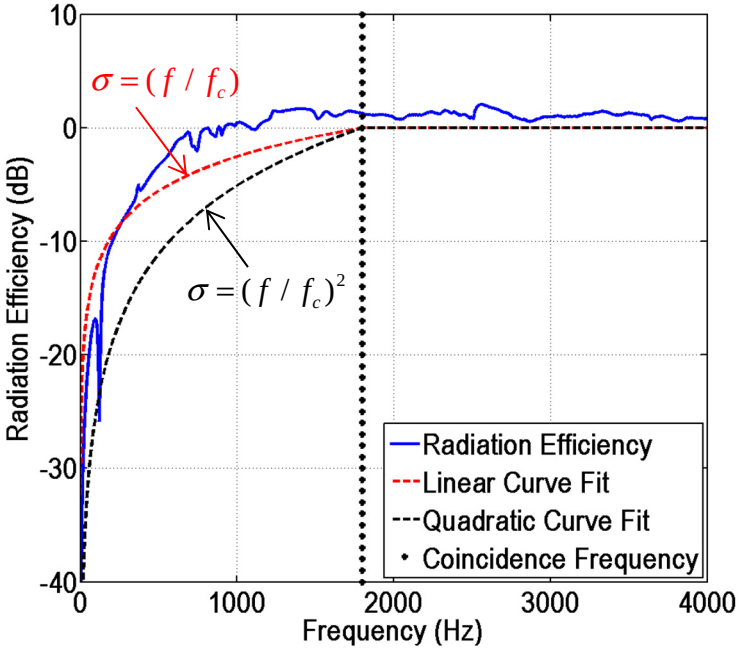

Figure 43. BE-computed and approximate (curve fits) radiation efficiency for gearbox with rolling element bearings, and drive in the LOA of the meshing gears.

4 Simulated and Measured Operating Gearbox Results

The vibrations of operating gearboxes are dominated by tones at the Gear Meshing Frequencies (GMFs), and at sideband tonal frequencies adjacent to the GMFs. The sidebands appear at frequencies equal to the GMFs +-the harmonics of the shaft rotational frequency (SRF). For example, the sidebands adjacent to the 1st GMF would be at GMF-3xSRF, GMF-2xSRF, GMF-1xSRF and GMF+1xSRF, GMF+2xSRF, GMF+3xSRF, etc. The side band amplitudes are caused by amplitude modulation of the fundamental GMF by nonuniformities in gear tooth spacing, caused by geometric imperfections or misalignment and imbalance. Examples of Fast Fourier Transforms (FFTs) of some of the accelerometer and microphone time series acquired by NASA GRC are shown in Figure 44, and show the GMF tones and sidebands.

The GMF peak values are proportional to:

- the gear transmission error forcing harmonic amplitudes, and
- the structural dynamic transfer functions between the meshing gear teeth and the accelerometer and microphone locations at the GMF frequencies.

If the gear transmission error is independent of the bearing stiffnesses, then the forcing harmonics are the same for the REB and journal and wave bearing configurations. In most transmissions, differences in bearing stiffness lead to differences in static shaft deflection, which can alter the alignment of the gears, leading to changes in the GTE. However, ignoring the effects of bearing differences on GTE is reasonable for the NASA GRC gearbox since the gears are near the shaft centers, and the shafts are geometrically similar. Also, the transmission error forces do not depend on frequency. Therefore, the relative differences between the structural dynamic transfer functions may be inferred from the differences between the GMF peak amplitudes measured for the gearbox with rolling element and journal bearings installed (while in theory the side bands might also be usable for this purpose, the side band amplitudes depend also on shaft behavior, which is influenced by the bearings). When measurements are made at several shaft rotational speeds, traces of the GMF peaks may be generated which are indicative of the structural dynamic transfer functions.

4.1 Rolling Element Bearings

Figure 44 shows FFTs of the horizontal and vertical motion of the bearing accelerometers mounted on the output side of the gearbox at 700 in-lb and about 4000 rpm. The GMF peaks are clearly visible. The FFT was taken using a window length equal to the total acquisition record (131,072 samples at 40 kilosamples/sec) so that the peak amplitudes are captured as accurately as possible. Since there is no averaging with this approach, the degree of random noise at frequencies other than at the GMFs and its side bands is high. However, this noise does not affect the tonal amplitudes of interest.

The measured data show some significant variability in GMF amplitude throughout the time records (the reasons for this variability are unknown). Therefore, the peak amplitudes are also computed from the raw time series, along with the amplitude variability. The time series are filtered with narrow pass bands around each GMF, and the amplitude means, maxima and minima are computed. Appendix A summarizes the procedure used to calculate GMF amplitudes and variability.

As the rotational speed increases, the gear meshing frequencies also increase, and the transmission error interacts with a different frequency of the structural-dynamic transfer functions. Figure 45 shows a three dimensional diagram of how the GMF tones (and their side bands) vary with increasing run speed, and trace out scaled structural-dynamic transfer functions (the functions are scaled by the amplitudes of the different harmonics of the transmission error). GMF traces for bearing accelerometer location 4 (input side, near the input shaft) for the gearbox with REBs measured at 700 in-lb of torque are compared in Figure 46. The GMF traces are similar, sometimes overlapping over common frequency ranges. This indicates that the GMF forcing harmonics are also similar. Unfortunately, the GMF traces are quite coarse, with a wide frequency bandwidth. NASA GRC typically runs their rig between shaft rates of 2200 and 5800 rpm, in increments of 400 rpm (sometimes 200 rpm). The coarseness of the traces precludes resolving any sharp peaks in the transfer functions influenced by resonances.

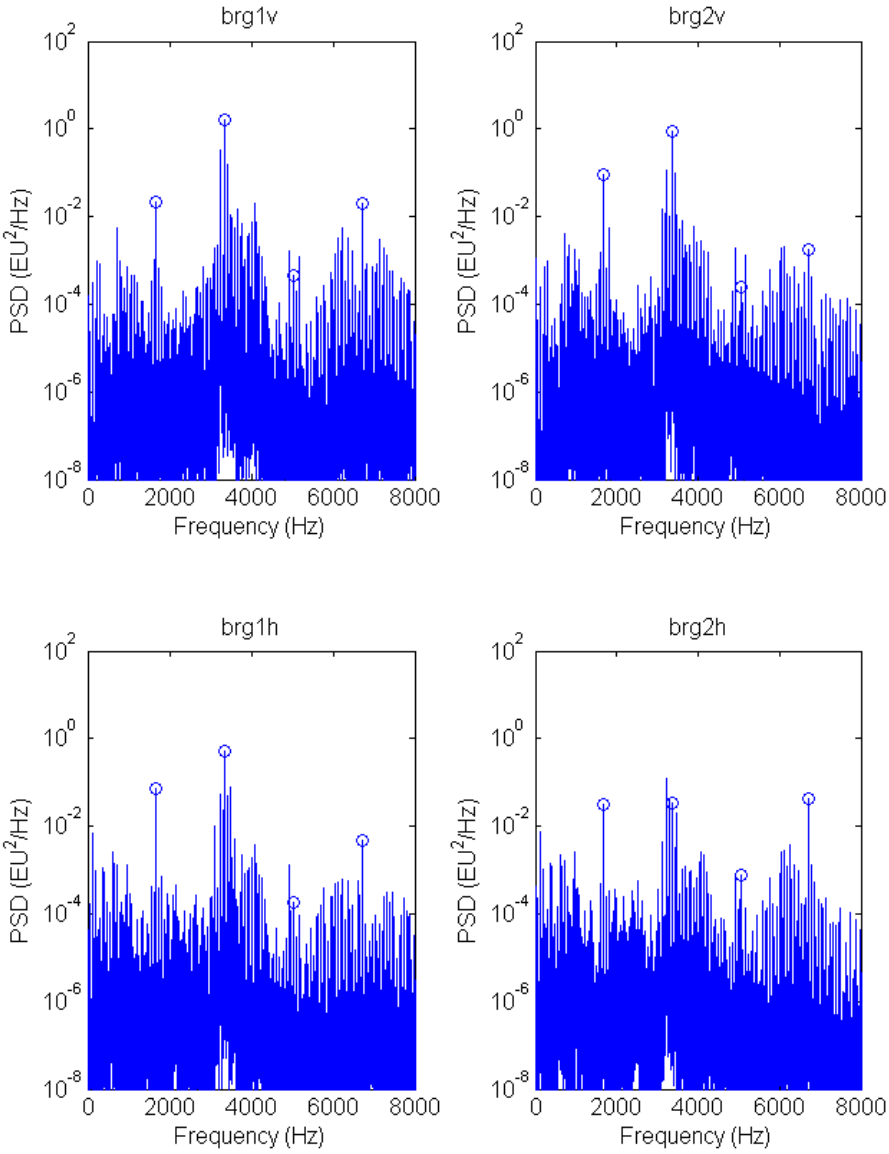

Figure 44. FFTs of acceleration time histories for REBs, 700 in-lb torque, with the first four GMF tones indicated with circles. Engineering Units (EU) are in g's.

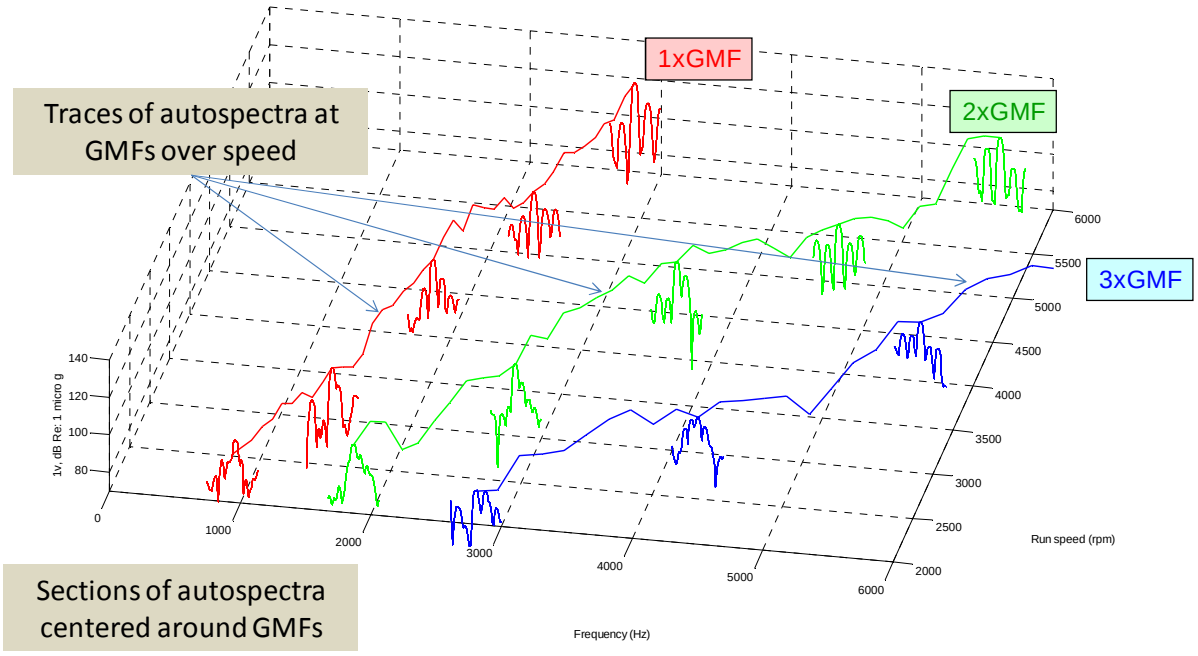

Figure 45. Example of GMF traces over run speed.

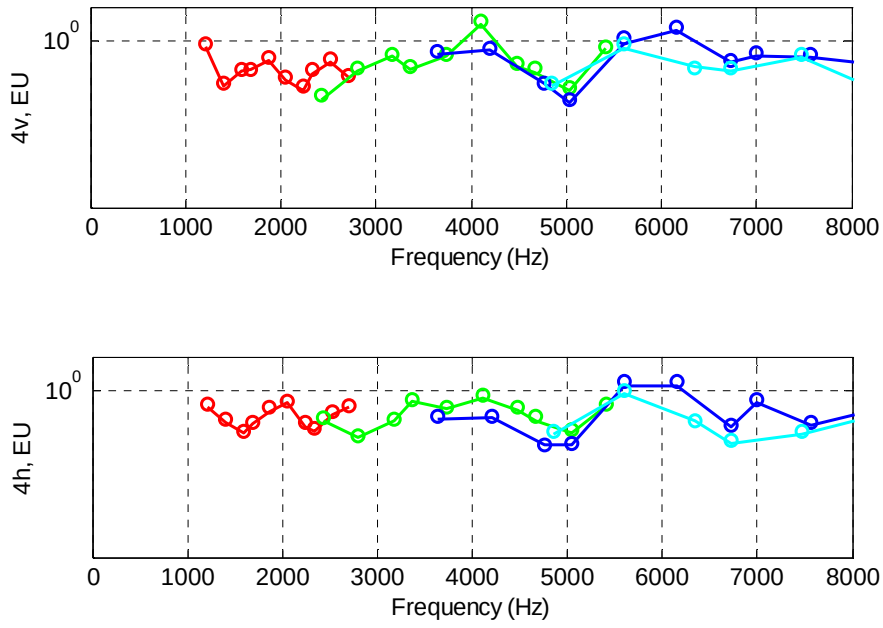

Figure 46. GMF traces for REBs, 700 in-lb torque, location 4. Levels are in g's. Red – 1xGMF, Green – 2xGMF, Blue – 3xGMF, Cyan – 4xGMF.

4.2 Rolling Element vs. Journal (Wave) Bearings

4.2.1 Measurements

NASA GRC measurements of the gearbox vibrations and radiated sound were made at several operational speeds at 700 in-lb of torque. Traces of the 1xGMF and 2xGMF peak amplitudes, along with the amplitude variability over the measurement period are shown for the vertical and horizontal accelerometer averages, and for averages over two microphone locations above the gearbox in Figure 47 for 1xGMF and Figure 48 for 2xGMF. Figure 40 and Figure 41 show the bearing accelerometer locations. The two microphones are located about 79 cm directly above the gearbox, and separated horizontally by about 18 cm.

In the figures, both the GMF frequencies and their corresponding operational speeds (rpm) are shown. Also, the variability of the measured levels are included in the figures. The figures show that the trends in radiated sound are similar to those in the averaged vertical vibration. The horizontal vibration also correlates fairly well with the radiated pressure at some operational speeds, but deviates at others. For 1xGMF, there is no clear benefit to replacing rolling element bearings with journal bearings, as the journal bearings lead to higher noise levels at some speeds, and lower noise levels at others. For 2xGMF, however, the gearbox is clearly quieter at nearly all run speeds when equipped with journal bearings.

4.2.2 Simulations Compared to Measurements

The gearbox model was exercised using CHAMP and the CMS approach, with unit loads applied to the gear teeth in the line of action (LOA) to gearbox models with standard rolling element bearings, journal bearings, and wave bearings. For this exercise, however, no measurements were made by NASA GRC of wave bearing performance. NASA GRC had hoped to measure the effects of wave profiles, but budget and schedule constraints precluded those tests. The response transfer functions are converted to those relative to unit gear transmission error (in μm) using the gear meshing stiffness of 108 N/μm.

To enhance the convergence of the CMS, mean bearing stiffnesses were applied to each bearing location in the base FE model, as discussed in Section 3.2. With this approach, the component modes more closely resemble those in the actual gearbox, and fewer modes are required to obtain converged solutions. In CHAMP, the differences between the actual bearing stiffnesses and the mean ones are applied (this can include negative stiffnesses, and non-symmetric stiffness terms). Also, the damping coefficients for the journal and wave bearings are applied in CHAMP. Since the journal and wave bearing stiffnesses and damping vary with rpm (see Figure 23 and Figure 24), the CHAMP analyses are run separately for several operational speeds, and pieced together to form semi-continuous vibration and radiated sound response transfer functions. The CMS approach saves significant computational time here, since it is straightforward to adjust the bearing properties for each sub-analysis.

Figure 49 compares simulations and measurements of the vertical vibrations at the roller bearing on the input side of the gearbox at 1xGMF. The simulations are plotted with a frequency resolution of 1 Hz, whereas the measurements were limited to roughly 200 Hz resolution. The measurements are of actual operational vibration levels, whereas the simulations are transfer functions of vibration relative to a 1

μm gear transmission error. As discussed previously, Penn State did not compute the actual transmission errors, and other efforts, such as those at Ohio State, were not yet complete at the time of this analysis. However, the transmission error harmonics computed using the commercial software Romax are approximately 0.2 μm at 700 in-lb of torque. To estimate the simulated operational vibration levels, the transfer function curves should be multiplied by the square of the transmission error, or when in dB, 20log10(0.2), or -14 dB is added to the curves. This reduction produces levels similar to those measured, establishing further confidence that the models are representative of actual gearboxes.

Also shown in the figure are the differences between the rolling element and journal bearing responses for the measurements and simulations. These differences do not depend on the amplitudes of the gear mesh transmission error, and may be compared directly. In the example, the trends compare well, showing that there is no clear benefit to replacing rolling element bearings with journal bearings for 1xGMF noise. Similar plots are shown for horizontal vibrations at the input shaft bearing and the radiated sound pressure above the gearbox at 1xGMF in Figure 50 and Figure 51. Once again, the simulations and measurements show similar trends. The figures also show that there is little significant difference between the journal and wave bearing vibration and radiated sound levels.

To assess the effects of replacing rolling element bearings with journal bearings on overall gearbox vibration and noise, the differences between averaged vertical and horizontal vibrations are compared to radiated sound measurements and simulations for 1xGMF in Figure 52 and 2xGMF in Figure 53. Once again, there is no clear benefit to replacing rolling element bearings with journal bearings for the 1xGMF tones, but a clear benefit at the 2xGMF tones (5-10 dB reductions). The measured benefits, however, are subject to wide deviations over nearly all run speeds. Both the simulations and measurements (even with the observed variability) show the same trends, establishing further confidence in the validity of the modeling approach.

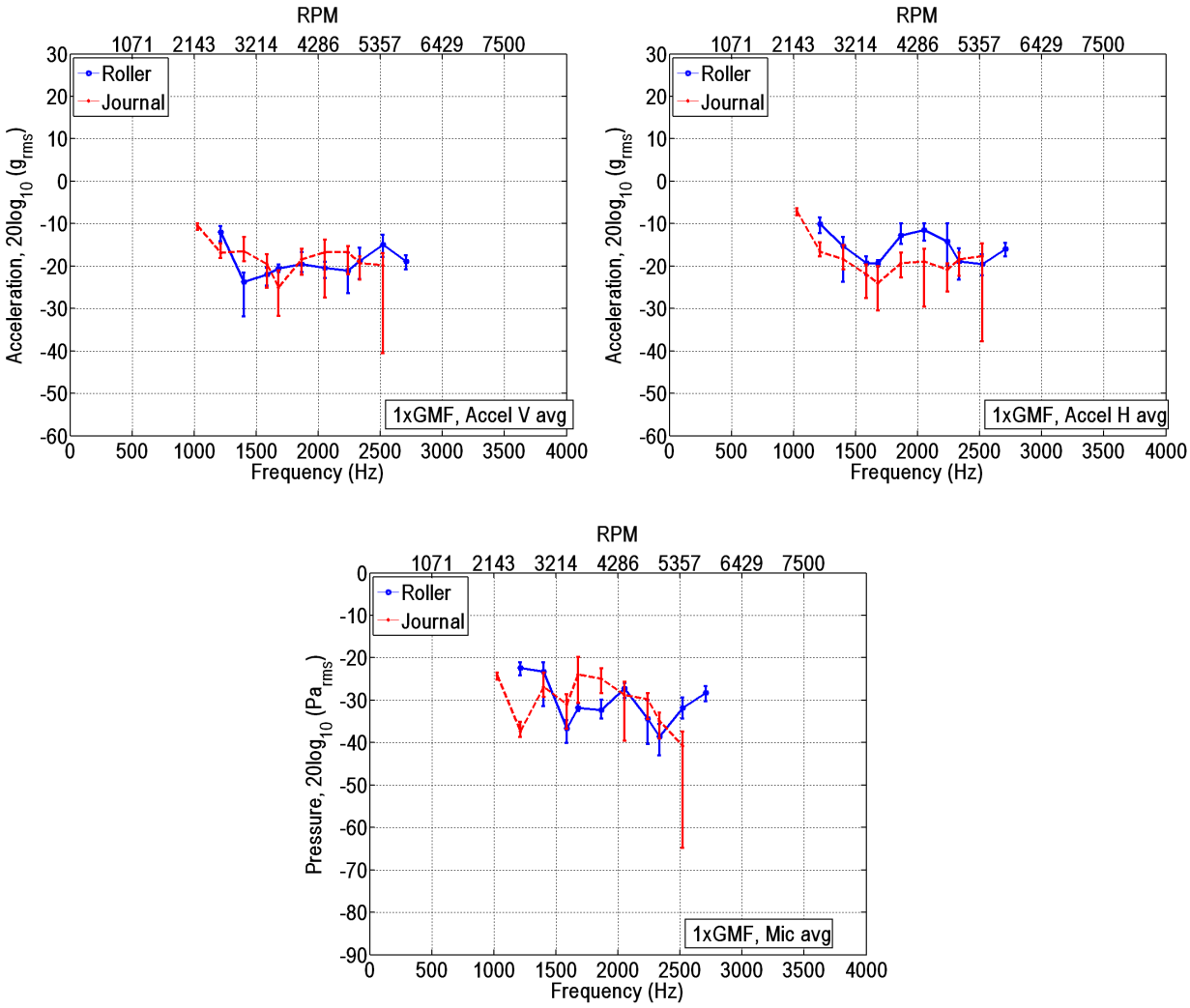

Figure 47. Measured averaged vertical accelerations (upper left), horizontal accelerations (upper right) and pressures (bottom) at 1xGMF for several operational speeds (rpm).

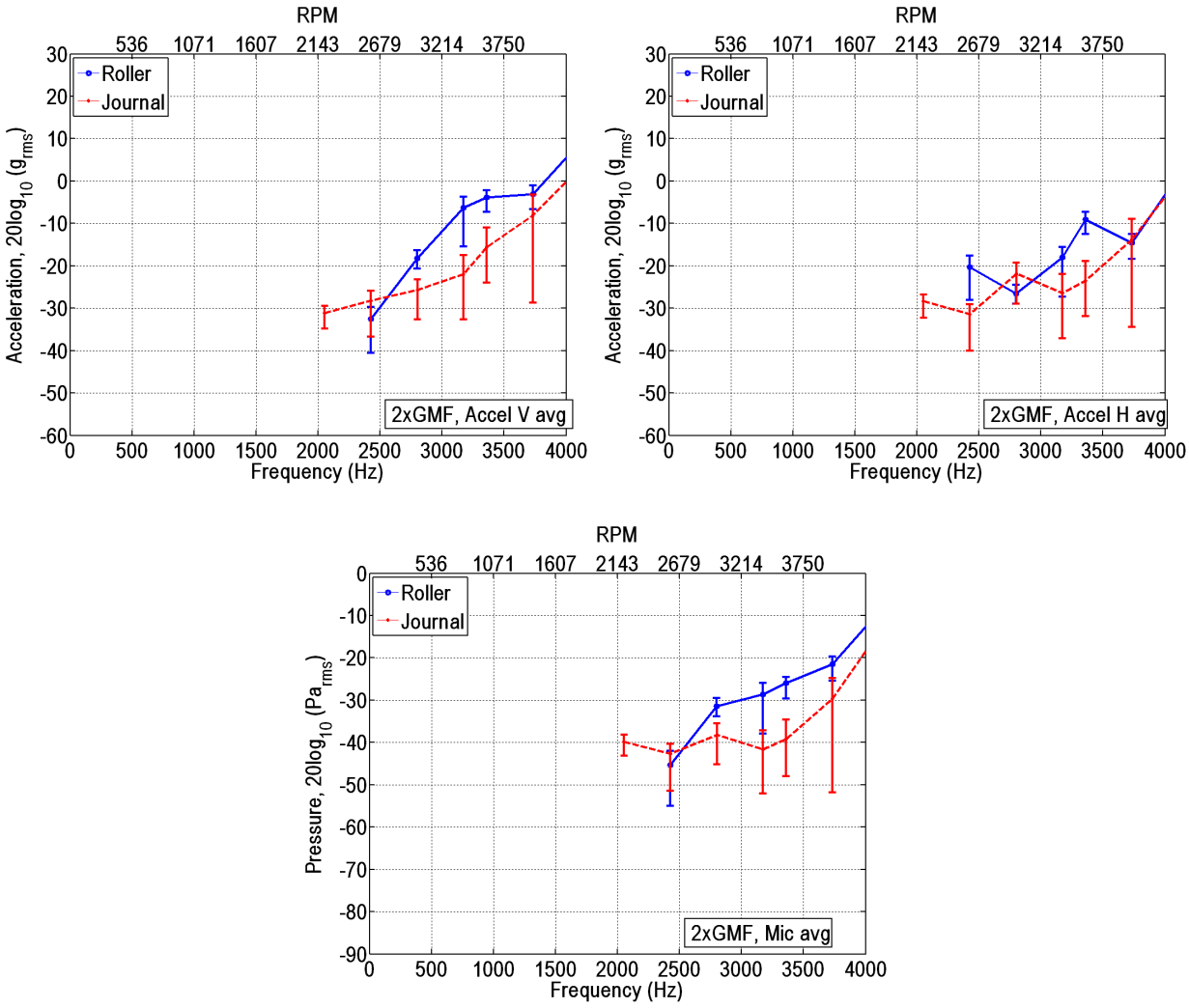

Figure 48. Measured averaged vertical accelerations (upper left), horizontal accelerations (upper right) and pressures (bottom) at 2xGMF for several operational speeds (rpm).

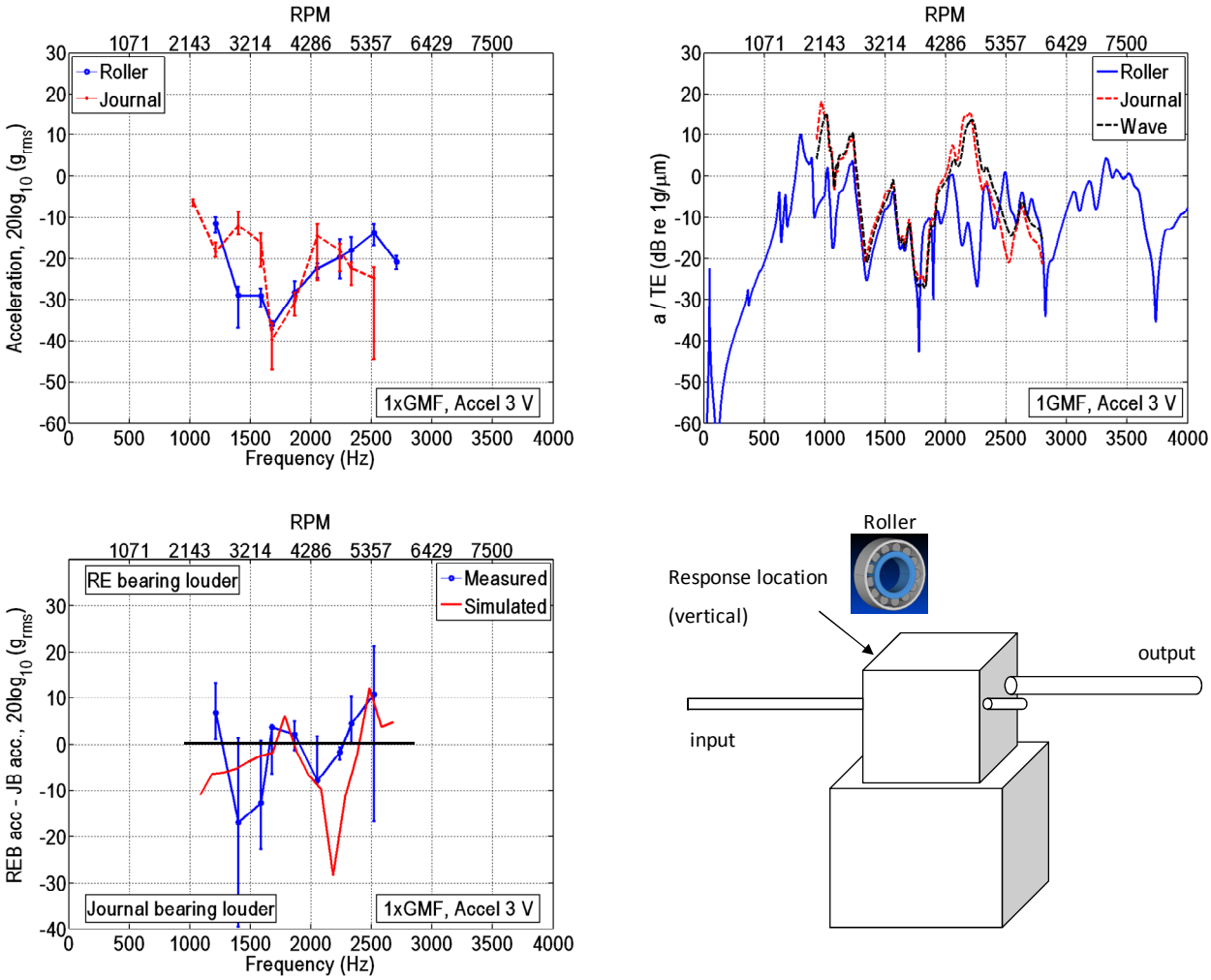

Figure 49. Vertical vibration at rolling element bearing on gearbox input side at 1xGMF. Upper left – measurements at NASA GRC; Upper right – CHAMP simulations; Lower left – differences between gearbox vibrations with rolling element and journal bearings.

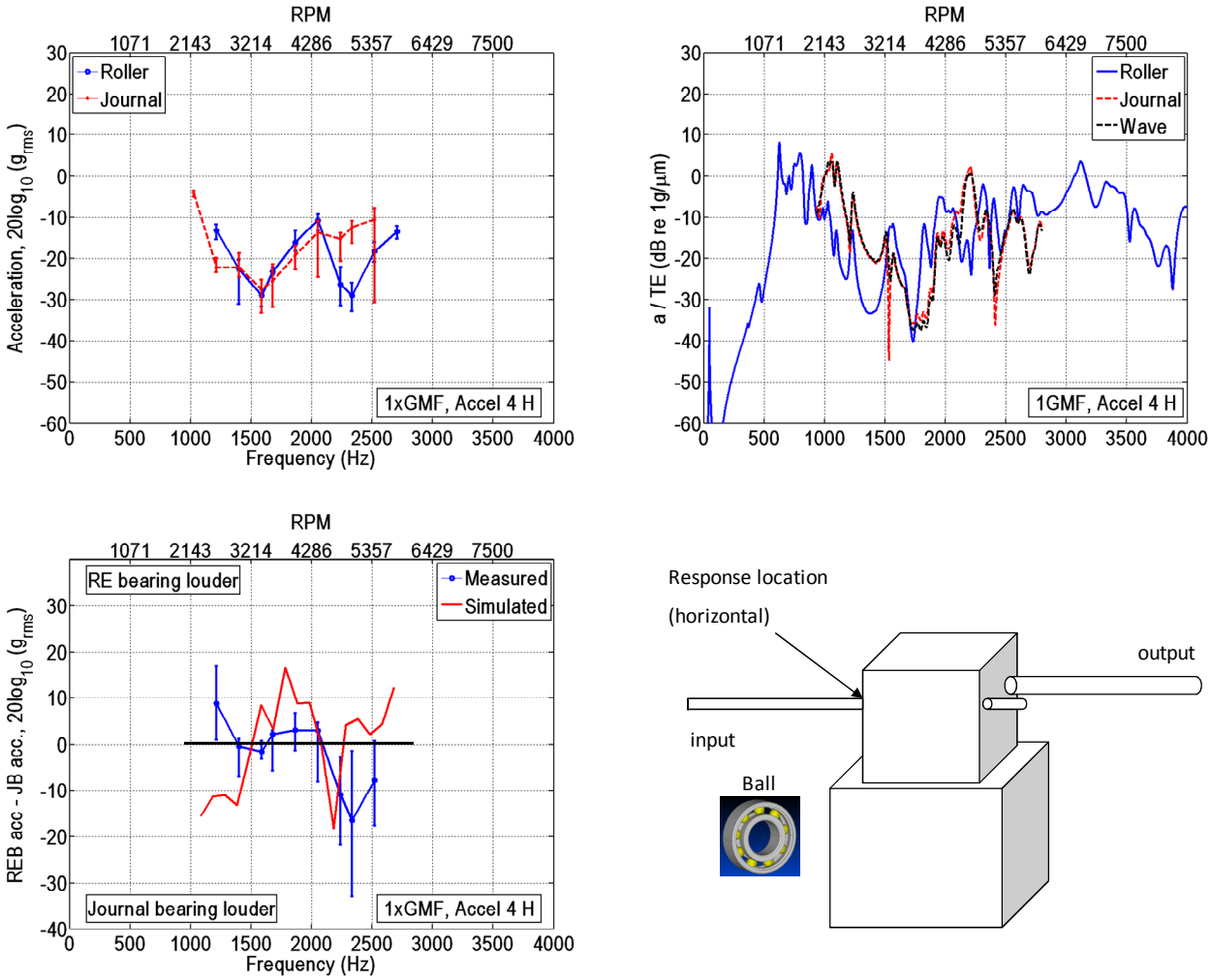

Figure 50. Horizontal vibration at rolling element bearing on gearbox input side at 1xGMF. Upper left – measurements at NASA GRC; Upper right – CHAMP simulations; Lower left – differences between gearbox vibrations with rolling element and journal bearings.

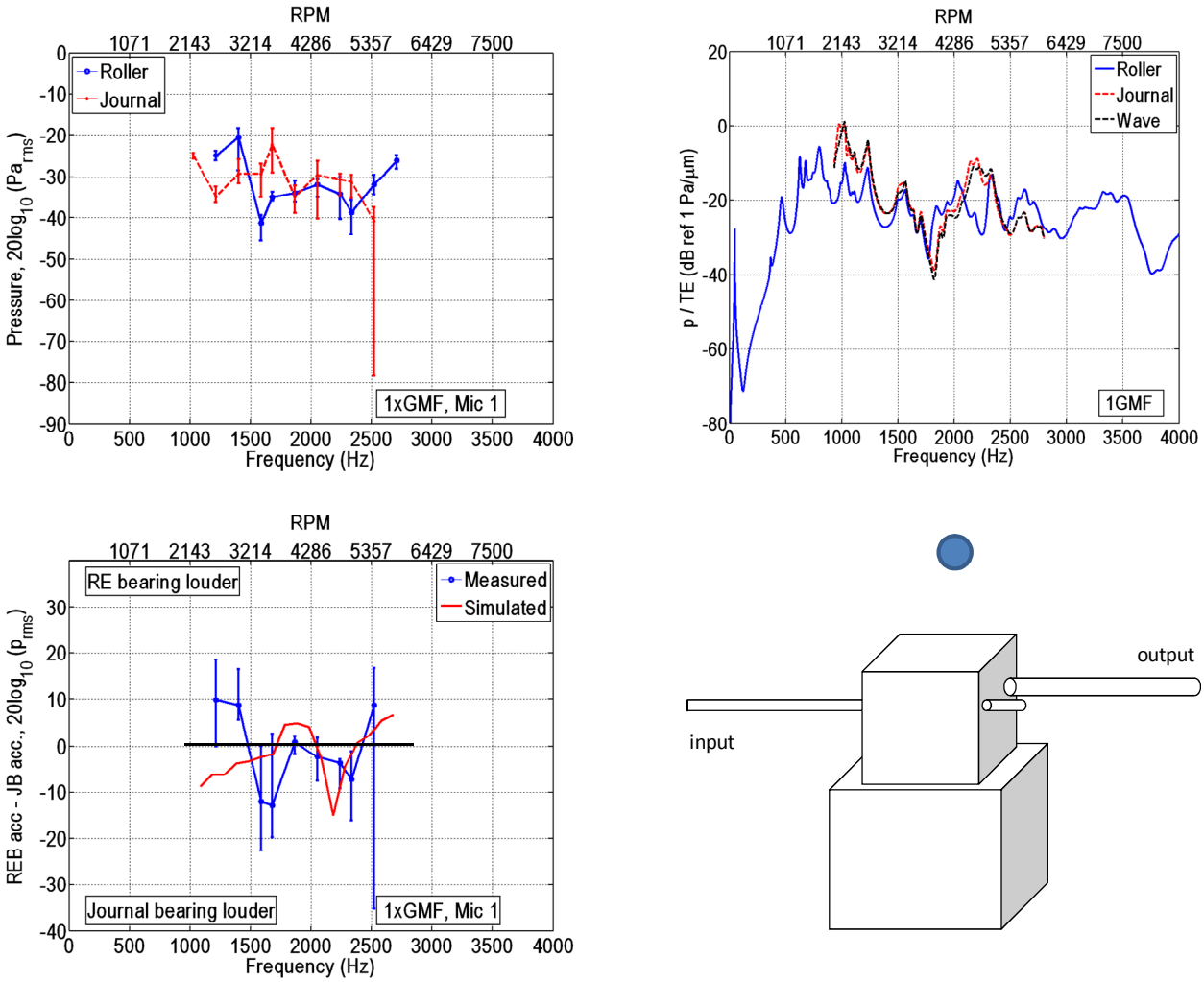

Figure 51. Radiated sound pressure above gearbox at 1xGMF. Upper left – measurements at NASA GRC; Upper right – CHAMP simulations; Lower left – differences between gearbox radiated sound pressure with rolling element and journal bearings.

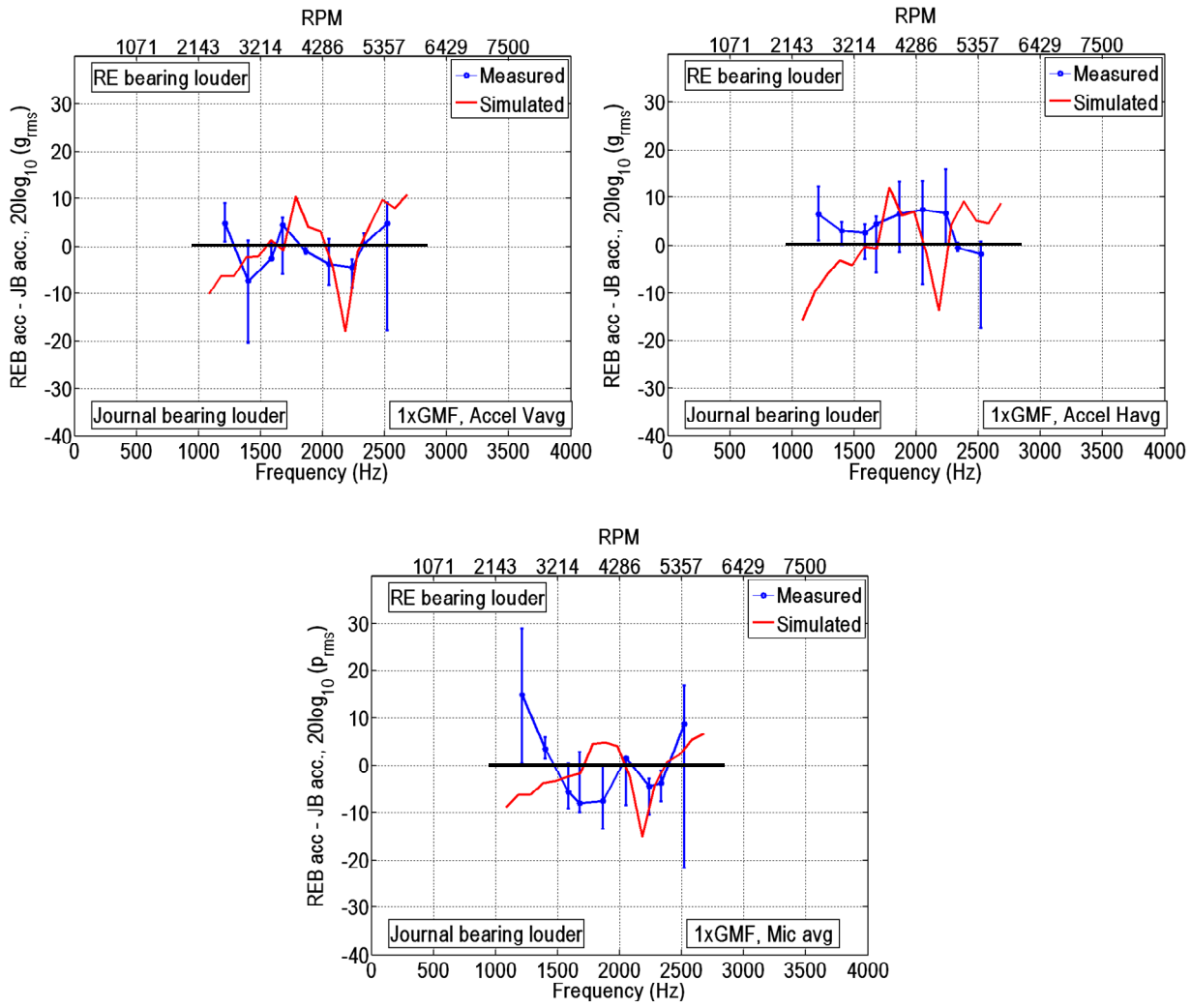

Figure 52. Differences between vibrations and noise from gearbox with rolling element and journal bearings for measured and simulated averaged vertical accelerations (upper left), horizontal accelerations (upper right) and pressures (bottom) at 1xGMF for several operational speeds (rpm).

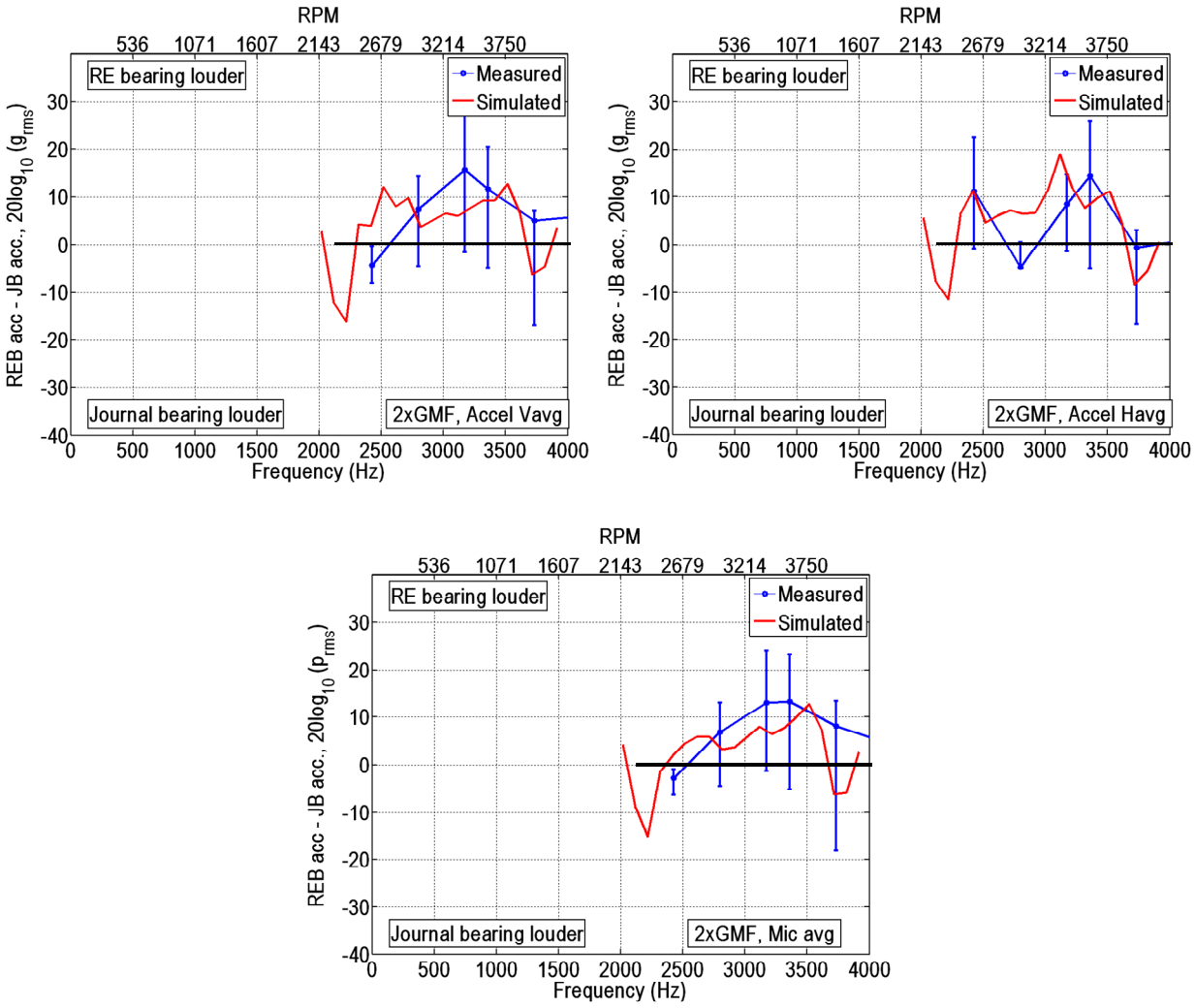

Figure 53. Differences between vibrations and noise from gearbox with rolling element and journal bearings for measured and simulated averaged vertical accelerations (upper left), horizontal accelerations (upper right) and pressures (bottom) at 2xGMF for several operational speeds (rpm).

5 Conclusions and Future Work

A computational approach for simulating the effects of rolling element and journal bearings on the vibration and sound transmission through gearboxes has been demonstrated. The approach, using ARL/Penn State's CHAMP methodology, uses Component Mode Synthesis of housing and shafting modes to allow for rapid adjustment of bearing impedances in gearbox models. The modes are computed using standard Finite Element software and coupled via the bearing impedances. Radiated sound is computed using acoustic boundary element modeling.

The approach has been demonstrated on NASA GRC's test gearbox with three different bearing configurations: in the first condition, traditional rolling element (ball and roller) bearings were installed, and in the second and third conditions, the traditional bearings were replaced with journal and wave bearings. Wave bearings are a form of journal bearing developed under NASA sponsorship where a multi-lobed wave form is imposed on the bearing surface. The waveform eliminates the possibility of whirling instability modes from occurring during operation, and increases the load capacity of the bearing.

A methodology for computing the stiffnesses and damping in journal and wave bearings was presented, and demonstrated for the journal and wave bearings used in the NASA GRC test gearbox. The journal bearings and wave bearings have stiffnesses comparable to those of roller bearings. The stiffnesses, however, depend on rotational speed, complicating their insertion into numerical vibration and noise models. Also, both journal and wave bearings have damping levels more than three orders of magnitude higher than that of rolling element bearings.

The FE model of the gearbox, along with the rolling element bearing coupling impedances, was analyzed to compute dynamic transfer functions between forces applied to the meshing gears and accelerations on the gearbox housing, including several locations near the bearings. The transfer functions were compared to measurements made on a static (non-operational) gearbox driven with an instrumented force hammer, and showed reasonable agreement, with discrepancies due to uncertainties in shaft and gearbox mounting conditions.

Measurements of the Gear Mesh Frequency (GMF) tones were made by NASA GRC at several operational speeds for the rolling element and journal bearing gearbox configurations. Traces of the dynamic response of the gearbox to the GMF tones were extracted from the measurements. The frequency traces show that the vibration and radiated sound levels change when the bearings are changed, but do not indicate clearly which bearing type leads to the lowest noise for 1xGMF tones. This lack of clarity is due in part to the limited frequency (and run speed) resolution in the NASA tests, where the run speed was varied in increments of 200 or 400 rpm. For the 2xGMF tones, however, there is a clear 5-10 dB benefit associated with the journal bearings. The numerical model, which was exercised over a narrow frequency resolution, also indicates that the journal bearings reduce vibration and noise for the 2xGMF tones, but shows no clear benefit to using journal bearings to reduce 1xGMF tones. Finally, the numerical model shows that the gearbox vibrations and radiated sound are similar for journal and wave bearing configurations.

6 References

1. Oswald, F.B., Zakrajsek, J.J, Townsend, D.P., Atherton, W., and Lin, H.H., 1992, "Effect of operating conditions on gearbox noise," *NASA Technical Memorandum 105331*.

2. Dimofte, F., 1995, "Wave journal bearing with compressible lubricant – Part 1: the wave bearing concept and a comparison to the plain circular bearing," *Tribology Transactions*, 38 (1), 153-160.

3. Dimofte, F., 1995, "Wave journal bearing with compressible lubricant – Part II: a comparison of the wave bearing with a wave-groove bearing and a lobe bearing," *Tribology Transactions*, 38 (2), 364-372.

4. Sellgren, U., and Akerblom, M., 2005, "A model-based study of gearbox-induced noise," *NAFEMS Seminar: Component and System Analysis using Numerical Simulation Techniques*, 23-24 November 2005, Gothenburg, Sweden.

5. Tanaka, E., Houjoh, H., Mutoh, D., Motoshiromizu, H., Ohno, K., and Tanaka, N., 2003, "Vibration and sound radiation analysis for designing a low-noise gearbox with a multi-stage helical gear system," *JSME International Journal, Series C*, 46 (3), 1178-1185.

6. Soeiro, N.S., Gerges, S.N.Y., Jordan, R., and Arenas, J.P., 2005, "Numerical modeling of the vibro-acoustic behavior of a vehicle gearbox," *International Journal of Acoustics and Vibration*, 10 (2), 61-72.

7. Abbes, M.S., Bouaziz, S., Chaari, F., Maatar, M., and Haddar, M., 2008, "An acoustic-structural interaction modeling for the evaluation of a gearbox-radiated noise," *International Journal of Mechanical Sciences*, 50, 569-577.

8. Kartik, V., and Houser, D.R., 2003, "An investigation of shaft dynamic effects on gear vibration and noise excitations," *SAE paper 2003-01-1491*.

9. Fleming, D.P., 2007, "Vibration transmission through bearings with application to gearboxes," NASA/TM-2007-214954, *Proceedings of the 4th Biennial International Symposium on Stability Control of Rotating Machinery (ISCORMA-4)*, Calgary, Alberta, Canada.

10. He, S., Singh, R., and Pavic, G., 2008, "Effect of sliding friction on gear noise based on a refined vibro-acoustic formulation," *Noise Control Engineering Journal*, 56 (3), 164-175.

11. Singh, R., 2005, "Dynamic analysis of sliding friction in rotorcraft geared systems," *Final Report for ARO Award # DAAD19-02-1-0334*.

12. Hurty, W.C., 1965, "Dynamic analysis of structural systems using component modes," *AIAA Journal*, 3, 678-685.

13. Craig, R.R., and Bampton, M.C.C., 1968, “Coupling of structures for dynamic analysis,” *AIAA Journal*, 6, 1313-1319.

14. MacNeal, R.H., 1971, “A hybrid method of component mode synthesis,” *Computers and Structures*, 1, 581-601.

15. Farstad, J.E., and Singh, R., 1995, “Structural transmitted dynamic power in discretely joined damped component assemblies,” *Journal of the Acoustical Society of America*, 97, 2855-2865.

16. Farstad, J.E., and Singh, R., 1996, “Effects of modal truncation errors on transmitted dynamic power estimates in discretely joined component assemblies,” *Journal of the Acoustical Society of America*, 100 (5), 3144-3158.

17. Ewins, D.J., 1995, *Modal testing: theory and practice*, John Wiley and Sons, New York, NY.

18. Oswald, F. B., Seybert, A.F., Wu, T.W., and Atherton, W., 1992, “Comparison of analysis and experiment for gearbox noise,” *NASA Technical Memorandum 105330, Proceedings of the 6th International Power Transmission and Gearing Conference*, Phoenix, Arizona.

19. Oswald, F.B., Townsend, D.P., Valco, M. J., Spencer, R.H., Drago, R.J., and Lenski, J.W., 1994, “Influence of gear design parameters on gearbox radiated noise,” *NASA Technical Memorandum 106511*.

20. Korde, A., and Wilson, B., 2009, “The effect of flexible components on the durability, whine, rattle and efficiency of an automotive transaxle geartrain system,” *Gear Technology*, November/December 2009.

21. Smith, J.D., 2003, *Gear Noise and Vibration, 2nd Edition*, Marcel Dekker, New York, NY.

22. Ozguven, H.N., and Houser, D.R., 1988, “Mathematical models used in gear dynamics – a review,” *Journal of Sound and Vibration*, 121 (3), 383-411.

23. Mark, W.D., 1978, “Analysis of the Vibratory Excitation of Gear Systems: Basic Theory," *Journal of the Acoustical Society of America*, 63, 1409-1430.

24. Mark, W.D., 1979, “Analysis of the Vibratory Excitation of Gear Systems II: Tooth Error Representations, Approximations, and Application,”*Journal of the Acoustical Society of America*, 66, 1758-1787.

25. *RomaxDesigner User’s Manual*, 2008, Romax Technologies.

26. *Calyx User’s Manual*, 2004, Advanced Numerical Solutions (ANSOL).

27. *Load Distribution Program (LDP)*, 2006, Ohio State University Gear and Power Transmission Laboratory.

28. Zhou, H., Kato, M., Inoue, K., and Shibata, K., 1997, "Influence of bearing positions on sound radiation of single-stage spur gear system," *JSME International Journal, Series C*, 40 (1), 128-134.

29. Lim, T.C., and Singh, R., 1991, "Vibration transmission through rolling element bearings, Part III: geared rotor studies," *Journal of Sound and Vibration*, 151 (1), 31-54.

30. Gargiulo, E.P., 1980, "A simple way to estimate bearing stiffness," *Machine Design*, July, 107-110.

31. Lim, T.C., and Singh, R., 1990, "Vibration transmission through rolling element bearings, Part I: bearing stiffness formulation," *Journal of sound and vibration*, 139 (2), 179-199.

32. Liew, H-V., and Lim, T.C., 2005, "Analysis of time-varying rolling element bearing characteristics," *Journal of Sound and Vibration*, 283, 1163-1179.

33. Igarashi, T. and Nishizaki, T., 1988, "Studies on the sound and vibration of a gearbox (2nd report, effect of casing rigidity on sound)," *Transactions of the Japan Society of Mechanical Engineers, Part C*, 52 (508), 3037-3042.

34. Igarashi, T., and Asano, H., 1993, "Studies on the sound and vibration of a gearbox (3rd report, vibration transmission and sound radiation)," *Transactions of the Japan Society of Mechanical Engineers, Part C*, 59 (567), 3540-3547.

35. Mucchi, E., and Vecchio, A., 2008, "Acoustical signature analysis of a helicopter cabin in steady-state and run up operational conditions," *Proceedings of ISMA 2008*, Leuven, Belgium, 1345-1358.

36. Rose, T., 1991, "Using residual vectors in MSC/NASTRAN dynamic analysis to improve accuracy," *Proceedings of the 1991 MSC World User's Conference*.

37. Hambric, S.A., Boger, D.A., Fahnline, J.B., and Campbell, R.L., 2010, "Structure- and fluid-borne acoustic power sources induced by turbulent flow in 90 degree piping elbows," *Journal of Fluids and Structures*, 26, 121-147.

38. Campbell, R.L., and Pray, C.M., 2005, *Substructure synthesis methods and their application to structural-acoustic simulations*, ARL/Penn State Technical Report 05-012.

39. Hanford, A.D., and Campbell, R.L., 2010, *Wave Journal Bearing Dynamic Coefficients User's Manual, Rev. 1*, ARL/Penn State.

40. Campbell, R.L., 2003, "Distributed Journal Bearing Dynamic Coefficients for Structural Finite Element Models," Proceedings of ASME IMECE 2003, NCA-43770.

41. Kraus, J., Blech, J.J., and Braun, S.G., 1987, "In Situ determination of rolling bearing stiffness and damping by modal analysis," ASME Journal of Vibration, Acoustics, Stress, and Reliability in Design, 109, 235-240.

42. Advanced Numerical Solutions, 2009, *Coustyx User's Manual*.

43. Koopmann, G.H., and Fahnline, J.B., 1996, *Designing Quiet Structures*, Academic Press.

Appendix A: Demonstration of GMF Tone Amplitude Extraction from NASA GRC Test Data

The NASA test rig data was acquired using the following data acquisition parameters:

- Sample rate: 40 kHz
- Total number of samples: 131,072
- Total acquisition time: 3.2768 seconds

The NASA test rig accelerometer and microphone time histories were processed to extract the peak amplitudes at each of the gear meshing frequencies (GMFs). Figure A.1 shows a sample time history from an accelerometer mounted on the gearbox operating with rolling element bearings. A zoomed time history reveals the rich harmonic content in the signal. Each transducer time history was filtered at frequencies corresponding to the GMF harmonics. Figure A.2 shows time histories which include only 1xGMF, 2xGMF and 3xGMF signals, and clearly shows that each signal has a different amplitude.

Figure A.2 also shows that there is significant variability in the peak amplitudes over time. The signal envelopes, computed using the amplitude of the Hilbert Transforms of each time history, are also shown (in red) on the plots. Averages, maxima, minima, and standard deviations of each signal envelope were computed for all GMFs and sensors. Figure A.3 shows a sample of final computed GMF amplitudes and error bars. Also shown on the plot are peak values computed from FFTs of the time histories.

The FFTs were computed using the full time record, with a boxcar window. An example of an FFT is shown in Figure 1. These FFTs, while noisy at frequencies away from GMFs, may be used to confirm the tonal amplitudes computed using the time histories. The GMF amplitudes may be computed from the power spectral density levels at the GMF frequencies as:

$$X_{peak} = \sqrt{2G_{xx}(f_{peak})\Delta f} \,,$$

where $G_{xx}(f_{peak})$ is the one-sided autospectrum of $x(t)$ evaluated at a given peak frequency f_{peak}, and Δf is the frequency bandwidth of the autospectrum.

Figure A.3 shows that the peak values computed from the autospectra are within the ranges of the peak values computed from the time histories, but do not match exactly the mean peak amplitudes. Comparisons between the gearbox data with rolling element and journal bearings will be made using the time-history based peak levels, and will include error bars based on the computed standard deviations.

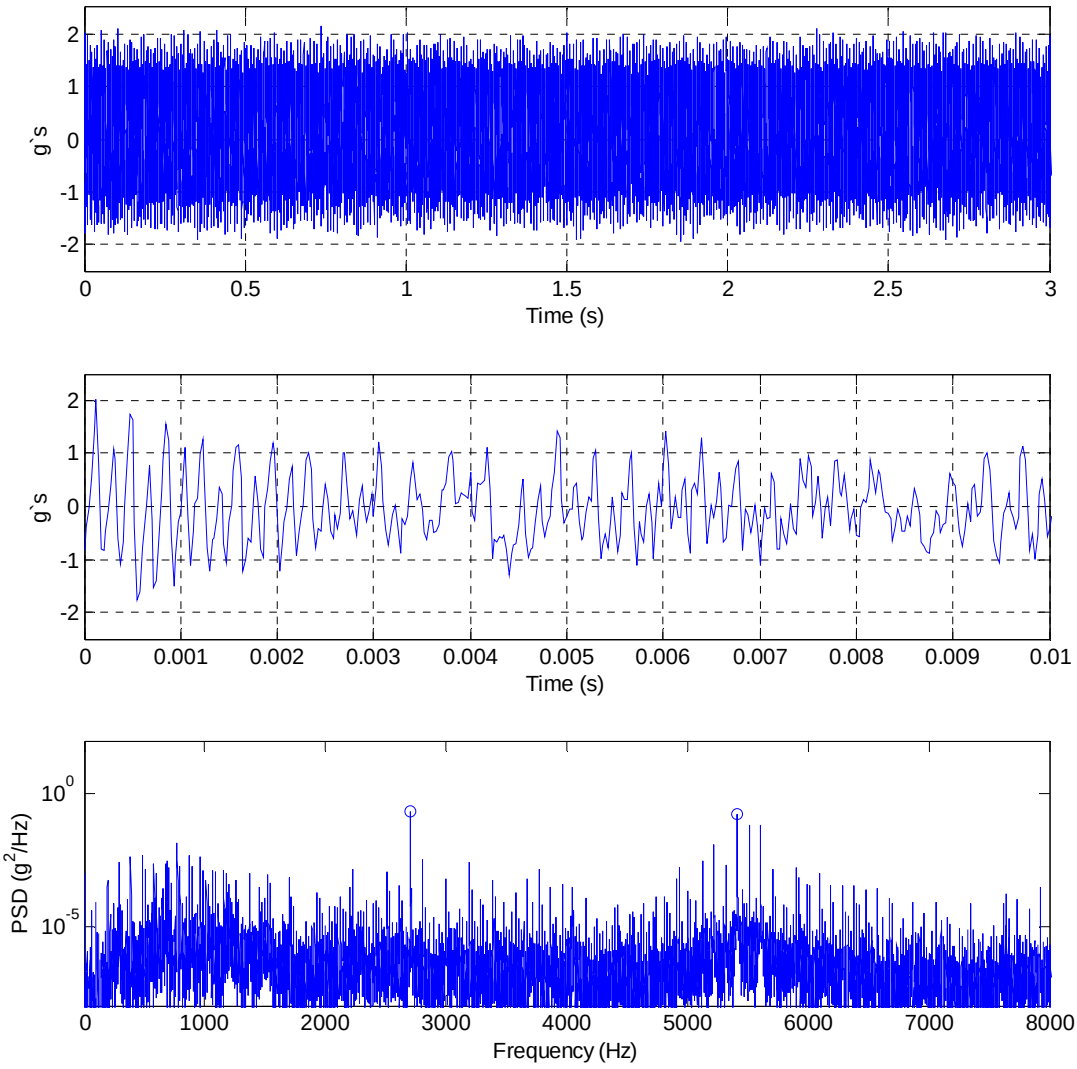

Figure A.1. Sample time history from NASA GRC test rig accelerometer, with rolling element bearings. Top – overall time history, captured over 3 seconds; middle – zoomed view of the beginning of the time history; bottom – FFT of the time history computed using the full time record, with no windowing. The 1st 2 GMFs are indicated with circles.

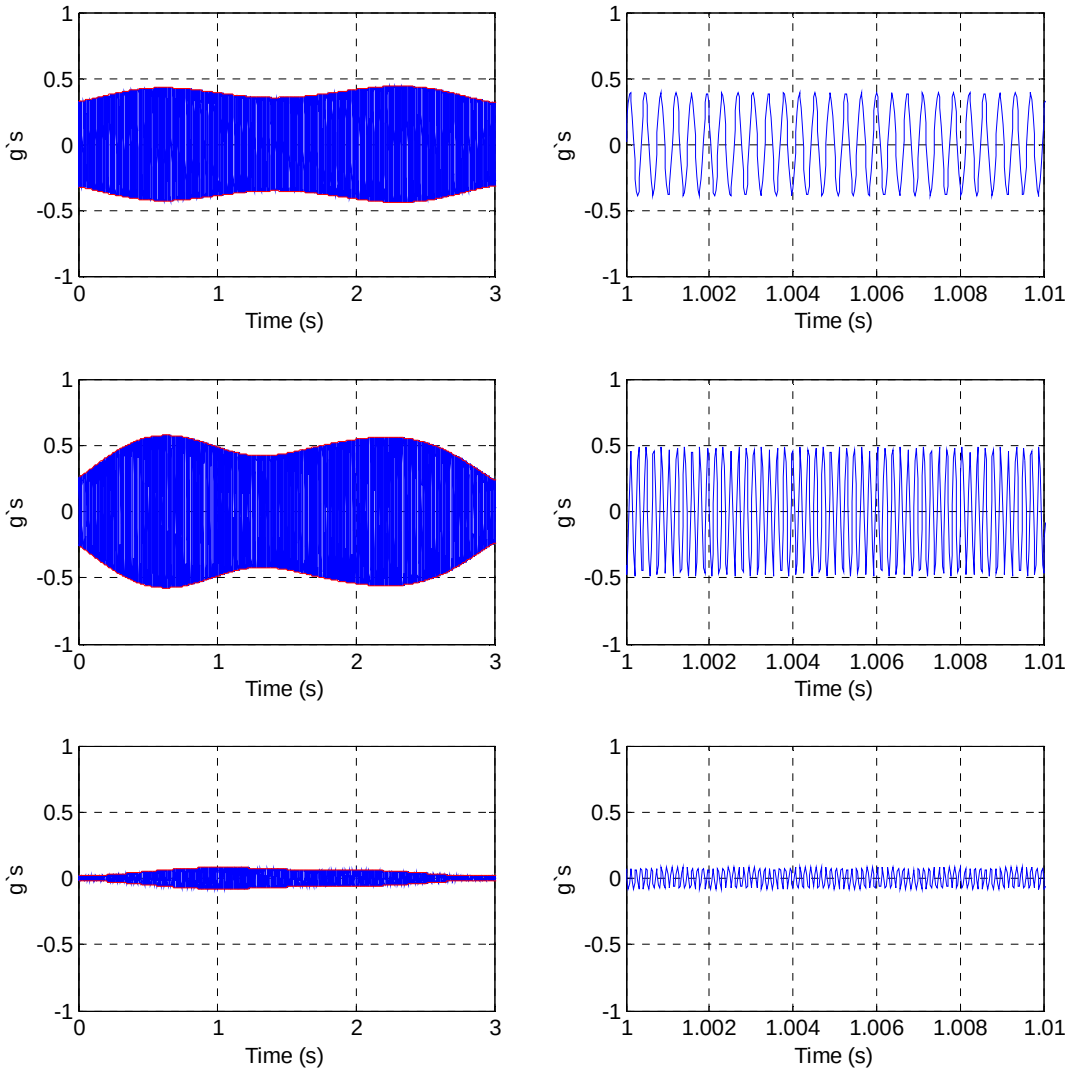

Figure A.2. Overall (left) and zoomed segments (right) of time history, filtered to include only signals at 1xGMF (top), 2xGMF (middle) and 3xGMF (bottom). The red curves on the left plots are the signal envelopes.

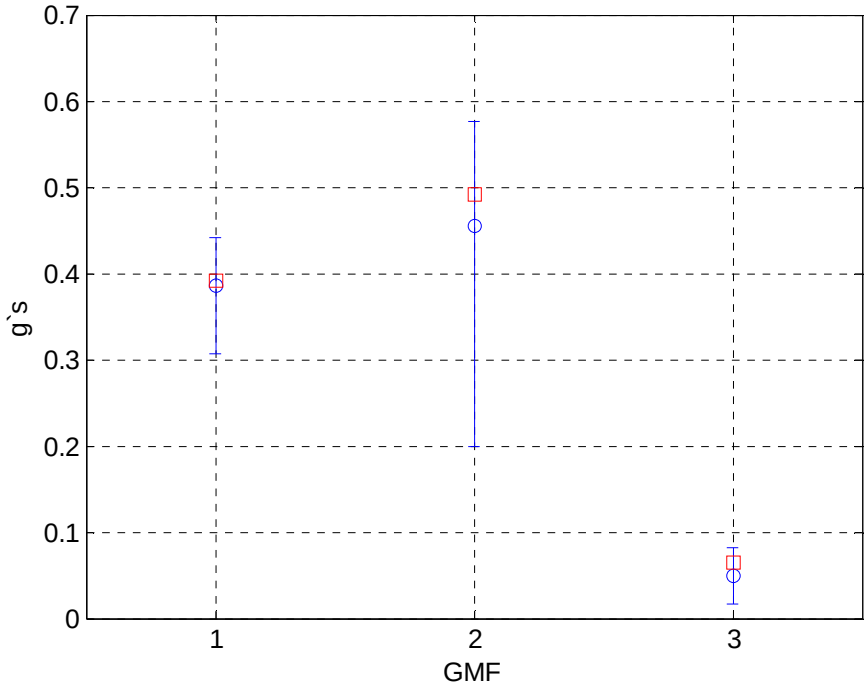

Figure A.3. GMF tone amplitudes. Blue averages and minimum/maximum spreads are based on the filtered time histories, while the red symbols are computed from the peaks of the FFTs of the time signals.

Appendix B: Brief Guide to Running Gearbox Numerical Simulations

The files, programs, and data provided separately may be used to compute the transmission of vibration and sound from gear tooth drives through a model of the NASA GRC gear test rig. A NASTRAN model of the rig, including the housing and shafts is provided in the NASTRAN directory. Nominal bearing stiffnesses have been included in the NASTRAN model so that component modes are computed which allow for rapid convergence of the forced response calculations. The remaining steps in the calculation procedure are:

1. Compute actual bearing stiffnesses and apply to CHAMP input files
2. Define frequency range of interest
3. Run the CHAMP Component Mode Synthesis program
4. Compute estimated radiated sound power based on the surface-averaged vibrations

1. Run bearing_stiffness.m matlab script.

The user must define the horizontal and vertical loads as the Fx0 and Fy0 variables in the code before running the code. These are the static loads applied to the bearing, and may be computed using commercial software like Romax, or from other methods. The ambient pressure and estimated equilibrium journal location can also be altered if needed. After starting the script, a graphical-user interface (GUI) pops up and the user inputs the bearing parameters. The code then computes the discrete and integrated stiffness and damping matrices for translational and rotational degrees of freedom by calling the functions multiWaveBrg.m, dynCoeffsWave.m and waveBrgStiffnessApprox.m. All matlab files must be either in the run directory or included in the matlab path.

To speed up the convergence of the component mode synthesis, nominal stiffness terms were already included in the FE model normal mode calculation. The newly computed bearing stiffness terms are added to/subtracted from the nominal values already in the model. These residual terms are used during component mode synthesis and are written to a txt file named 'added_stiffness.txt' for later use. The damping values are written to a file named 'added_viscdamp.txt.' The stiffness and damping values are also transformed from the bearing coordinate system to the FE model coordinate system. These files contain the stiffness/damping matrices and the nodes where they will be applied and have METRIC units.

This entire script will require a 5-10 minute runtime.

2. Set the frequency range of interest in the files 'xyz_drive_nodes.txt' and 'in.txt'

The 'xyz_drive_nodes.txt' contains the starting frequency on the first line in the 9-16th spaces (similar to NASTRAN convention). Lines 3-7 indicate the node, direction and magnitude of the drives. The X,Y, and Z slots are not used and can be left as 0.0. The gear-mesh stiffness is modeled using two closely-spaced springs to account for the finite width of the gear blank. Each of the four drive points represent a single end of one of the springs and has a magnitude of 0.25 so that the aggregate forcing amplitude is

unity. The NX, NY and NZ slots are the X, Y and Z components of a unit drive in the FE model coordinate system and represent the LOA direction (20°).

The 'in.txt' file contains input parameters for the 'NASA_GRC_gearbox_analysis.exe' code (located in the 'acs/' directory). The variable 'FI' is the number of frequency increments to include in the analysis with 1 Hz spacing. A separate 'in.txt' file also exists in the parent directory, but only the file located in the same directory as the executable must be changed. Since the wave bearing dynamic coefficients depend on rpm (which is related to the gear-mesh frequency), a single wave bearing stiffness set may not be sufficient for a wide frequency range. The maximum frequency range suggested for this model is 4 kHz.

3. Execute acs\NASA_GRC_gearbox_analysis.exe

This code reads in a pre-computed set of normal modes and performs component mode synthesis by including the bearing stiffness and damping information in the 'added_stiffness.txt' and 'added_viscdamp.txt' files. If these files do not exist, the code will still run, but will not have the correct stiffness and damping values. The normal modes information is stored in the files d_nodes.f06 and r_nodes.f06 for translational and rotational dofs respectively. The 'modes.txt' file contains the modal amplitudes at each element while the 'str_damp.txt' file contains the modal damping values (inferred from measurements). The 'geom.txt' file contains the boundary element mesh for the gearbox. The file 'xyz_response_nodes.txt' can be used to determine the acceleration at specific nodes but is not necessary for sound power analysis. The output files include 'high.txt' which contains the surface-averaged velocity multiplied by characteristic impedance of air and the gearbox surface area (in decibels reference unity). Units are described in the file 'README_units.txt'.

4. Add frequency components from 'high.txt' file with 'rad_eff_est.txt' file to get radiated sound power

The 'high.txt' file will contain a response value at each of the analysis frequencies which represents the amount of radiated sound power an equivalently-sized circular piston would radiate. The radiation efficiency of the gearbox was pre-computed, fit to a curve and stored in the file 'rad_eff_est.txt.' The corresponding value for that each frequency in the 'rad_eff_est.txt' file should be added to the 'high.txt' value to get the sound power radiated by the gearbox.

NOTES ON NASTRAN MODEL

The FE model is found in the NASTRAN folder in the file 'NASA_GRC_gearbox_wav.blk.' It is in standard NASTRAN format and has English units. For computing the normal modes (with residual vectors), the file 'gearbox_modal.dat' can be used.

REPORT DOCUMENTATION PAGE		Form Approved OMB No. 0704-0188

1. REPORT DATE *(DD-MM-YYYY)*	2. REPORT TYPE	3. DATES COVERED *(From - To)*
01-09-2010	Final Contractor Report	

4. TITLE AND SUBTITLE
Rotorcraft Transmission Noise Path Model, Including Distributed Fluid Film Bearing Impedance Modeling

5a. CONTRACT NUMBER
NNC08CB07C

5b. GRANT NUMBER

5c. PROGRAM ELEMENT NUMBER

6. AUTHOR(S)
Hambric, Stephen, A.; Hanford, Amanda, D.; Shepherd, Micah, R.; Campbell, Robert, L.; Smith, Edward, C.

5d. PROJECT NUMBER

5e. TASK NUMBER

5f. WORK UNIT NUMBER
WBS 877868.02.07.03.04.01

7. PERFORMING ORGANIZATION NAME(S) AND ADDRESS(ES)
Pennsylvania State University

8. PERFORMING ORGANIZATION REPORT NUMBER
E-17444

9. SPONSORING/MONITORING AGENCY NAME(S) AND ADDRESS(ES)
National Aeronautics and Space Administration
Washington, DC 20546-0001

10. SPONSORING/MONITOR'S ACRONYM(S)
NASA

11. SPONSORING/MONITORING REPORT NUMBER
NASA/CR-2010-216812

12. DISTRIBUTION/AVAILABILITY STATEMENT
Unclassified-Unlimited
Subject Category: 37
Available electronically at http://gltrs.grc.nasa.gov
This publication is available from the NASA Center for AeroSpace Information, 443-757-5802

13. SUPPLEMENTARY NOTES

14. ABSTRACT

A computational approach for simulating the effects of rolling element and journal bearings on the vibration and sound transmission through gearboxes has been demonstrated. The approach, using ARL/Penn State's CHAMP methodology, uses Component Mode Synthesis of housing and shafting modes computed using Finite Element (FE) models to allow for rapid adjustment of bearing impedances in gearbox models. The approach has been demonstrated on NASA GRC's test gearbox with three different bearing configurations: in the first condition, traditional rolling element (ball and roller) bearings were installed, and in the second and third conditions, the traditional bearings were replaced with journal and wave bearings (wave bearings are journal bearings with a multi-lobed wave pattern on the bearing surface). A methodology for computing the stiffnesses and damping in journal and wave bearings has been presented, and demonstrated for the journal and wave bearings used in the NASA GRC test gearbox. The FE model of the gearbox, along with the rolling element bearing coupling impedances, was analyzed to compute dynamic transfer functions between forces applied to the meshing gears and accelerations on the gearbox housing, including several locations near the bearings. A Boundary Element (BE) acoustic model was used to compute the sound radiated by the gearbox. Measurements of the Gear Mesh Frequency (GMF) tones were made by NASA GRC at several operational speeds for the rolling element and journal bearing gearbox configurations. Both the measurements and the CHAMP numerical model indicate that the journal bearings reduce vibration and noise for the second harmonic of the gear meshing tones, but show no clear benefit to using journal bearings to reduce the amplitudes of the fundamental gear meshing tones. Also, the numerical model shows that the gearbox vibrations and radiated sound are similar for journal and wave bearing configurations.

15. SUBJECT TERMS
Gear noise; Noise transmission; Vibration; Bearings; Rolling element bearings; Journal bearings; Wave journal bearings

16. SECURITY CLASSIFICATION OF:			17. LIMITATION OF ABSTRACT	18. NUMBER OF PAGES	19a. NAME OF RESPONSIBLE PERSON
a. REPORT	b. ABSTRACT	c. THIS PAGE			STI Help Desk (email:help@sti.nasa.gov)
U	U	U	UU	83	19b. TELEPHONE NUMBER *(include area code)* 443-757-5802